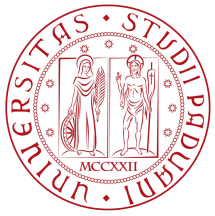

DIPARTIMENTO
DI INGEGNERIA
DELL'INFORMAZIONE

Università degli Studi di Padova

Department of Information Engineering

Ph.D. Course in Information Engineering

Curriculum: Information and Communication Technologies

XXXVI cycle

Control Co-Design of a CO2-based Chiller System

Coordinator: Prof. Fabio Vandin

Supervisor: Prof. Alessandro Beghi

Co-Supervisor: Prof. Mirco Rampazzo

Ph.D. Candidate: Enrico Sisti

A tutte le mie radici.

To all my roots.

"Por aquí pasan sueños acariciados por el viento"

– Anonymous on a wall in El Calafate (Argentina)

Abstract

Natural refrigerant R744 (i.e., CO_2, Carbon Dioxide) chillers are part of the current and next generation of chillers and find applications in various sectors, ranging from industrial processes to HVAC&R (Heating, Ventilation, Air Conditioning, and Refrigeration) systems, including commercial refrigeration.

This technology is considered a sustainable and environmentally friendly alternative to traditional refrigerants with practical well proven performance, enabling energy efficient and safe installations. However, designing and controlling a CO_2 chiller poses new challenges due to its unique thermodynamic and fluid dynamic properties compared to conventional chillers. These characteristics strongly influence decisions made during the design or retrofitting of existing systems, where a mere refrigerant replacement approach to achieve energy-efficient system configurations would fall short. Understanding the potential improvements in system design and control, as well as their impact on costs and energy demand, represents the initial step toward fostering effective technological developments, strengthening industry capabilities, and generating market interest.

Within this framework, this doctoral Thesis centers on the control co-design (CCD) of a chiller that uses CO_2 as a refrigerant. This involves the concurrent and integrated design of both the control system and the physical components of the cooling apparatus. By explicitly accounting for interactions between the control algorithms and the thermodynamic processes within the chiller, CCD aims to identify innovative solutions in both physical and control system design, paving the way for new levels of performance, efficiency, and enhanced functionality. The study was funded by the Italian

National Research Council (CNR) and was carried out in collaboration with the University of Illinois Urbana-Champaign (USA) and the University of Minnesota – College of Science and Engineering (USA).

Key aspects of CCD for the CO_2 chiller include: dynamic system modelling through a graph-based approach, the definition of the CCD problem in terms of an optimization problem and its solution via black-box optimization.

The outcomes reveal that the simultaneous optimization strategy offered by the CCD yields superior performance compared to the conventional sequential design process, wherein control designs are typically developed at the end, once the mechanical, thermodynamic, electrical, and other subsystems are completely defined.

Sommario

I sistemi chiller a refrigerante naturale R744 (ovvero CO_2, anidride carbonica) fanno parte dell'attuale e della prossima generazione di chiller e trovano applicazione in vari settori, dai processi industriali ai sistemi HVAC&R (Riscaldamento, Ventilazione, Condizionamento dell'aria e Refrigerazione), inclusa la refrigerazione commerciale.

Questa tecnologia è considerata un'alternativa sostenibile ed ecologica ai refrigeranti tradizionali, con un'affidabile e comprovata efficacia pratica, che consente installazioni energeticamente efficienti e sicure. Tuttavia, la progettazione e il controllo di un chiller a CO_2 presentano nuove sfide in virtù delle sue peculiari caratteristiche termodinamiche e fluidodinamiche, che differiscono significativamente dai chiller dotati di refrigeranti convenzionali. Queste caratteristiche influenzano fortemente le decisioni prese durante la progettazione o il retrofitting di sistemi esistenti, dove per ottenere configurazioni energeticamente efficienti un semplice approccio di sostituzione del refrigerante risulterebbe inefficace. Comprendere il potenziale miglioramento nella progettazione e nel controllo del sistema, nonché il loro impatto sui costi e sulla domanda energetica, rappresenta il primo passo per uno sviluppo tecnologico efficace, per rafforzare il settore e suscitare interesse sul mercato.

In questo contesto, il presente lavoro di tesi di dottorato è incentrato sul control co-design (CCD) di un sistema chiller che utilizza CO_2 come refrigerante. Ciò comporta la progettazione simultanea e integrata sia del sistema di controllo che dei componenti fisici del sistema a compressione di vapore. Tenendo conto esplicitamente delle interazioni tra gli algoritmi di controllo e i processi termodinamici all'interno del chiller, il CCD mira a identificare soluzioni innovative sia per la progettazione del sistema fisico che del sistema

di controllo, aprendo la strada a nuovi livelli di prestazioni, efficienza e funzionalità. Lo studio è stato finanziato dal Consiglio Nazionale delle Ricerche italiano (CNR) ed è stato svolto in collaborazione con l'Università dell'Illinois Urbana-Champaign (USA) e l'Università del Minnesota – College of Science and Engineering (USA).

Gli aspetti chiave del CCD del chiller a CO_2 includono: modellazione dinamica del sistema attraverso un approccio basato su grafi, definizione del problema CCD in termini di problema di ottimizzazione e sua soluzione tramite metodi di ottimizzazione black-box.

I risultati rivelano che la strategia di ottimizzazione simultanea offerta dal CCD produce prestazioni superiori rispetto ad un approccio convenzionale di progettazione sequenziale, in cui la progettazione del sistema di controllo viene generalmente svolta alla fine, una volta che i sottosistemi, meccanici, termodinamici, elettrici e altri, sono completamente definiti.

Acknowledgments

I would like to first express my gratitude to my co-supervisor, Professor Mirco Rampazzo, for his invaluable guidance. Without his unwavering support, I might not have embarked on this journey, let alone reached its conclusion. I am deeply grateful for his dedication and encouragement.

A special thank goes to my supervisor, Professor Alessandro Beghi, for his mentorship throughout my academic journey. He has provided me with numerous opportunities and helped me improve my research, greatly contributing to my professional growth

I would like to express my appreciation for the support provided by the Construction Technologies Institute (ITC) of the National Research Council (CNR), which funded this doctoral project. Collaborating with Silvia Minetto, Sergio Marinetti, and particularly Antonio Rossetti has been incredibly valuable. Antonio's insights have played a significant role in shaping and adding value to my work.

I extend my gratitude to Dr. Andrew Alleyne for his mentorship during my stay at the University of Minnesota. His guidance has had a significant impact on my project, and I am truly grateful for the opportunity he gave me to spend those months in such a supportive work environment. Also, special thanks to all past and present members of the Alleyne Research Group (ARG). I would like to express my gratitude to Christopher Thomas Aksland, Cary Laird Butler, Reid Smith, Kayla Russel, Frank Andújar Lugo, Zhara Marvi, Bo Wang, and Mahsa Hemmat for being so friendly and helpful throughout my visiting research period.

Lastly, but most importantly, I would like to thank my family and friends for all their love. My roots.

Contents

Nomenclature

Symbols

α	Convective heat transfer coefficient $[\mathrm{W\,m^{-2}\,K^{-1}}]$
Δ	Difference operator
$\dot{\mathrm{m}}$	Mass flow rate $[\mathrm{kg\,s^{-1}}]$
$\dot{Q}$	Heat transfer rate [W] or [kW]
$\dot{V}$	Volumetric flow rate $[\mathrm{m^3\,h^{-1}}]$
η	Efficiency $[-]$
κ	Covariance function (kernel)
$\mathbb{EI}$	Expected improvement function
$\mathbf{C}$	Block diagonal capacitance matrix
$\mathcal{A}$	Acquisition function
$\mathcal{D}$	Sample dataset
$\mathcal{E}$	Edge set
$\mathcal{G}$	Graph
$\mathcal{N}$	Normal distribution
$\mathcal{V}$	Vertex set

μ Mean function

μ^* Mean value

ω Rotational speed [rad s^{-1}]

$\overline{M}$ Edges to nodes mapping matrix

ϕ Flow coefficient [−]

ψ Pressure coefficient [−]

ρ Density [kg m^{-3}]

σ Net cross-sectional area to total cross-sectional area of the gas-cooler [−]

σ Standard deviation

σ^2 Variance function

φ Surrogate statistical model function

Ξ Multidimensional space

ξ Decision variables set

ζ Cross-sectional area of airflow passage in the four fans to total gas-cooler cross-sectional area [−]

ζ Valve pressure drop coefficient [−]

A Area [m^2]

C Capacitance matrix

C Capacitance

c_p Specific heat at constant pressure J kg^{-1} K^{-1}]

D Sources to internal nodes mapping matrix

d	Diameter [m] or [mm]
d	Disturbance
d	Element of the matrix D [$-$]
e	Edge
EE	Elementary effect
f	Friction factor [$-$]
f	Generic function
g	Gravitational acceleration [$\mathrm{m\,s^{-2}}$]
g	Inequality constraint function
h	Equality constraint function
h	Height [m]
h	Specific enthalpy [$\mathrm{kJ\,kg^{-1}}$]
J	Objective function
K	Element of the covariance matrix
k_L	Minor loss coefficient [$-$]
k_{valve}	Pressure loss gain [$-$]
L	Length [m]
l	Length [m]
M	Incidence matrix
m	Element of the incidence matrix [$-$]
m	Mass [kg]
m	Mean vector element

n	Rotational speed $[rpm]$
o	Valve opening $[-]$
P	Flow in a graph edge
P	Power [W] or [kW]
p	Efficiency polynomial coefficient $[-]$
p	Pitch [m] or $[mm]$
p	Pressure $[Pa]$ or $[bar]$
S_D	Sources to internal nodes mapping adaptive matrix
$S_{\overline{M}}$	Edges to nodes mapping adaptive matrix
T	Temperature [°C]
t	Thickness [m] or $[mm]$
u	Input
u	Internal energy [J]
V	Volume [m^3]
v	Vertex
w	Width [m]
x	State
z	Height [m]

Subscripts/Superscripts

0	Nominal conditions
$\mathcal{C}$	Control system
$\mathcal{P}$	Plant

A	Tank-flooded evaporator water loop
amb	Ambient conditions
B	Tank-building water loop
C	Compressor
c	Cooling
c	Cross-section
D	Space dimension
d	d^{th} dimension
e	External
f	Fin
fan	Fan
fr	Frontal
$head$	Head vertex
i	Internal
in	Inlet/Input/Incoming
is	Isentropic
liq	Refrigerant liquid condition
$load$	Thermal load
mec	Mechanical
nc	Natural circulation
out	Outlet/Output/Outcoming
$overall$	Overall

R	Row
seq	Sequential
sim	Simultaneous
t	Tube
t/R	Tube/Row
$tail$	Tail vertex
tot	Total
v	Volumetric
$valve$	Valve
w	Wall

Abbreviations

ARD	Automatic Relevance Determination
BO	Bayesian Optimization
BPV	Back-pressure valve
C	Compressor
CCD	Control Co-Design
DAE	Differential Algebraic Equation
DD	Data-Driven
EE	Elementary effects
EI	Expected Improvement
FD	Finite Difference
FE	Flooded evaporator

FP First Principle

FPDD First Principle Data-Driven

FV Finite Volume

GBM Graph-based Modeling

GC Gas-cooler

GP Gaussian Process

GSA Global Sensitivity Analysis

HT High temperature

HTL High thermal load

HVAC&R Heating, Ventilation, Air Conditioning, and Refrigeration

IHX Internal heat exchanger

LPR Low-pressure receiver

LT Low temperature

LTL Low thermal load

MB Moving Boundary

MCGM Multi-state Conservation-based Graph-based Modeling

MDO Multidisciplinary Design Optimization

MIMO Multiple-input and multiple-output

MT Mid temperature

MTL Mid thermal load

NFTL No Free Launch Theorems

PDE Partial Differential Equation

PI Proportional-integral

SH Superheating

SISO Single-input and single-output

SMB Switched Moving Boundary

VCC Vapor Compression Cycle

VCS Vapor Compression System

List of Figures

List of Tables

Chapter 1

Introduction

1.1 Motivation and Background

In recent years, regulations such as the F-gas regulation in Europe and international protocols like the Kigali Amendment to the Montreal Protocol have prompted both research and industry to adopt R744 as a refrigerant [1], particularly in heat pumps and chillers designed for various applications such as industrial processes, commercial refrigeration, and comfort heating and cooling [2, 3, 4]. The appeal of using CO_2 lies in its extremely low Global Warming Potential (GWP) of 1 or 0, coupled with its non-toxic, non-flammable nature, making it a safe and environmentally friendly choice. This shift towards CO_2 as a refrigerant is becoming increasingly crucial in addressing the rising demand for energy-efficient and environmentally sustainable refrigeration solutions in the long run. It is a fact that, e.g., Heating, Ventilation, Air Conditioning, and Refrigeration (HVAC&R) systems make substantial contributions to the energy consumption. No optimal design and operation of these systems not only leads to poor performance and higher costs but also contributes to elevated global emissions and an increased environmental footprint resulting from human activities [5]. It is noteworthy that, energy efficiency lies at the core of the European Green Deal's medium (i.e., 2030) and long-term (i.e., 2050) goals, aiming for intelligent, sustainable, and inclusive growth, as well as the transition to a resource-efficient

economy [6]. Besides, the design and control of these systems face new world challenges, e.g., the COVID-19 pandemic. For instance, recent studies have examined the impact of the pandemic on the usage of HVAC&R systems during periods of stringent measures in various countries [7, 8]. Additionally, researchers have explored the implications for the future operation of these systems, considering new policies and guidelines introduced by organizations worldwide to manage and mitigate indoor infection risks [9, 10]. In this context, developments in the design and optimization of heat pump operation are essential to reduce the carbon footprint of heating and cooling applications.

In this scenario, this doctoral Thesis consider a CO_2-based chiller [11, 12, 13, 14, 15, 16]. As a matter of fact, chillers are crucial components in applications where cooling is required [17, 18, 19]. An example of a CO_2-based chiller system is depicted in Figure 1.1. This kind of device removes heat from a liquid, typically water or a water-glycol mixture, in order to cool a space or process. The basic working principle of a chiller involves a refrigeration cycle, similar to how a household refrigerator works but on a larger scale. Chillers are versatile and can be used for various applications, including air conditioning in buildings, process cooling in industrial facilities, and cooling in data centers [20, 21, 22, 23]. They come in different types,

Figure 1.1: CO_2-based chiller system.

such as air-cooled chillers and water-cooled chillers, each with its advantages and applications.

The utilization of CO_2 as a working fluid in chillers is not a recent development. Carbon Dioxide has served as a refrigerant for over a century. Dating back to the 1890s, refrigerated vessels from Australia, New Zealand, and Argentina were already employing Carbon Dioxide for transporting meat and other food products to Europe [24, 25, 26]. One of the main disadvantage of a CO_2 chiller is the high operating pressures. However, thanks to recent technological advancements, current and upcoming generations of chillers include CO_2 ones. From an environmental perspective, CO_2 chillers hold considerable appeal. From an operational standpoint, they ensure an excellent heat transfer coefficient and guarantee substantially higher cooling capacities, exhibiting high efficiency, especially in large systems.

The nonlinear behaviors of HVAC&R systems, coupled effects, and the multidisciplinary approach required to address both the physical system (plant) and its control present significant challenges in developing efficient and effective systems under technological constraints. In this circumstance, modeling and simulation tools offer valuable opportunities to manage the increasing complexity of technologies, thereby providing invaluable support for designing and analyzing refrigerating systems. Additionally, simulation environments accelerate innovation cycles by facilitating rapid exploration of new solutions. Moreover, compared to real-world experiments, these software tools are generally more cost-effective, faster, and more flexible, as they allow for easy configuration of environmental parameters to replicate the operational conditions of the final product [27]. Consequently, once the boundaries are defined (e.g., thermal load and outdoor temperature profiles), validated models can reliably forecast system performance, particularly under conditions that are challenging to replicate in experimental tests. Furthermore, as these systems involve various dynamic interactions among subsystems, numerical models serve as valuable tools for optimizing operation and minimizing energy consumption within a more integrated Co-Design approach [28, 29]. Indeed, synthetic environments play a pivotal role in deploying co-simulation methods to design the entire system and achieve optimal solutions

while considering all multidisciplinary aspects.

1.2 Research Objectives

In the above mentioned context, technological innovation involves the design and development of advanced hardware (such as, heat exchangers) and software (such as control systems) [30, 31, 32, 33, 34, 35]. This gives opportunities to improve performance and energy efficiency simultaneously, also playing a pivotal role in minimizing the carbon footprint linked to various applications. Such contributions align with the objectives of sustainable development goals.

In the development of actively controlled engineering systems, such as a CO_2 chiller, the decisions made in the design of the physical system have a significant impact on how control systems for the plant should be designed to enhance performance. Conversely, decisions in control design also influence optimal plant design choices. This mutual influence is referred to as bi-directional design coupling. Traditional sequential design approaches, where plant design precedes control design, do not fully exploit this coupling. The holistic philosophy of multiphysics systems design acknowledges this interdependence, but existing methods lack the capability to articulate and fully leverage plant-control design coupling. Control Co-Design (CCD) methods formalize the handling of this coupling to pave the way for achieving new levels of performance, efficiency, and enhanced functionality [28, 36, 37, 38]. In particular, CCD includes several areas that range from control-inspired paradigms (i.e., innovative design solutions based on a practical engineering comprehension of dynamics and control) to co-optimization (that applies a formal mathematical approach involving nonlinear low/mid-fidelity models and multivariable constrained optimization), including co-simulation (which uses an iterative simulation process with multiphysics and high/mixed-fidelity dynamic models). In each of the three areas, the accuracy and complexity of the multiscale, multiphysics, nonlinear dynamic models are critical. The inherent uncertainty in these system models can add complexity to the design process [39]. Moreover, the multitude of cases

to be studied, influenced by various parameters, inputs, and model uncertainties, can be computationally prohibitive. Employing effective simulation techniques to determine suitable parameter values and inputs can aid in streamlining the design process. While CCD has been applied to specific applications like control-structure interaction for some time, recent research has provided more robust theoretical foundations and increasingly practical CCD methods [40, 41]. These methods offer systematic handling of physical system design elements, tools to balance the complexities of both plant and control design, and the ability to uncover superior design solutions that may not be immediately obvious. Ongoing CCD research aims to advance theories and methods that provide a more comprehensive perspective of both physical and control system design, effectively managing the interface between these design domains. Notably, progress has been made in employing open-loop optimal control methods to realistically address physical system design aspects [42], yet a gap remains in addressing the information-based constraints of implementable feedback control systems.

As will be further elaborated, recent research has increasingly focused on implementing CCD approaches to optimize HVAC systems [43, 44, 45, 46, 47] and, more broadly, thermal-fluid systems [48, 49, 50]. Nevertheless, there is a noticeable lack of detailed discussion concerning the crucial aspects of the dynamic modeling of these systems and its relationship with the utilization of CCD methods. Additionally, there is limited literature on consistent and explicit comparisons between the implementation of traditional approaches and more comprehensive CCD strategies, which could help evaluate critical aspects and the true potential of adopting CCD in the HVAC&R sector. This dissertation aims to fill the gap between theory and practice by developing a framework tailored for facilitating CCD of two-phase fluid systems. It will emphasize key aspects of dynamic modeling, delve deeply into the intricacies of implementing two distinct optimization approaches, and conduct a thorough comparison of their respective outcomes.

In this scenario, the Thesis focuses on the CCD of the considered CO_2 chiller. CCD, by explicitly considering interactions between control algorithms and thermodynamic processes within the chiller, aims to discover ef-

fective and sub-optimal solutions in both physical and control system design. This entails the simultaneous and integrated design of both control system aspects (e.g., feedforward actions) and crucial physical components of the cooling apparatus (e.g., gas-cooler). It is worth noticing that, graph-based modeling approaches offer a possible solution to modeling challenges for CCD purposes [51, 52]. In particular, graphs that exploit the laws of energy and mass conservation can be used to develop modular modeling tools that allow for the derivation of dynamic models that are computationally efficient, seamlessly integrated into the CCD framework, and yet can be modified to better meet the needs of individual disciplines. Another important consideration is that having such tools, which, on the one hand, simplifies the development of models of complex systems and, on the other, is well-suited to the development of control systems, can also represent a common platform for application domain experts and control systems experts. In this context, although certain graph-based tools already exist for single-phase fluid systems such as the toolbox developed by Renkert et al. [53], specific solutions for two-phase fluid systems, such as a CO_2 chiller, are not entirely at hand. One of the goal of this research is to fill this modeling gap.

The research presented here was supported by the Italian National Research Council (CNR) and was conducted in collaboration with the Construction Technologies Institute (ITC) of the CNR in Italy, as well as the Alleyne Research Group (ARG) at the University of Illinois Urbana-Champaign, and the University of Minnesota - College of Science and Engineering in the USA.

1.3 Problem Statement

Basically, this research aims at answering the questions:

Q_1 "How can CCD impact a CO_2 chiller, and is the investment justified?"

Q_2 "What exactly is design coupling? If modifications are made in one design domain, does that impact decision-making in other domains?"

Q_3 "What is the optimal way to design the physical aspects (e.g., the

gas-cooler) of an actively controlled CO_2 chiller to ensure that passive and active properties interact synergistically, leading to optimal system performance?"

Q_4 "What are the advantages, in terms of system performance and efficiency, as well as the limitations of the CCD solution compared to traditional sequential design approaches, where the design of the control system comes after the design of the chiller?".

The main steps to answer to these research questions include

i) System characterization: understand and model the behavior of the controlled CO_2 chiller, including its physical components and their interactions.

ii) System simulation: integrate the model in a Matlab-based Computer-aided Control System Design (CACSD) software tool. This software allows to generate synthetic data, carry out analysis, design and assess different CCD and traditional sequential design strategies.

iii) CCD design: definition of the CO_2 chiller CCD as an optimization problem that includes design and control objectives, global sensitivity analysis, decision variables selection, and the solution of the optimization problem.

iv) Analysis: comparison of the performance of CO_2 chiller CCD and a traditional sequential design approach.

1.4 Dissertation Scope and Main Contributions

The main goals of this dissertation are:

1. Development of a multi-state graph-based modeling toolbox, rooted in conservation-based graphs, specifically designed for integrating two-phase thermal management systems within a Control Co-Design frame-

work. Leveraging graph-based modeling, this toolbox, implemented in Matlab™, aims to streamline several aspects of model development by:

- providing a library of components for easy generation of customized graphs representing individual components;
- offering functions to rapidly connect graphs of individual components, creating subsystem or full system graphs;
- managing model parameters, initial conditions, causality relationships, and system-level inputs;
- supplying a model simulation function that dynamically scales with the order and size of the graph to perform dynamic simulations, which are essential for both analysis and optimization purposes.

2. Development of the dynamic model of a chiller system connected to a water tank, used to meet the cooling demands of a highly energy-demanding building. The model is developed using the multi-state graph-based modeling toolbox. Subsequently, it is integrated with a control system using a decentralized control approach. The model is intended to be integrated in a simulation environment to be part of a CCD framework.

3. Development of a CCD framework that exploits graph-based models, Global Sensitivity Analysis (GSA) using the Morris method, and black-box optimization. Two distinct objective functions are formulated for design and control optimization, defining two CCD problems: one employing a traditional sequential approach, while the other uses a simultaneous optimization strategy. Within the simulation environment, a Global Sensitivity Analysis (GSA) is performed on the objective functions using the Morris method. This analysis aims to identify and rank the most influential subset of design and control variables, shedding light on potential couplings between the design and control optimization subproblems. Finally, a proposed solution involves a black-box op-

timization framework that leverages the Bayesian optimization method to address CCD problems.

4. Comparison of the results from the two CCD approaches to assess advantages, disadvantages, and opportunities associated with employing CCD approaches in the HVAC&R domain.

The direct and collateral findings of this research have led to published and in preparation contributions:

J_1 Sisti, E., Rossetti, A., Minetto, S., Marinetti, S., Tosato, G., Beghi, A., and Rampazzo, M. (2023). Assessment of basic control strategies through dynamic simulations: A CO2-based chiller under extreme off-design conditions. Energy and Buildings, 289, 113066.

C_1 Riccardi, B., Sisti, E., Carnieletto, L., Rampazzo, M., and De Carli, M. (2023). Global Sensitivity Analysis applied to a dynamic energy simulation model: the case study of UniZEB prototype building. In 26th International congress of refrigeration. International Institute of Refrigeration.

C_2 Sisti, E., Antonio, R., Silvia, M., Sergio, M., Giacomo, T., Beghi, A., and Rampazzo, M. (2022). Modelling and Simulation of a CO2-based Combined Heating and Cooling System. In Proceedings of 15th IIR-Gustav Lorentzen Conference on Natural Refrigerants GL2022.

C_3 Sisti, E., Santiago, M. B., Silvia, M., Antonio, R., Sergio, M., Beghi, A., and Rampazzo, M. (2022). TinyML and IoT for cold chain monitoring: applications, challenges and opportunities. In Proceedings of 7th IIR Conference on Sustainability and the Cold Chain.

WiP_1 International journal article in preparation. Manuscript on multi-state graph-based modelling of two-phase refrigeration systems. Project in collaboration with University of Minnesota, USA.

WiP_2 International journal article in preparation. Manuscript on control co-design of two-phase refrigeration systems. Project in collaboration with CNR, Italy.

1.5 Thesis outline

The remainder of this thesis is organized as follows.

Chapter 2 introduces the chiller system, its operational schematic, and the associated processes. Following this, an overview of common modeling methods for Vapor Compression Systems (VCSs) is presented, emphasizing the significance of the graph-based modeling approach in the CCD context. The fundamentals of conservation-based graph models are then explored, elucidating the extension of the method to multi-state graphs. This approach leads to the development of a multi-state conservation-based graph modeling (MCGM) toolbox, outlined in Section 2.4. Subsequently, the chapter elaborates on deriving the chiller system model using the toolbox and concludes by introducing the considered control system for the chiller system.

Chapter 3 explores Control Co-Design methods, highlighting their potential advantages in designing HVAC&R applications. It begins by discussing issues concerning the definition of the optimization problem, with a particular emphasis on the importance of identifying couplings between subsystems/subproblems. The chapter introduces objective functions for design and control optimization subproblems in the given scenario. Furthermore, subsection 3.3.2 delves into the pivotal role of Global Sensitivity Analysis (GSA), particularly focusing on the Morris method. This method efficiently harnesses computationally intensive simulation models, serving as a preliminary analysis tool for CCD problems. In subection 3.4.2, the Morris method is applied to identify the subset of influential design and control variables concerning the aforementioned objective functions, with the goal of reducing the complexity of the optimization problems. The chapter then introduces prevalent optimization strategies for CCD problems, concluding with an exploration of the role of black-box optimization, specifically Bayesian optimization (BO), within the CCD framework.

In Chapter 4, two optimization problems are formulated using two CCD optimization strategies: a sequential approach and a simultaneous approach. An analysis of the search space for both optimization problems is performed to highlight the presence of couplings between design and control optimiza-

tion subproblems. The algorithmic approaches for both cases are also discussed, with a particular focus on the implementation of the BO method. The results of the optimization problems are singularly discussed and then compared to underscore potential synergies or conflicts between the solutions derived from the two optimization strategies. Their comparison offers a detailed performance analysis, highlighting the strengths and limitations of each strategy. Finally, a convergence analysis is presented to supplement the comparison between the strategies by examining the performance of the proposed algorithms, including a computational perspective.

Concluding Chapter 5 summarizes the contributions of the dissertation, proposing potential areas for future research.

Chapter 2

Chiller System Modeling

This chapter delves into an extensive explanation of the foundational principles and methodologies employed in developing the dynamic model of a CO_2-based chiller system operating in transcritical conditions and coupled with a stratified water storage tank.

The chapter is structured as follows: Section 2.1 introduces the reference system, its operational layout, and the involved processes. Following this, Section 2.2 provides an overview of common approaches to modeling vapor compression systems (VCSs), focusing on the challenges related to Control Co-Design. In Section 2.3, the graph-based modeling method is presented, highlighting the benefits of conservation-based graphs. This method is then used to develop a toolbox, as detailed in Section 2.4, tailored specifically for integration within Control Co-Design frameworks for two-phase thermal management systems. The subsequent use of this toolbox to derive the graph-based model of the chiller is discussed in Section 2.5. Finally, Section 2.6 explores the control architecture of the chiller system.

2.1 Chiller System Overview

The investigated CO_2-based chiller system harnesses the heat exchange occurring within a natural circulation flooded evaporator to lower the temperature of the water stream sourced from a stratified water storage tank.

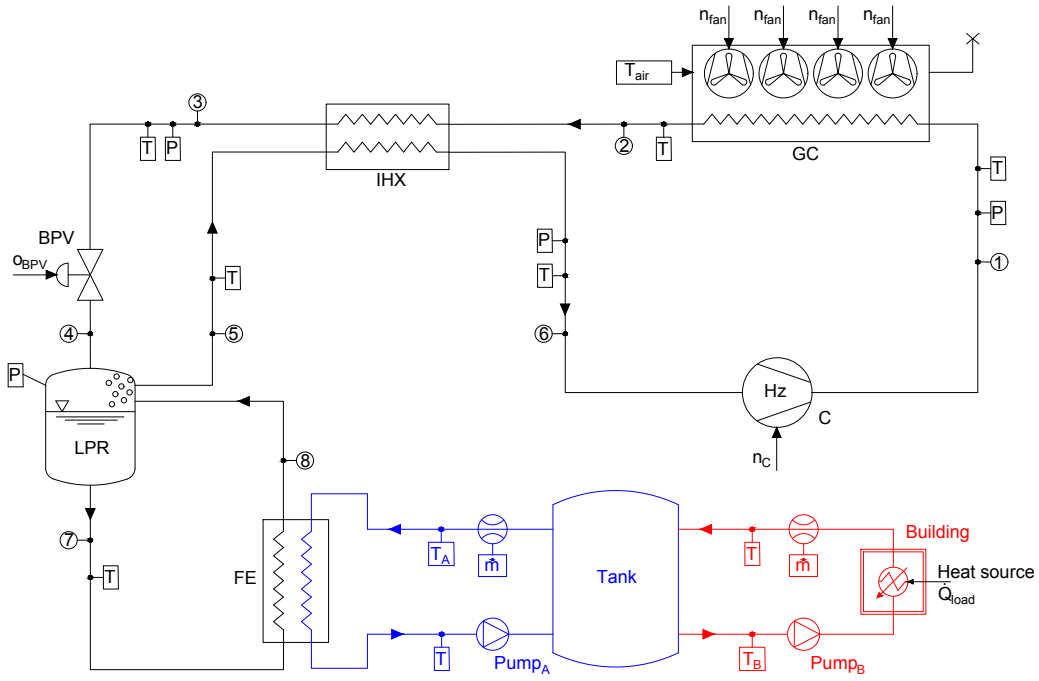

Figure 2.1: Operating scheme of the transcritical chiller system.

This cooled water is then employed to meet the cooling demand $\dot{Q}_{load}$ of a building. Operating under transcritical conditions, the system employs a vapor compression cycle (VCC) where the refrigerant in the high-pressure line can be in either a subcritical or supercritical state[1]. Figure 2.1 illustrates the operational scheme and the primary system components.

The system is driven by an inverter-controlled semi-hermetic compressor (C), and depending on the operating conditions, the refrigerant exits the compressor in either a subcritical or supercritical state. Subsequently, the refrigerant flows into a finned tube gas-cooler (GC) where it releases heat to an external air stream at ambient temperature T_{air}. The air, extracted from the surrounding environment, is forced through the heat exchanger by four axial fans. Afterwards, the refrigerant is further cooled by passing through the high-pressure side of the internal heat exchanger (IHX) and

[1]Subcritical signifies the fluid being below its critical point, while supercritical denotes the fluid being above the critical point.

then expanded to the evaporation pressure via a back-pressure valve (BPV), typically regulated to maintain its inlet high-pressure set-point [2, 11, 13].

After the expansion, the two-phase mixture enters the low-pressure receiver (LPR), designed as a separator of the liquid and vapor phases. This receiver connects its lower and upper parts to the refrigerant ports of a brazed plate heat exchanger (FE). The remaining ports of FE are configured for a counter-flow heat exchange with a secondary fluid (water). The refrigerant moves through the evaporator due to buoyancy-driven natural convection, where the driving force relies on the density difference between the liquid and gaseous phases at the evaporator's inlet and outlet.

In the water circuit, a recirculating pump (PumpA) supplies the flooded evaporator with water drawn from an insulated water tank (Tank) at temperature T_A. Then, a second recirculating pump (PumpB) delivers chilled water at temperature T_B to the building's air conditioning system.

Simultaneously, as a portion of the liquid in the receiver feeds the flooded evaporator, part of the refrigerant in a saturated vapor state exits the low-pressure receiver and enters the low-pressure side of the internal heat exchanger. As a result, the refrigerant undergoes heating by absorbing heat from the high-pressure line. This process ensures a consistent degree of superheating at the compressor suction.

2.2 Dynamic Modeling of Vapor Compression Systems

Vapor compression systems are widely used in the HVAC&R sector due to their remarkable efficiency and versatile applications, ranging from household systems to industrial usage. Their widespread adoption extends across various domains, including building HVAC systems, automotive air conditioning, cold chains, and more. Over the past few decades, their usage has seen a consistent and significant rise. Their usage has steadily grown over the past decades, prompting the need to design and develop systems that are increasingly efficient and adaptable to diverse contexts of use.

The design and development of control systems are intricately linked to the availability of adequate simulation models. Engineers rely on these models during the preliminary stages of virtual prototyping, occurring before the physical development and deployment of the system. This practice allows engineers to refine the design of individual components as well as the entire system, and optimize the control strategies. It involves conducting extensive simulations and assessments in a virtual environment prior to their real-world deployment. Unfortunately, the modeling of VCSs represents an exceptionally challenging task, due to the highly nonlinear behavior resulting from strong cross-coupling and multi-timescale thermal, hydraulic and mechanical dynamics. This is notably prominent in VCSs operating under transcritical conditions, especially when using carbon dioxide as the refrigerant, owing to the substantial variations in the refrigerant's thermophysical properties.

The operation of actuating components (such as compressors, valves, pumps, fans, etc.) primarily governs mechanical dynamics. Hydraulic dynamics arise from the interactions among these components, encompassing both mass flow devices and the other elements, and the circulating fluids within the system. Conversely, thermal dynamics are closely related to mass and heat transfer phenomena, owing to the complex coupled nature of the working fluids involved in the VCC. The dynamics to be captured depend heavily on the intended purpose of the model. In any case, the modeling technique should strike an optimal balance, being accurate enough to capture essential dynamic behaviors, while ensuring simplicity to prevent undesirable long simulation times and reduce the duration of the design phases.

Over recent decades, the field of industrial and research domains has witnessed the emergence of numerous tools and methodologies for thermal modeling. These models are commonly categorized into three groups [54, 55]: *white box*, *black box*, and *gray box* models.

White-box models, also referred to as first principles or mechanistic models, are characterized by their foundation on physics-based principles, employing fundamental physical laws like energy and mass conservation equations.

In contrast, black-box models rely on data-driven approaches like identification or time-series analysis to fit experimental data, offering purely numerical solutions through simplified reduced-order dynamic models.

The majority of modeling efforts for VCSs are often categorized as *gray-box* models. These models primarily rely on underlying physics but incorporate semi-empirical elements. They integrate empirical data, such as heat transfer correlations and efficiency maps derived from experimental tests, into their physics-based framework. *Gray-box* models can be classified into two main types: First Principle Data-Driven (FPDD) models and hybrid models [56]. FPDD models leverage *black-box* model identification techniques to adapt *white-box* model parameters to the modeled system. On the other hand, hybrid models combine the FP models, which explain only a part of the system's behavior as formulated, with a DD-type modeling that is required to shed light where first-principle equations fall short.

Summarizing, one can choose between First-Principle (FP), Data-Driven (DD), or a combination of both model types, depending on the level of understanding of the considered phenomena and the intended use of the model (see Figure 2.2). Modeling a complex system often involves leveraging the integration of these three approaches.

The effectiveness of a data-driven modeling method is evident in models quick identification, particularly in constructing a black-box model using available data, thereby expediting the modeling process. Despite their practicality, these models lack a direct physical interpretation of the studied system and often exhibit reduced robustness, limiting their applicability to a confined range of conditions based on the collected data and the specific system under examination.

In contrast, physics-based models, while more demanding in terms of time and effort during creation and validation, are characterized by minimized approximations and comprehensive structure, thus offering greater adaptability and robustness. Their capacity to promptly incorporate changes in system parameters or operating conditions into governing equations ensures their reliability. However, a drawback of this method is its reliance on substantial

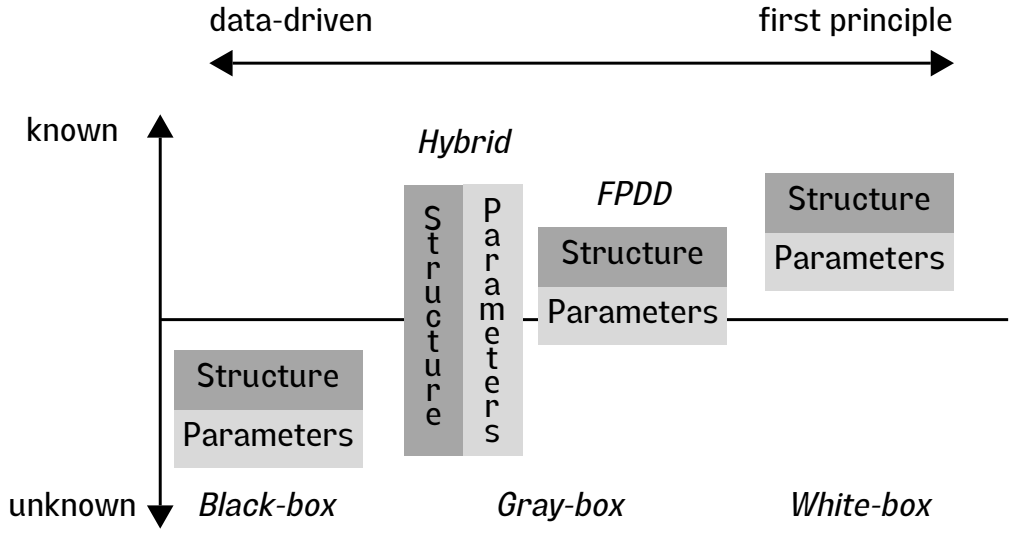

Figure 2.2: From left to right: Data-Driven Model (DD), Hybrid Model, First-Principle Data-Driven Model (FPDD), First-Principle Model (FP).

computational capabilities. Nonetheless, thanks to the continuous advancement in installed computing power within modern computer systems, this limitation is progressively alleviated, enabling the processing of increasingly complex models in shorter time frames [54]. This boost in computational capability has also promoted the development of more efficient optimization algorithms and methods, facilitating the handling of the intricate physics-based models required by these approaches, as will discussed further in this dissertation.

Design-oriented models often require high accuracy and can benefit from modeling approaches capable of reproducing dynamics across various orders, encompassing both low and high orders. On the other hand, control-oriented models prefer modeling approaches that replicate dynamics of the lowest possible order. This allows leveraging control system design tools without completely losing essential information regarding the underlying physics of the system.

Therefore, developing control-oriented models necessitates making certain assumptions. Among these, actuating components are often characterized

by high-order dynamics that can be overlooked, leading to simplifications in their modeling. Conversely, heat exchangers exhibit lower-order dynamics and significantly influence the overall system dynamics, as detailed in [33]. Hence, while the mass flow devices are represented with static algebraic formulations, the modeling of heat exchangers involves significantly more intricate procedures. Consequently, numerous researchers have directed their focus toward studying modeling approaches specifically designed for heat exchangers, paying particular attention to physics-based frameworks.

The modeling of heat exchangers can be broadly approached through three main methodologies, each offering distinct advantages and trade-offs in terms of accuracy, computational complexity, and the ability to capture specific dynamics [54, 55, 57].

- **Lumped Parameter Approach**
  The lumped parameter approach in heat exchanger modeling simplifies equations by assuming lumped parameters for the entire heat exchanger or specific fluid phases. While simpler than Moving Boundary (MB) and Finite Volume (FV) methods, it struggles to capture transient behavior, leading to lower accuracy. This limitation, particularly in detecting superheating/subcooling and capturing heat transfer dynamics, makes it unsuitable for advanced control development. Specifically, when applied to a two-phase fluid heat exchanger, the lumped parameter model tends to oversimplify by treating it as a single lumped subsystem, ignoring crucial dynamics associated with the boundary between two-phase and single-phase flow regions observed in more advanced MB and FV models.

- **Moving Boundary (MB) Approach**
  First introduced in [58], the MB method discretizes heat exchangers based on fluid phases, typically dividing them into three control volumes: superheated, two-phase, and subcooled. It can be regarded as an adaptation of the lumped parameter approach, where parameters are once again aggregated within regions defined by fluid phases, while permitting the transition point between these phases to be a dynamic

variable.. This strategy aims to grasp the dynamics of heat exchangers handling multiple fluid phases while maintaining the simplicity of lumped parameter models. Unlike lumped parameter models, MB models allow the lengths of fluid phases to vary over time. At the core of this method lies the capability to predict the effective phase change position within a heat exchanger. The introduction of the Switched Moving Boundary (SMB) approach further refined this technique, allowing fluid phases to appear and vanish without introducing numerical complications [59, 60, 61, 55]. The computational demand of a moving-boundary model is typically lower than that of a finite-volume approach due to its reliance on a smaller set of differential equations. However, this simplicity can compromise accuracy since these models use lumped characteristics for each control volume, such as a mean void fraction for the two-phase zone, and often overlook pressure drop and momentum effects.

- **Discretized Approach**: Finite difference (FD) and Finite Volume (FV) approaches provide models that are fairly accurate, and are largely implemented in commercial software packages. These methods typically derive governing equations either by discretizing the heat exchanger into numerous controls and applying conservation equations directly, assuming average or lumped parameters, or by discretizing the governing Partial Differential Equations (PDEs) using the FD method.

  The FV approach in heat exchanger modeling involves discretizing the fluid into control volumes (CV), allowing for the application of energy and continuity equations to each CV, determining average parameters. Higher discretization levels can improve model accuracy but come with increased computational demands. FV models, categorized by their inclusion or exclusion of conservation of momentum, can capture pressure drop effects but introduce complexities with transient momentum behavior, leading to a stiff dynamic system. An alternative approach to integrate pressure drops is to calculate static pressure differentials between regions, which results in the formulation of a system of Differ-

ential Algebraic Equations (DAEs).

Compared to lumped parameter approaches, FV methods provide more detailed fluid behavior modeling by considering thermophysical gradients and distributed parameters, resulting in higher accuracy predictions. However, the accuracy of predictions using FV methods heavily relies on the level of discretization, which varies based on the specific application. The accuracy is also influenced by assumptions made when calculating average properties for each region.

Differing from the MB approach, FV modeling operates by considering average values within control regions, relying on extensive discretization for accurate refrigerant mass predictions. In contrast to MB methods, which generally ignore momentum conservation, FV and FD methods provide numerous strategies to handle this aspect.

While FV and FD methods result in highly accurate models, they are more suitable for dynamic simulations than for developing control algorithms or predicting extensive transients due to their high dynamic order and complexity. Various toolboxes have been developed to leverage these qualities, primarily adopting component-based modeling frameworks (e.g., Thermosys [33]) and object-oriented approaches (e.g., Simscape, Modelica, etc.).

Object-oriented modeling has significantly influenced FV model implementation. These software packages represent physical connections through component model interconnections, and efficiently automate several aspects of model development, handling initial conditions, causality relationships, and system-level inputs.

In the domain of discretized methods, graph-based modeling (GBM) remains a relatively unexplored path for Vapor Compression Systems (VCS). Typically applied within single-phase thermal-fluid systems, there have been limited efforts to adapt this approach to two-phase thermal-fluid systems by adopting the bond-graph method, which graphically describes system dynamics across multiple domains using energy states and energy flows [62].

Various modeling examples exist, employing both true bond graphs [63, 64, 65] and pseudo bond graphs [66, 67, 68]. True bond graphs rely on effort and flow variables, whose combination represents power, enabling the potential description of all types of physical systems. Pseudo bond graphs differ from true bond graphs in their distinct characteristic: the product of variables associated with each bond does not always equate to instantaneous power, unlike true bond graphs [66]. Nonetheless, they share other characteristics of the method with true bond graphs. Furthermore, specific software solutions, like Simcenter Amesim [69], incorporate bond graphs for modeling two-phase systems and have demonstrated success in modeling and validating CO_2-based heat pump systems operating under transcritical conditions [70, 71, 72].

Recently, an alternative graph-based approach, known as conservation-based graph-based modeling, has emerged, proving highly suitable for modeling conservation-based systems [73]. This method efficiently models dynamic systems using interconnected nodes and edges. While extensively applied in single-phase thermal-fluid systems with notable success [74, 75, 76, 77, 78, 52], Russell et al. have demonstrated its adaptability to effectively capture the dynamics within two-phase systems [57]. Furthermore, the authors showcased that the computational burden of this modeling method can be equated to less accurate approaches. In Section 2.3, the approach pioneered by Russell et al. will be detailed, followed by its implementation to model the specific chiller system under investigation.

It must be noted that choosing the right modeling approach for heat exchangers has a ripple effect on how other system components are modeled. The advantage of GBM method lies in its seamless extension to various components within the chiller system. This versatility is especially beneficial in addressing CCD problems, leveraging models that serve both design and control objectives concurrently. The flexibility of GBM, shaped by its multi-domain logic and adjustable fidelity levels, paired with its computa-

tional efficiency, is an essential feature to meet the requirements of CCD for complex systems such as HVAC&R systems based on vapor compression cycles.

Finally, similar to the FV method, conservation-based graph-based modeling offers an opportunity to benefit from object-oriented modeling techniques. In Section 2.4, certain aspects of object-oriented modeling, such as class parameterization and inheritance, will be used to craft a toolbox for developing and fine-tuning graph-based models, following the framework introduced in [57]. This toolbox aims to streamline the generation of models from shared foundational elements.

2.3 Graph-Based Modeling Method

Graph-based modeling is a powerful methodology used for dynamic modeling and analysis, representing power flow across various domains: thermal, hydraulic, mechanical, and electrical. It establishes a unified framework capable of representing power flow dynamics both with linear and nonlinear relationships [74]. Graph-based models are structured based on energy conservation laws and offer modular construction by combining individual components into larger systems, streamlining the validation process as each component can be independently isolated and validated. Beyond this, they allow for adaptable fidelity, facilitating the adjustment of the number of dynamic states for either more detailed or simplified models, and also enable scaling the size of the model, ultimately enhancing computational efficiency [79, 57].

Stemming from energy conservation principles, these models offer flexibility by seamlessly adapting to different domains and find applications in diverse systems like thermal management systems [74, 76, 57], aircraft [75, 79, 77, 53, 52], and hybrid energy storage systems [51]. Their modular nature and ability to flexibly adjust across diverse energy domains and timescales make them well-suited for applications in model-based control [80, 77, 53, 51]. They effectively manage primary power flows while maintaining model simplicity. Additionally, their capability to individually linearize power flow

relationships aids in generating linear representations of nonlinear system dynamics, proving advantageous for control design.

A graph-based modeling framework inherently accounts for the storage and transport of conserved quantities, irrespective of the specific conserved quantity being addressed. This characteristic proves especially valuable when representing real-world systems governed by both energy and mass conservation. As demonstrated in [74], these systems are effectively described using two interconnected graphs: one following energy conservation laws and the other adhering to mass conservation principles. This is particularly suitable for systems using single-phase fluid as the working fluid, where the conserved energy is usually represented by considering the fluid temperature as state variable, which is insufficient to fully describe the hydraulic dynamics within the system. In such cases, an option exists to incorporate a secondary graph that considers pressure as a state variable for conserved mass. This secondary graph allows for a more nuanced representation of hydraulic dynamics, especially beneficial when these dynamics are relevant to the control system, and facilitates the calculation of mass flow rates subsequently employed within the primary graph. However, incorporating an additional graph increases the computational load of the model. Thus, in the interest of model simplicity, an effective alternative often involves computing mass flow rates through static algebraic formulations. Moreover, when dealing with two-phase fluids, graph-based modeling provides a chance to incorporate momentum equation within a single multi-state graph. This simplifies the process by eliminating the need for a second graph, as detailed later in this section.

Two recent investigations underscore the benefits of harnessing graph-based modeling within control co-design scenarios.

Laird et al. [51] introduce a framework for integrated plant and control optimization of electro-thermal systems, focusing on hybrid energy storage for electrified vehicles. It leverages graph-based modeling tools for multi-domain system representation and control design, addressing challenges such as high ramp rate loads. The framework is demonstrated through a case

study on a load-haul-dump mining machine, showcasing improvements in power density while reducing its size. It offers modularity, scalability, and adaptability for a wide range of electro-thermal systems beyond the specific case study.

In his doctoral thesis [52], Aksland employs graph-based modeling for control co-design in electrified aircraft, showcasing its effectiveness in optimizing integrated energy management across diverse scenarios. The approach integrates closed-loop dynamics into plant design, significantly enhancing closed-loop system performance. Additionally, it efficiently incorporates feedback control design into architecture and sizing optimization, effectively identifying mission-specific thermal management system designs.

In the following subsections 2.3.1 and 2.3.2, the mathematical formulations for the single-state vertex graph and the multi-state vertex graph are presented, following same formulation and formalism used in [57]. Finally, the conservation equations, used to describe the dynamics involved in single-phase fluids, two-phase fluids, and wall elements are discussed in subsection 2.3.3.

2.3.1 Single-state vertex graph

Graph-based modeling aims to define an oriented graph $\mathcal{G} = (\mathcal{V}, \mathcal{E})$ of N_v vertices $\mathcal{V} = \{v_i\}\,,\ i \in [1,\ 2,\ \ldots,\ N_v]$ interconnected by N_e oriented edges $\mathcal{E} = \{e_j\}\,,\ j \in [1,\ 2,\ \ldots,\ N_e]$. These vertices, v_i, represent the single states x_i corresponding to conserved quantities (such as energy or mass) and serve as storage units. Additionally, the rates of conserved quantity transfer P_j are associated with the respective edges e_j, oriented from tail vertices $v_{\text{tail}}^{e_j}$ to head vertices $v_{\text{head}}^{e_j}$, (refer to Figure 2.3). Each edge connects only two vertices and allows the flow to occur in either direction. The flows P_j are generally defined as a function of the adjacent vertex states, $x_{\text{tail}}^{e_j}$ and $x_{\text{head}}^{e_j}$, inputs u_j, as per Eq. 2.1.

$$P_j = f_j\left(x_{\text{tail}}^{e_j},\ x_{\text{head}}^{e_j},\ u_j\right). \tag{2.1}$$

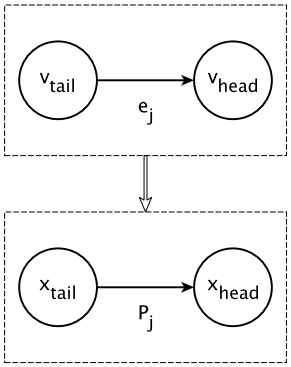

Figure 2.3: Graph with two nodes.

Since multiple edges can converge at each vertex, the dynamics are described by the difference between the summation of incoming flows P_{in} and the summation of outgoing flows P_{out}, as shown in the following equation.

$$C_i \, \dot{x}_i = \sum P_{in}^{v_i} - \sum P_{out}^{v_i}, \tag{2.2}$$

where C_i is the capacitance of the vertex v_i.

An important characteristic of graph-base models is that they are designed to account for both internal and external factors impacting the conserved quantity within the system. Distinguishing nodes as internal or external, and specifically categorizing edges originating from external nodes as source edges, helps in delineating their individual roles within the model. Also, from a practical point of view, this helps dealing with the definition of disturbances to the system. So, within the external nodes, two distinct types can be identified: source nodes $\mathcal{V}_s = \{v_k\}$, $k \in [1, 2, \ldots, N_s]$, where $\mathcal{V}_f \nsubseteq \mathcal{V}$, from which source edges $\mathcal{E}_s$ originate; and sink vertices $\mathcal{V}_t = \{v_l\}$, $l \in [1, 2, \ldots, N_t]$ with sink states $x_t = \{v_{t,l}\}$, where $\mathcal{V}_t \subset \mathcal{V}$ but the sink states x_t are not included in the state vector x. Figure 2.4 depicts an example of single-state graph of both order N_v and size N_e equal to 8, with six internal nodes, two sources and two sinks. The labels for vertices and edges are displayed in the top box, while the states and flows are

indicated in the bottom box.

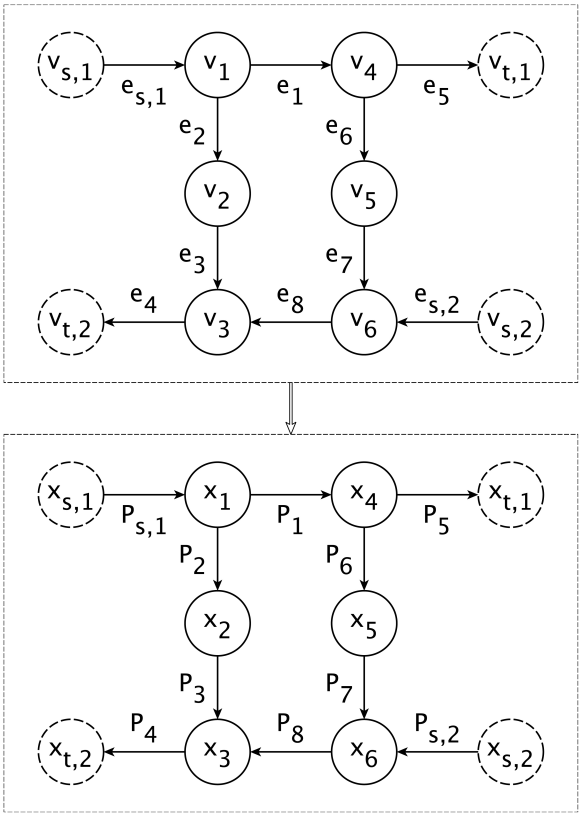

Figure 2.4: Single-state vertex graph model with two sources and two sinks.

The system dynamics are computed as follows:

$$C\,\dot{x} = -\overline{M}\,P(x, x_t, u) + D\,P_s, \tag{2.3}$$

where:

- $C = diag\,([C_i])$ represents a diagonal matrix of the capacitance values of each vertex.
- P denotes the vector of the flows P_j;
- P_s stands for the vector of the sources $P_{s,k}$;

- $\overline{M}$ is the matrix responsible for correlating the flows P_j to the states;
- D is the matrix that maps the sources $P_{s,k}$ to the internal states.

The mapping matrix $\overline{M} \in \mathbb{R}^{(N_v - N_t) \times N_e}$ stems from the incidence matrix $M = [m_{i,j}] \in \mathbb{R}^{N_v \times N_e}$, with the elements $m_{i,j}$ computed as:

$$m_{i,j} = \begin{cases} 1 & v_i \text{ if tail of } e_j \\ -1 & v_i \text{ is head of } e_j \\ 0 & \text{otherwise.} \end{cases} \tag{2.4}$$

In a similar way, the elements $d_{i,k}$ of the matrix $D = [d_{i,k}] \in \mathbb{R}^{(N_v - N_t) \times N_s}$ are given by:

$$d_{i,k} = \begin{cases} 1 & v_i \text{ is head of } e_{s,k} \\ 0 & \text{otherwise.} \end{cases} \tag{2.5}$$

The $\overline{M}$ and D matrices for the example in Figure 2.4 are:

$$\overline{M} = \begin{bmatrix} 1 & 1 & 0 & 0 & 0 & 0 & 0 & 0 \\ -1 & 0 & 1 & 0 & 0 & 0 & 0 & 0 \\ 0 & 0 & -1 & 1 & 0 & 0 & 0 & -1 \\ 0 & -1 & 0 & 0 & 1 & 1 & 0 & 0 \\ 0 & 0 & 0 & 0 & -1 & 0 & 1 & 0 \\ 0 & 0 & 0 & 0 & 0 & 0 & -1 & 1 \end{bmatrix}, \quad D = \begin{bmatrix} 1 & 0 \\ 0 & 0 \\ 0 & 0 \\ 0 & 0 \\ 0 & 0 \\ 0 & 1 \end{bmatrix}. \tag{2.6}$$

2.3.2 Multi-state vertex graph

Russell et al. [57], as previously mentioned, expanded the earlier formulation to encompass multi-state vertex graph-based models, enabling a more comprehensive representation of complex system dynamics and interdependencies. In their formulation, multi-state graph model dynamics are computed as:

$$\mathbf{C}\,\dot{x} = -\left(\overline{M} * S_{\overline{M}}\right)\, P(x, x_t, u) + (D * S_D)\, P_s, \tag{2.7}$$

with:

- $\mathbf{C} = diag\left([C^{v_i}]\right)$ represents a block diagonal matrix obtained combining the capacitance matrix of each vertex v_i;
- $S_{\overline{M}}$ is the adaptive matrix responsible for correlating the multi-flow edges to the states;
- S_D is the adaptive matrix that maps the multi-source edges to the internal states;
- The operator $*$ represents the Khatri-Rao product [81].

The block diagonal capacitance matrix is defined as in Eq. 2.8:

$$\mathbf{C} = \begin{bmatrix} [C^{v_1}] \in \mathbb{R}^{N_{x,\,v_1} \times N_{x,\,v_1}} & 0 & \cdots & 0 \\ 0 & [C^{v_2}] \in \mathbb{R}^{N_{x,\,v_2} \times N_{x,\,v_2}} & \cdots & 0 \\ \vdots & \vdots & \ddots & \vdots \\ 0 & 0 & \cdots & [C^{v_{N_v^*}}] \in \mathbb{R}^{N_{x,\,v_{N_v^*}} \times N_{x,\,v_{N_v^*}}} \end{bmatrix}, \tag{2.8}$$

where $N_v^* = N_v - N_t$ is the number of internal nodes and $N_{x,\,v_i}$ is the number of states in the vertex v_i.

The adaptive matrix $S_{\overline{M}} = [S_{i,j}] \in [\mathbb{R}]^{(N_v - N_t) \times N_e}$ is obtained combining block matrices $S_{i,j} = [S_{a,b}]_{i,j} \in \mathbb{R}^{N_{x,\,v_i} \times N_{P,\,e_j}}$, where $N_{P,\,e_j}$ is the number of flows in the edge e_j. The elements $S_{a,b}$ of each matrix $S_{i,j}$ are determined considering the dependence between the a^{th} state in the vertex v_i and the b^{th} flow in the edge e_j. If the a^{th} state in the vertex v_i is function of the b^{th} flow in the edge e_j, then $S_{a,b}$ is equal to 1, otherwise is equal to 0. This can be summarized as follows:

$$[S_{a,b}]_{i,j} = \begin{cases} 1 & (C\,\dot{x})_{i,a} = f\left(P_{j,b}\right) \\ 0 & \text{otherwise.} \end{cases} \tag{2.9}$$

A similar approach is used to determine the elements $S_{a,b}$ of each matrix $S_{i,k} = [S_{a,b}]_{i,k} \in \mathbb{R}^{N_{x,\,v_i} \times N_{P,\,e_{s,k}}}$ that composes the adaptive matrix $S_D =$

$[S_{i,k}] \in [\mathbb{R}]^{(N_v - N_t) \times N_s}$, where $N_{P,\,e_{s,k}}$ is the number of flows in the source edge $e_{s,k}$. Therefore, if the a^{th} state in the vertex v_i is function of the b^{th} flow in the edge $e_{s,k}$, then the element $S_{a,b}$ of $S_{i,k}$ are equal to 1, otherwise is equal to 0, as defined in Eq. 2.10:

$$[S_{a,b}]_{i,k} = \begin{cases} 1 & (C\,\dot{x})_{i,a} = f\,(P_{s,k,b}) \\ 0 & \text{otherwise.} \end{cases} \tag{2.10}$$

It is worth noting that this formalism is consistent with the formulation outlined in subsection 2.3.1 for a single-state vertex graph. Indeed, if each node is associated with only one state, then $\overline{M} * S_{\overline{M}} = \overline{M}$ and $D * S_D = D$.

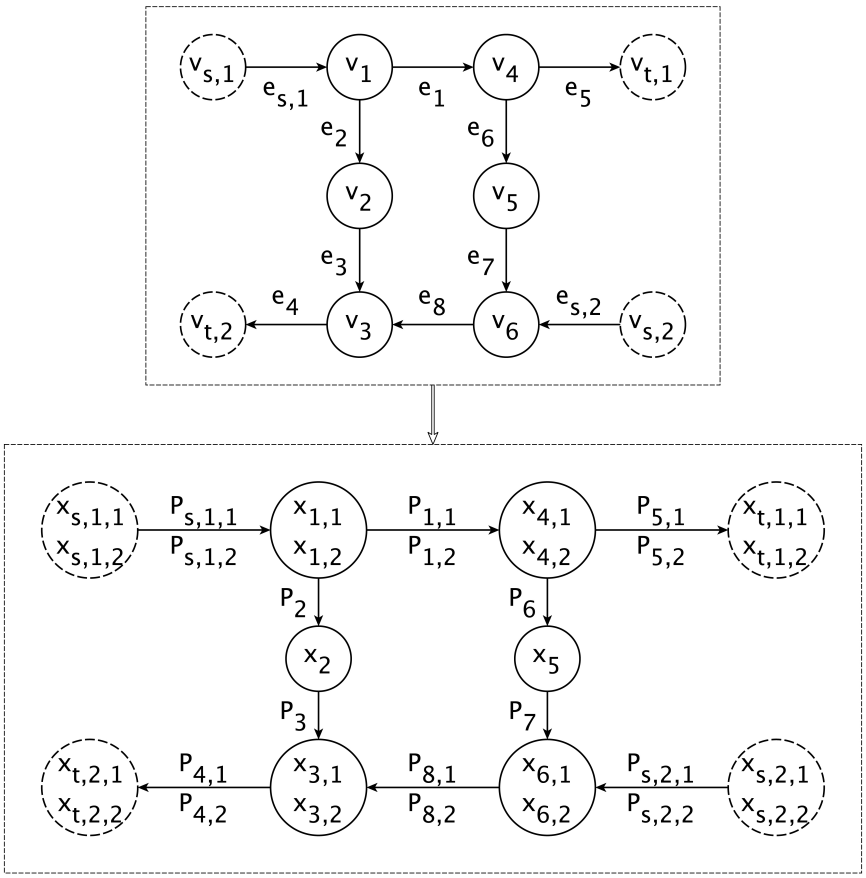

Figure 2.5: Multi-state vertex graph model with two sources and two sinks.

Figure 2.5 illustrates the multi-state graph, derived from Figure 2.4 considering one state for the internal nodes v_2 and v_5, and two states for remaining nodes.

The corresponding adapted matrices are:

$$\overline{M} * S_{\overline{M}} = \begin{bmatrix} 1 & 1 & 0 & 0 & 0 & 0 & 0 & 0 & 0 & 0 & 0 & 0 \\ 0 & 0 & 1 & 0 & 0 & 0 & 0 & 0 & 0 & 0 & 0 & 0 \\ -1 & 0 & 0 & 1 & 0 & 0 & 0 & 0 & 0 & 0 & 0 & 0 \\ 0 & 0 & 0 & -1 & 1 & 0 & 0 & 0 & 0 & 0 & -1 & 0 \\ 0 & 0 & 0 & 0 & 0 & 1 & 0 & 0 & 0 & 0 & 0 & -1 \\ 0 & -1 & 0 & 0 & 0 & 0 & 1 & 1 & 0 & 0 & 0 & 0 \\ 0 & 0 & -1 & 0 & 0 & 0 & 0 & 0 & 1 & 0 & 0 & 0 \\ 0 & 0 & 0 & 0 & 0 & 0 & -1 & 0 & 0 & 1 & 0 & 0 \\ 0 & 0 & 0 & 0 & 0 & 0 & 0 & 0 & 0 & -1 & 1 & 0 \\ 0 & 0 & 0 & 0 & 0 & 0 & 0 & 0 & 0 & 0 & 0 & 1 \end{bmatrix},$$

$$D * S_D = \begin{bmatrix} 1 & 0 & 0 & 0 \\ 0 & 1 & 0 & 0 \\ 0 & 0 & 0 & 0 \\ 0 & 0 & 0 & 0 \\ 0 & 0 & 0 & 0 \\ 0 & 0 & 0 & 0 \\ 0 & 0 & 0 & 0 \\ 0 & 0 & 0 & 0 \\ 0 & 0 & 0 & 0 \\ 0 & 0 & 1 & 0 \\ 0 & 0 & 0 & 1 \end{bmatrix}. \tag{2.11}$$

2.3.3 Graph-based model governing equations

As observed, nodes and edges respectively serve as storage and transport elements, defining the dynamics of the modeled system. Storage elements can be used to model various components like pipes, heat exchangers, tanks, separators, etc. Conversely, transport elements encompass energy flows such as enthalpy flow rate and convective heat transfer, along with fluid flows driven by dynamic forces from mass flow devices or pressure variations within a fluid.

To simplify model complexity and focus on essential dynamics, assump-

tions are necessary to formulate mathematical representations, including:

- heat exchangers are modeled as long cylindrical pipes, with their length significantly exceeding their diameter, while maintaining a consistent cross-sectional area;
- each node represents a control volume with constant cross-sectional area;
- single-phase fluids are incompressible, therefore no mass accumulation occurs and hydraulic dynamics are neglected;
- the fluid flows only in the longitudinal direction;
- single-phase and two-phase flows are homogeneous;
- heat conduction in flow direction is neglected.

In the following, the discussion continues delving into specific assumptions, categorized into storage and transport elements, and the mathematical formulation involving conservation equations.

Storage element modeling assumptions

In thermal management systems, two main types of nodes can be identified: fluid and solid nodes. Fluid nodes serve to represent both single-phase and two-phase fluid volumes, while solid nodes are typically designated to represent heat exchanger walls. Assumptions regarding fluid nodes include:

- two-phase fluid nodes store both energy and mass, whereas single-phase fluid nodes store only energy;
- two-phase fluid nodes consider pressure p and specific enthalpy h as state variables (Figure 2.6b), while single-phase fluid nodes consider temperature T as a state variable (Figure 2.6a).

Regarding solid nodes, the following applies:

- each node has isotropic properties;

- each node store only energy;
- solid nodes consider temperature as a state variable, as in Figure 2.6a.

(a) One-state node. **(b)** Two-state node.

Figure 2.6: State variables of the storage elements.

Transport element modeling assumptions

In these systems, transport phenomena are associated with the transfer of energy and mass. The mechanisms governing energy transfer primarily include enthalpic flow and convective heat transfer, both closely related to mass transport. While in some applications another mechanism to consider is heat exchange due to conduction, in this work, the focus remains solely on the former two. Therefore, the transport elements can be categorized into advective edges and convective edges. The former denote mass and enthalpic flows between two fluid nodes, whereas the latter represent convective heat transfer between a fluid and a solid node. The following assumptions hold for the advective edges:

- for single-phase fluids, only energy, represented as enthalpy flow rate, is considered as the transported quantity, as detailed in Figure 2.7a;
- in two-phase fluids, Figure 2.7b, the transported quantities include energy and mass, conveyed through enthalpy $\dot{m}\,h$ and mass $\dot{m}$ flow rates, respectively;

- the approach employs a modified version of the upwind scheme [82], where the enthalpy flowing through the edge corresponds to the enthalpy of the tail node.

Regarding convective edges, the transported quantity is energy, and the flow is represented by the heat exchanged between the two connected nodes: one fluid node and one wall node (Figure 2.7c), due to the temperature difference between them.

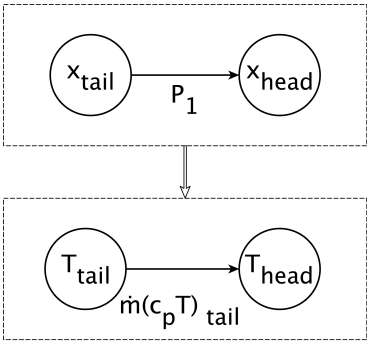

(a) Advective edge: single-phase flow.

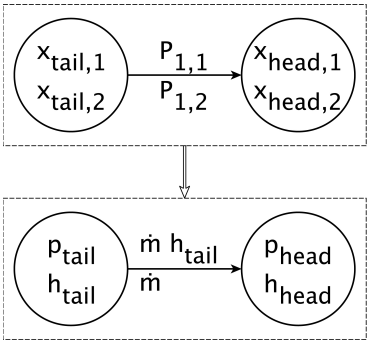

(b) Advective edge: two-phase flow.

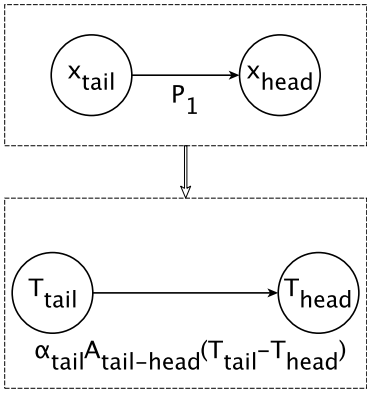

(c) Convective edge.

Figure 2.7: Flows of the transport elements.

Governing equations

All three types of nodes (single-phase v_1, solid v_2, and two-phase v_3) are depicted in the graph in Figure 2.8 representing a single-phase to two-phase

heat exchanger. To introduce the mathematical formulation that describe

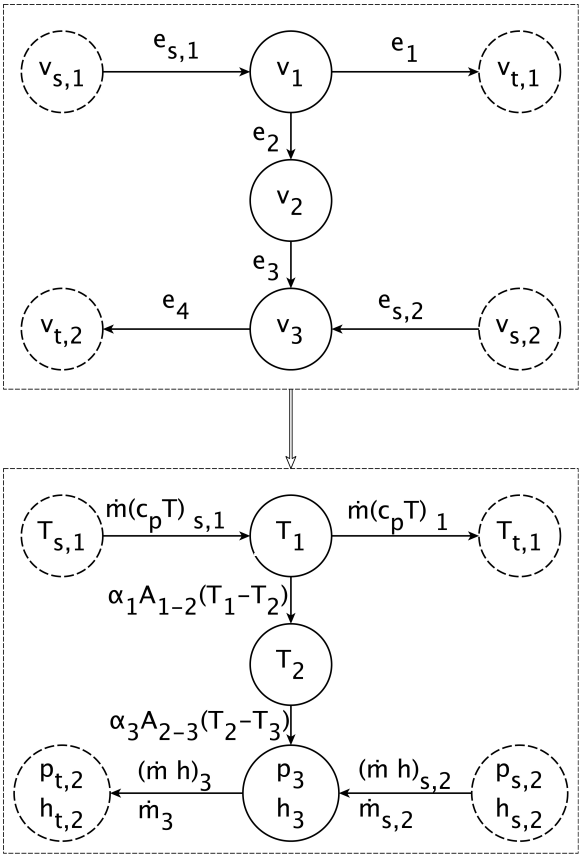

Figure 2.8: Single-phase to two-phase heat exchanger, with one single-phase v_1, one two-phase v_3, and one solid v_2 internal nodes.

the phenomena involved in a heat exchanger, it is useful to refer to three different subgraphs:

- single-phase fluid subgraph comprises by the source node $v_{s,1}$, the internal node v_1, the sink node $v_{t,1}$, and all the edges entering and exiting v_1 ($e_{s,1}$, e_1, and e_2);
- two-phase fluid subgraph includes by the source node $v_{s,2}$, the internal node v_3, the sink node $v_{t,2}$, and all the edges entering and exiting v_3 ($e_{s,2}$, e_3, and e_4);
- wall subgraph encompasses by the internal node v_2 along with edges e_2 and e_3.

The respective dynamics can be derived by applying Eq. 2.2 along with the previously mentioned assumptions. Therefore, for the single-phase fluid subgraph the following equation holds:

$$m_1 \, c_{p,1} \frac{dT_1}{dt} \; = \; \dot{m} \, c_{p,s,1} \, T_{s,1} - \dot{m} \, c_{p,1} \, T_1 - \alpha_1 \, A_{1-2} \, (T_1 - T_2), \tag{2.12}$$

where:

- $m_1 = \rho_1 \, V_1$ is the mass of the fluid within the discretized control volume, where ρ_1 is the density and V_1 is the volume;
- c_p denotes the fluid specific heat at constant pressure;
- $\dot{m}$ represents the fluid mass flow rate, which is typically defined as an input parameter or provided by a dedicated mass flow device (e.g., fan, pump, etc.);
- α_1 stands for the convective heat transfer coefficient of the fluid in v_1, computed from the mass flow rate $\dot{m}$;
- A_{1-2} refers to the heat transfer surface area between nodes v_1 and v_2.

Similarly, the dynamics of the wall subgraph are given by:

$$m_2 \, c_{p,2} \frac{dT_2}{dt} \; = \; \alpha_1 \, A_{1-2} \, (T_1 - T_2) - \alpha_3 \, A_{2-3} \, (T_2 - T_3), \tag{2.13}$$

where:

- m_2 is the mass of solid material that composes the discretized control volume of the wall;
- α_3 stands for the convective heat transfer coefficient of the two-phase fluid in v_3, computed from the mass flow rate $\dot{m}_{s,2}$;
- A_{2-3} refers to the heat transfer surface area between nodes v_2 and v_3;
- T_3 represents the temperature of the two-phase fluid in v_3, calculated from the state variables p_3 and h_3.

To describe the dynamics of the two-phase fluid subgraph, both energy conservation and mass conservation equations must be written:

$$A_{c,3}\frac{\partial(\rho\, u)_3}{\partial t} + \frac{\partial(\dot{m}\, h)_3}{\partial z} = \alpha_3\, A_{2-3,z}\,(T_2 - T_3) \tag{2.14}$$

$$A_{c,3}\frac{\partial \rho_3}{\partial t} + \frac{\partial \dot{m}_3}{\partial z} = 0, \tag{2.15}$$

where:

- $A_{c,3}$ represents the constant pipe cross-sectional area of the heat exchanger;
- $A_{2-3,z}$ represents the heat transfer surface area between nodes v_2 and v_3 per unit of length z;
- ρ_3 stands for the density of the fluid in v_3;
- u_3 is the internal energy of the fluid in v_3, given by:

$$\rho_3\, u_3 = \rho_3\, h_3 - p_3; \tag{2.16}$$

- z is the spatial coordinate in the direction of the flow.

Using the definition of internal energy, the energy conservation equation 2.14 transforms into:

$$A_{c,3}\frac{\partial(\rho\, h - p)_3}{\partial t} + \frac{\partial(\dot{m}\, h)_3}{\partial z} = \alpha_3\, A_{2-3,z}\,(T_2 - T_3). \tag{2.17}$$

As suggested in [33], the PDEs equations 2.14, 2.15, and 2.17, can be rearranged into ODEs by applying Leibniz's rule to integrate them along the spatial coordinate in order to remove the spatial dependence:

$$\int_{z_1(t)}^{z_2(t)} \frac{\partial f(z,t)}{\partial t}\; dz \;=\; \frac{d}{dt}\left[\int_{z_1(t)}^{z_2(t)} f(z,t)\; dz\right] - f(z_2(t),t)\,\frac{dz_2(t)}{dt} + f(z_1(t),t)\,\frac{dz_1(t)}{dt}. \tag{2.18}$$

Within the current modeling framework the boundaries z_1 and z_2 do not vary with time, hence Leibniz's equation reduces to:

$$\int_{z_1(t)}^{z_2(t)} \frac{\partial f(z,t)}{\partial t}\, dz \;=\; \frac{d}{dt}\left[\int_{z_1(t)}^{z_2(t)} f(z,t)\, dz\right]. \tag{2.19}$$

Therefore, setting $z_1 = 0$ and $z_2 = L_3$, where L_3 stands for the length of the control volume in v_3, and integrating with respect to z:

$$\int_0^{L_3} \left[A_{c,3}\frac{\partial(\rho\, h - p)_3}{\partial t} + \frac{\partial(\dot{m}\, h)_3}{\partial z}\right] dz \;=\; \alpha_3\, A_{2-3}\,(T_2 - T_3) \tag{2.20}$$

$$\int_0^{L_3} \left[A_{c,3}\frac{\partial \rho_3}{\partial t} + \frac{\partial \dot{m}_3}{\partial z}\right] dz \;=\; 0. \tag{2.21}$$

By applying Leibniz's rule:

$$A_{c,3}\,\frac{d}{dt}\int_0^{L_3} (\rho\, h)_3\, dz - A_{c,3}\,\frac{d}{dt}\int_0^{L_3} p_3\, dz + (\dot{m}\, h)_3 - (\dot{m}\, h)_{s,2} \;= \;= \alpha_3\, A_{2-3}\,(T_2 - T_3) \tag{2.22}$$

$$A_{c,3}\,\frac{d}{dt}\int_0^{L_3} \rho_3\, dz + \dot{m}_3 - \dot{m}_{s,2} \;=\; 0, \tag{2.23}$$

leading to:

$$A_{c,3}\, L_3\,\frac{d(\rho\, h)_3}{dt} - A_{c,3}\, L_3\,\frac{dp_3}{dt} \;=\; (\dot{m}\, h)_{s,2} - (\dot{m}\, h)_3 + \alpha_3\, A_{2-3}\,(T_2 - T_3) \tag{2.24}$$

$$A_{c,3}\, L_3\,\frac{d\rho_3}{dt} \;=\; \dot{m}_{s,2} - \dot{m}_3. \tag{2.25}$$

The first derivative term in Eq. 2.24 can be further rearranged as follows:

$$\begin{aligned}\frac{d(\rho\, h)_3}{dt} \;&=\; h_3\,\frac{d\rho_3}{dt} + \rho_3\,\frac{dh_3}{dt} \\ &=\; h_3\,\frac{\partial \rho_3}{\partial h_3}\bigg|_{p_3}\,\frac{dh_3}{dt} + h_3\,\frac{\partial \rho_3}{\partial p_3}\bigg|_{h_3}\,\frac{dp_3}{dt} + \rho_3\,\frac{dh_3}{dt},\end{aligned} \tag{2.26}$$

while the derivative in Eq. 2.25 can be written as:

$$\frac{d\rho_3}{dt} = \left.\frac{\partial \rho_3}{\partial p_3}\right|_{h_3} \frac{dp_3}{dt} + \left.\frac{\partial \rho_3}{\partial h_3}\right|_{p_3} \frac{dh_3}{dt}. \tag{2.27}$$

Finally, substituting these derivatives into Eqs. 2.24-2.25 and grouping the common factors, the energy conservation and mass conservation equations can be expressed as:

$$\begin{aligned} A_{c,3}\, L_3 \left[h_3 \left.\frac{\partial \rho_3}{\partial p_3}\right|_{h_3} - 1 \right] \frac{dp_3}{dt} + A_{c,3}\, L_3 \left[h_3 \left.\frac{\partial \rho_3}{\partial h_3}\right|_{p_3} + \rho_3 \right] \frac{dh_3}{dt} = \\ = (\dot{m}\, h)_{s,2} - (\dot{m}\, h)_3 + \alpha_3\, A_{2-3}\, (T_2 - T_3) \end{aligned} \tag{2.28}$$

$$A_{c,3}\, L_3 \left.\frac{\partial \rho_3}{\partial p_3}\right|_{h_3} \frac{dp_3}{dt} + A_{c,3}\, L_3 \left.\frac{\partial \rho_3}{\partial h_3}\right|_{p_3} \frac{dh_3}{dt} = \dot{m}_{s,2} - \dot{m}_3, \tag{2.29}$$

where $\dot{m}_3$ denotes the fluid mass flow rate, which is determined through the momentum equation, as will be elaborated upon shortly, or supplied by a dedicated mass flow device (e.g., compressor, valve, etc.).

Note that by considering Eqs. 2.12, 2.13, and 2.28-2.29, one can derive the capacitance matrix for each internal node in the following manner:

$$[C^{v_1}] = m_1\, c_{p,1} \tag{2.30}$$

$$[C^{v_2}] = m_2\, c_{p,2} \tag{2.31}$$

$$[C^{v_3}] = \begin{bmatrix} A_{c,3}\, L_3 \left[h_3 \left.\frac{\partial \rho_3}{\partial p_3}\right|_{h_3} - 1 \right] & A_{c,3}\, L_3 \left[h_3 \left.\frac{\partial \rho_3}{\partial h_3}\right|_{p_3} + \rho_3 \right] \\ A_{c,3}\, L_3 \left.\frac{\partial \rho_3}{\partial p_3}\right|_{h_3} & A_{c,3}\, L_3 \left.\frac{\partial \rho_3}{\partial h_3}\right|_{p_3} \end{bmatrix}. \tag{2.32}$$

Following the method outlined in [57], the momentum effects are integrated within the modeling framework to describe the two-phase flow. The acceleration drop and gravitational effects in the steady-state momentum

equation are neglected, while major and minor losses are considered:

$$p_{tail} - p_{head} - \frac{L_{tail}\, f_{tail}\, \dot{m}_{tail}^2}{2\, \rho_{tail}\, A_{c,tail}^2\, d_{h,tail}} - \frac{k_{L,tail}\, \dot{m}_{tail}^2}{2\, \rho_{tail}} \;=\; 0, \tag{2.33}$$

where d_h, f, and k_L are the hydraulic diameter, the friction factor, and the minor losses coefficient of the tail node, respectively. Although both f and k_L are dependent on the flow regime, in the following, they will be considered as parameters specific to the component being modeled.

Hence, the mass flow rate transferring between two two-phase fluid nodes can be calculated using Eq. 2.33 in the following manner:

$$\dot{m}_{tail} \;=\; A_{c,tail} \sqrt{\frac{2\,(p_{tail} - p_{head})}{\frac{L_{tail}\, f_{tail}}{\rho_{tail}\, d_{h,tail}} + \frac{k_{L,tail}}{\rho_{tail}}}}. \tag{2.34}$$

2.4 Multi-state Conservation-based Graph-based Modeling (MCGM) Toolbox

Taking advantage of the properties and mathematical framework inherent in the multi-state conservation-based graph-based modeling method, a dedicated toolbox called the MCGM Toolbox has been developed. Its development specifically aims to incorporate the capability of modeling two-phase thermal management systems, aligning with the methodology proposed in [57]. This toolbox is tailored to facilitate the modeling stages, automating composition and analysis of the graph, through a set of routines implemented in Matlab™ that leverages built-in functions of the *Graph and Network Algorithms* library [83]. Although in its current version it appears as a stand-alone tool, the author's intent is for the toolbox to be conceived as an extension, explicitly drawing inspiration from it, of the multi-domain toolbox developed in [53], and based on the graph model interconnection algorithms presented in [79].

The main features of the toolbox are depicted in Figure 2.9. The foun-

dation of the toolbox consists of a component library enabling users to effortlessly obtain the graph model of several components, such as pipes, heat exchangers, tanks, and separators. Users simply specify:

- component type;
- component graph name;
- fluid type and number of states in the fluid nodes;
- material of solid nodes;
- number of nodes for each type of nodes to align the resulting model with their specific objectives and computational resources.

A dedicated routine manages the composition of the graph and provides both the graph's structure and the corresponding data structure containing node, edge, and model parameter information. Among these, each node and edge is associated a name, which serves as a label that can be easily handled in further operations, while model parameters can be defined by the user in a subsequent phase. Additionally, another routine computes the incidence matrix, yielding $\overline{M}$ as detailed in Eq. 2.4. It also calculates the mapping matrix D for the source flows, and determines the adaptive matrices $S_{\overline{M}}$ and S_D as specified in equations 2.5, 2.9, and 2.10.

Subsequently, the toolbox provides functionalities for linking individual component graphs to construct more intricate subsystems or complete systems. The user is asked to define an array comprising pairs of node names that are part of distinct graphs. The connection between two graphs occurs only if the nodes form a pair of types: fluid/fluid, wall/fluid, or fluid/wall. In the case of fluid/fluid pairs, the routine also verifies that the two nodes contain the same number of states and the same type of fluid. Moreover, wall nodes can only be internal nodes. If these criteria are not met, the routine returns a message indicating the impossibility of connecting the two graphs. However, in a positive outcome, the connection operates as follows:

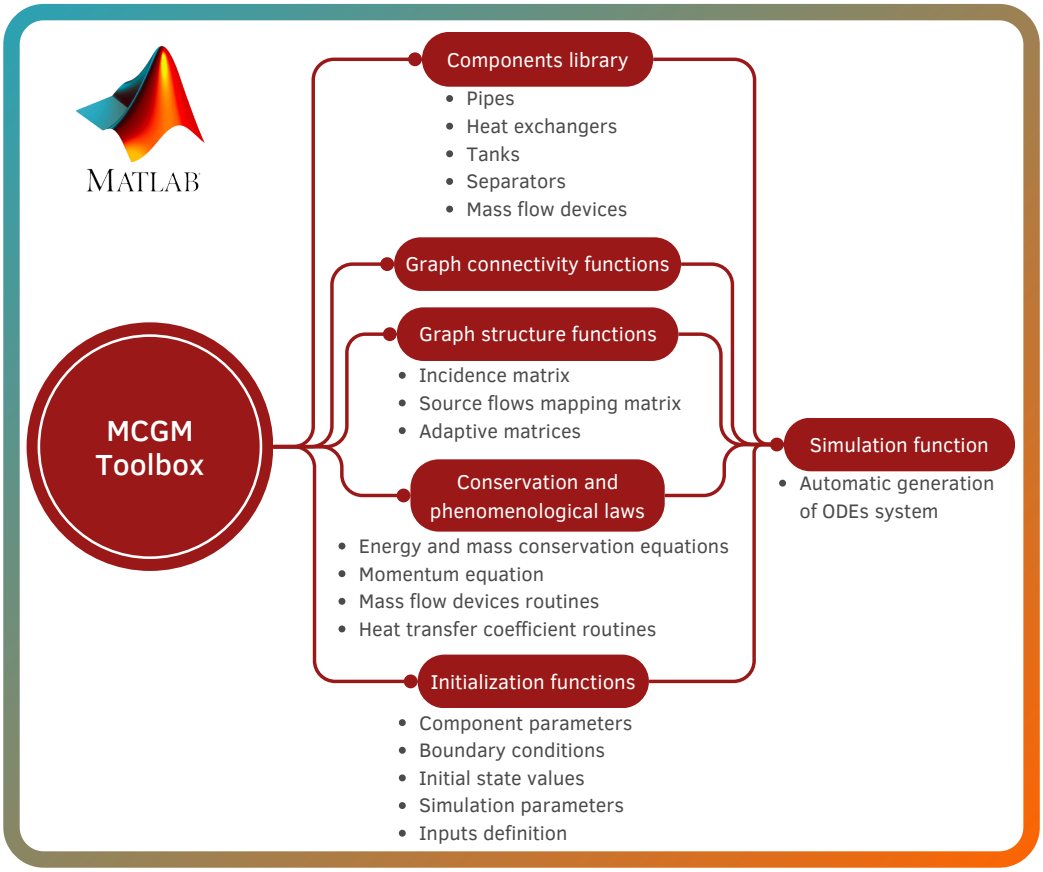

Figure 2.9: MCGM Toolbox.

- if the two nodes are both internal nodes, the routine establishes an edge from the first to the second node of the pair. This edge is advective if the nodes are of type fluid/fluid, and convective if the nodes are of type wall/fluid or fluid/wall;
- when one node is a source and the other is an internal node, a source edge is traced from the source node to the internal node. The edge is advective for fluid/fluid node pairs, and convective for wall/fluid or fluid/wall pairs;
- in the case of one node being a sink and the other an internal node, the sink node is eliminated, and the internal node inherits the connections that were previously linked to the sink node;

- if one node is a source and the other a sink, both nodes are eliminated, and their respective connections are inherited by the internal nodes that were originally linked to them.

After establishing the connection, a new graph is obtained, and the toolbox automatically computes the graph structure, also identifying fluid circuits, and topology data structures by integrating the information from each combined graph. Additionally, the mapping and adaptive matrices are recalculated. At this point, users have the option to incorporate mass flow devices into the model, following the instructions outlined in subsection 2.4.2.

As suggested by Russell et al. [57], fluid properties are stored in lookup tables generated using *REFPROP* [84]. These lookup tables are used within the simulation function to interpolate the fluid properties in each fluid node, using state variable values. Boundary conditions and inputs can encompass the states of source nodes, the flows of edges connecting internal nodes to sink nodes, if not defined during the simulation by mass flow device functions, and manipulable variables of mass flow devices. Conversely, initial conditions cover all dynamic states of internal nodes. A toolbox function is responsible for extracting information from the graph's data structure to define two arrays, one for boundary condition values and the other for the initial conditions. Then, the user can decide to conveniently set the values of model parameters, boundary conditions and initial state values either through the workspace or via user-defined functions. Once the parameters of the components and the initial conditions are set, a routine computes the block diagonal capacitance matrix, as described in Eqs. 2.8, 2.30, 2.31, and 2.32.

Finally, the toolbox includes a simulation function capable of adapting to any graph order and size, and easily accessible to solvers. This function requires essential data structures of the dynamic model (graph topology data, model parameters, boundary conditions, inputs, and initial conditions) along with specific simulation and solver parameters. Using the node state values as a starting point, it computes system dynamics at each integration

step using Eq. 2.7. Notably, this simulation function seamlessly integrates with controller functions and can be readily implemented within analysis and optimization functions.

2.4.1 Simulation function

The main steps of the algorithm implemented within the simulation function are outlined as follows:

- during each simulation step, the integrated state values provided by the solver are stored and used to compute the fluid properties of individual fluid nodes and the block diagonal capacitance matrix using Eq. 2.8;
- boundary conditions and inputs are associated with their respective nodes, edges, and manipulable variables, and their values are assigned accordingly;
- mass flow rates, sourced from mass flow devices, natural circulation effects (see subsection 2.4.2), and internal tank mass conservation, are computed using specific routines and linked with their corresponding edge;
- calculation of momentum-induced mass flow rates in two-phase flow is performed using Eq. 2.34;
- energy flows in advective edges are computed as depicted in Figure 2.7;
- starting from mass flow rate values, heat transfer coefficients are computed using correlations detailed in subsection 2.4.2. Subsequently, energy flows are computed for each convective edge;
- lastly, the vectors of edge flows P and sources P_s are assembled, leveraging topology data, and the derivatives of state variables are computed using Eq. 2.7.

2.4.2 Components library

The main thermal management components in the toolbox are:

Pipes

Pipes are modeled as long circular tubes. The basic element of a pipe comprises only one source, one internal, and one sink nodes. Figure 2.10 shows the graphs of the basic element of a single-phase and a two-phase pipe. However, by setting the number of nodes, the toolbox offers the opportunity to generate multiple-node pipes, attaching each node in series. Moreover,

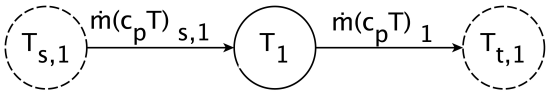

(a) Single-phase pipe.

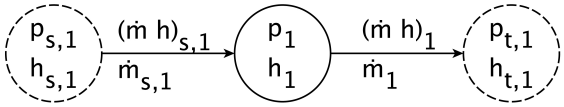

(b) Two-phase pipe.

Figure 2.10: Pipe graphs with one internal node.

the users provide the name to associate with the component graph, and the number of state variables and fluid type in the nodes. If the number of states and the chosen fluid type are inconsistent, the toolbox displays an error message highlighting this incompatibility and the consequent inability to generate the graph. Before simulating the model, the users must set the following parameters: pipe length L_1, hydraulic diameter $d_{h,1}$, cross-sectional area $A_{c,1}$, friction factor f_1, and minor loss coefficient $k_{L,1}$. In case of multiple-node pipes, a function divides the total length L_1 for each node.

The dynamics of single-phase pipes are then computed though Eq. 2.12, while the dynamics of two-phase pipes come from Eqs. 2.28 and 2.29, neglecting the term related to heat transfer in both cases.

Heat exchangers

Heat exchangers are modeled as long circular horizontal tubes and are classified as single-phase to single-phase, single-phase to two-phase, and two-phase to two-phase. Users choose:

- name of the component graph;
- type, flow configuration (counterflow or parallel flow) and number of basic elements of the heat exchanger;
- fluid type in both sides of the heat exchanger;
- material of the wall.

Each basic element is composed by one node for the solid node and each fluid node. Figure 2.8 depicts the basic element of a single-phase to two-phase heat exchanger. Therefore, heat exchangers with multiple basic elements are obtained by connecting each fluid node of one basic element with the fluid node of the same type of another basic element. Figure 2.4 and Figure 2.5 show the graphs of a single-phase to single-phase heat exchanger and a two-phase to two-phase heat exchanger, each composed of two basic elements and operating in a counterflow configuration.

For each fluid flow, the parameters to be configured include: total length L, hydraulic diameter d_h, cross-sectional area A_c, heat transfer surface area between the fluid and the heat exchanger wall A_w, friction factor f, and minor loss coefficient k_L. Moreover, the total mass of the heat exchanger wall m_w needs to be specified.

In a similar manner to the pipes, in case of multiple nodes for the same fluid, a function automatically divides the total length L, the heat transfer surface area A_w, and the mass of the wall m_w for each node.

User can choose among different correlations, summarized in Table 2.1, to compute the convective heat transfer coefficients. Each correlation uses the thermodynamic properties of the fluid within the involved fluid node undergoing heat exchange and a mass flow rate value. Within the toolbox, this mass flow rate value is computed as the average of the incoming and outgoing mass flow rates from the node. Furthermore, a function for smoothing is employed to reconcile calculated values in the transitional region between subcritical and supercritical conditions within two-phase fluids.

It is important to highlight the option of selecting a *Regression* method, aligned with the method proposed in [57, 85]. This choice aims to reduce the risk of encountering numerical issues stemming from potential discontinuities in the correlations. In this case, users are prompted to input a lookup table containing smoothed heat transfer coefficients. This table is then employed within the simulation function to calculate the interpolated value corresponding to the considered mass flow rate.

Table 2.1: Convective heat transfer coefficient correlations.

Flow type	Fluid type/state	Correlation
Single-phase flow	Air	Regression
		Colburn j-factor[2]
	Water	Regression
		Sieder and Tate [86]
		Gnielinski [87]
Two-phase flow	Subcritical	Regression
		Sieder and Tate [86]
	Supercritical	Regression
		Sieder and Tate [86]
		Liu [88]

Tanks

Tank model is defined by setting the number of nodes and the number of inlet and outlet ports of each node. The parameters to be set include:

- total volume V, which is then divided for each node;
- hydraulic diameter d_h, cross-sectional area A_c and minor loss coefficient k_L of outlet ports.

[2]Convective heat transfer coefficient α computed using Colburn j-factor:

$$j = 0.023\, Re^{-0.2},\ \alpha = \frac{j\, \frac{\dot{m}}{A_c}\, c_p}{Pr^{2/3}},$$

where Re and Pr are Reynolds and Prandtl numbers, respectively.

Figure 2.11 shows an example of tank considering a single-phase fluid. The tank includes three internal nodes, and the first and third nodes present an inlet and an output port. As introduced in subsection 2.3.3, single-phase fluids are considered incompressible, and the incoming and outgoing mass flow rates are either set by inputs or calculated by mass flow device routines. Therefore, the simulation function ensures that the sum of incoming mass flow rates equals the sum of outgoing mass flow rates during simulation. This allows for computing the mass flow rate flowing between internal tank nodes by simply applying mass balance equations.

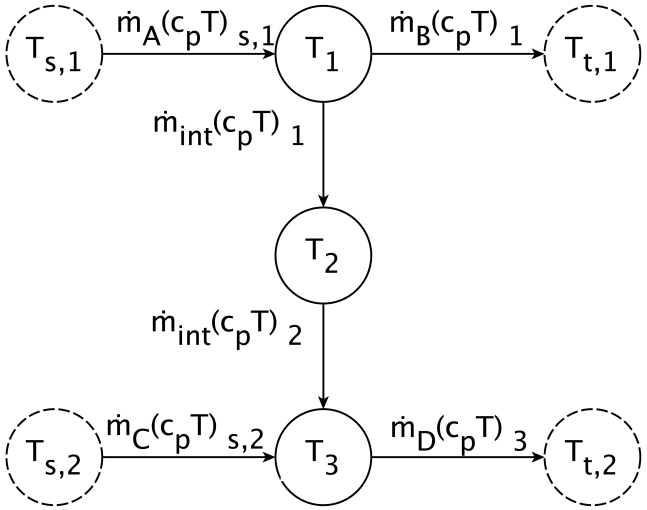

Figure 2.11: Single-phase tank with three internal nodes, two inlet ports and two outlet ports.

For tanks containing two-phase fluids, it is not necessary to adhere to such a condition, as it is ensured by the mass and conservation equations. In this case, the mass flow rate between two fluid nodes is computed using Eq. 2.33.

Separators

The separator is modeled as a vertical cylindrical component. Its model consists of a single internal two-phase fluid node and must include at least one inlet port and one outlet port. Users must set:

- diameter d and height h of the separator, from which the volume V is obtained;
- heights of inlet and outlet ports;
- a dataset consisting of two columns: the first column records volume fraction values paired with internal height fraction values in the second column. During each simulation step, this dataset is used to calculate the liquid-vapor interface height, allowing for versatile modeling of separators with varying geometries;
- hydraulic diameter d_h, cross-sectional area A_c and minor loss coefficient k_L of outlet ports, used to compute the mass flow rate using Eq. 2.33.

During simulation, the state variables of the internal node help establish the fluid properties under saturated conditions. Consequently, the density of the saturated liquid phase aids in calculating the liquid volume within the separator. This calculated volume, in turn, determines the height of the liquid-vapor interface. Subsequently, this value is compared with the height of each outlet port to derive the properties of the two-phase fluid exiting the separator:

- if the internal node is in a two-phase state and the height of the port is equal to or greater than the liquid-vapor interface height, the fluid exits the separator in saturated vapor conditions;
- if the internal node is in a two-phase state and the height of the port is smaller than the liquid-vapor interface height, the fluid exits the separator in saturated liquid conditions;
- if the internal node is in a state of subcooling or superheating, the properties of the exiting fluid mirror those of the internal node.

As will be discussed later in this section, by closing a loop between one of the outlets and one of the inlets and inserting a heat exchanger within the loop, this component can be coupled with the natural convection mechanism that drives mass transport within the loop.

Heat sources

Heat sources are represented as sources that can be linked to nodes of any type. The associated energy flow is integrated into the energy balance of the connected node.

The following models for mass flow devices are incorporated:

Fans

The toolbox allows users to incorporate the model of one or multiple fans in parallel between two single-phase nodes where the fluid is air. After specifying the edge for the fan model, a routine logs all the nodes and edges within the air circuit where the fan is placed (v_1 and v_2 in Figure 2.12). It calculates the mass flow rate $\dot{m}_{fan}$ needed for the the pressure rise Δp_{fan} to equalize the total pressure losses Δp_{loss} across the involved nodes in the circuit.

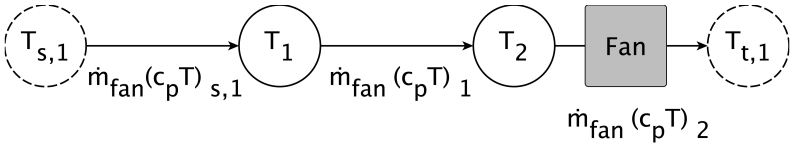

Figure 2.12: Fan circuit graph.

At each step, the algorithm involves using a trial value Δp^*_{fan} to determine a corresponding value $\dot{m}^*_{fan}$. From Δp^*_{fan} it is possible to compute the pressure coefficient ψ_{fan}:

$$\psi_{fan} = \frac{\Delta p^*_{fan}}{\rho_i \, \omega^2_{fan} \, d^2_{fan}}, \tag{2.35}$$

where:

- ρ_i is the density of the fluid entering the fan (ρ_2 referring to Figure 2.12), expressed in $\mathrm{kg\,m^{-3}}$;
- $\omega_{fan} = 2\,\pi\,n_{fan}/60$ denotes the fan rotational speed in $\mathrm{rad\,s^{-1}}$, computed from the rotational speed n_{fan} measured in rpm;

- d_{fan} represents the fan impeller diameter in m.

The pressure coefficient is then used to calculate the flow coefficient ϕ_{fan} using the polynomial:

$$\phi_{fan} = \sum_{k=0}^{8} p_{\phi,k}\, \psi_{fan}^{k}, \tag{2.36}$$

with the coefficients $[p_{\phi,0}, \ldots, p_{\phi,8}]$ drawn from manufacturers data. With ϕ_{fan}, the volumetric flow rate $\dot{V}_{fan}$ can be derived:

$$\dot{V}_{fan}^{*} \;=\; 3600\, \phi_{fan}\, \omega_{fan}\, d_{fan}^{3}, \tag{2.37}$$

and therefore the mass flow rate $\dot{m}_{fan}^{*}$:

$$\dot{m}_{fan}^{*} \;=\; \frac{\rho_i\, \dot{V}_{fan}^{*}}{3600}. \tag{2.38}$$

This value is then utilized to calculate the pressure losses Δp_{loss}^{*} across the nodes, computed as the summation of losses across each node. This computation proceeds as follows:

$$\Delta p_{loss}^{*} \;=\; \sum_{i}^{N_{air,nodes}} \frac{1}{2\,\rho_i} \left(\frac{\dot{m}_{fan}^{*}}{A_{c,i}} \right)^{2} \left(\frac{L_i\, f_i}{d_{h,i}} + k_{L,i} \right), \tag{2.39}$$

where:

- $N_{air,nodes}$ is the number of nodes in the air circuit;
- A_c, i, L_i, $d_{h,i}$, f_i, and $k_{L,i}$ are parameters of each node supplied by users;
- ρ_i is the density of the fluid.

If there are multiple fans in parallel, the steps outlined in Eqs. 2.35-2.38 are carried out for each fan. The resulting $\dot{m}_{fan}^{*}$ represents the summation of the mass flow rates from each individual fan.

The process iterates, adjusting the value of Δp_{fan}^{*} until it aligns with Δp_{loss}^{*}, thereby yielding $\dot{m}_{fan}$. This value is then associated with all the edges in the air circuit.

Ultimately, the power consumption P_{fan} of each fan is computed using:

$$P_{fan} = \frac{\Delta p_{fan} \dot{V}_{fan}}{3600\, \eta_{fan}}, \tag{2.40}$$

where η_{fan} is the total efficiency of the fan, given by:

$$\eta_{fan} = \sum_{k=0}^{8} p_{\eta,k}\, \phi_{fan}^{k}, \tag{2.41}$$

with the coefficients $[p_{\eta,0}, \ldots, p_{\eta,8}]$ obtained from the efficiency curves provided by the manufacturer.

Notably, the rotational speed n_{fan} can be treated either as a boundary condition or as user input.

Pumps

In the current version of the toolbox, pumps are solely modeled as input parameters within the model and can function as both boundary conditions and manipulable variables. Once users designate the single-phase nodes (containing liquids) between which the pump is to be placed, a routine identifies the nodes and edges comprised in the circuit in which the pump is situated. Users are required to set the value of the mass flow rate processed by the pump. This value is then associated with all other edges within the circuit.

Compressors

Users include a compressor model by specifying the two-phase advective edge that represents it. The model is coupled to two existing pipe models which calculate the necessary inlet and outlet pressure dynamics for determining mass flow rate. Automatically, the toolbox adds a new source linked to the head node, depicted in Figure 2.13, representing the power introduced into the fluid by the compressor's action. A routing computes the specific enthalpy $h^{*}_{head,is}$ from the values of the pressure in the head node p_{head} and the specific entropy calculated in the tail node from the state variables p_{tail}

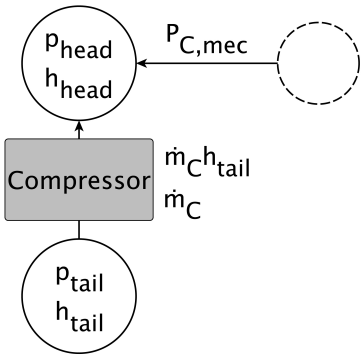

Figure 2.13: Compressor graph.

and h_{tail}. This value is used to determine the isoentropic increase in the specific enthalpy $\Delta h_{is} = h^*_{head,is} - h_{tail}$, which leads to:

$$h^*_{head} = h_{tail} + \frac{\Delta h_{is}}{\eta_{is}}, \tag{2.42}$$

where η_{is} is the compressor isoentropic efficiency.

Then, the mass flow rate sourced by the compressor is given by:

$$\dot{m}_C = \eta_v \, \rho_{tail} \, V_C \, \frac{n_C}{60}, \tag{2.43}$$

where:

- η_v is the compressor volumetric efficiency;
- ρ_{tail} is the density of the two-phase fluid in the tail node, in $\mathrm{kg\,m^{-3}}$;
- V_C is the compressor displacement volume, expressed in $\mathrm{m^3}$;
- $\frac{n_C}{60}$ is the rotational speed measured in rps.

Therefore, the power $P_{C,mec}$ introduced into the fluid is computed as:

$$P_{C,mec} = \dot{m}_C \, (h^*_{head} - h_{tail}), \tag{2.44}$$

while the total power consumption P_C of the compressor is:

$$P_C = \frac{P_{C,mec}}{\eta_{mec}}, \tag{2.45}$$

where η_{mec} is the mechanical efficiency.

Users must set the displacement V_C and can choose between setting each efficiency η as a constant or providing the constant terms $[p_{\eta,0}, \ldots, p_{\eta 8}]$ of the following polynomial, which can be obtained from manufacturer data:

$$\eta = \sum_{k=0}^{8} p_{\eta,k}\, r_p^k, \tag{2.46}$$

with $r_p = p_{head}/p_{tail}$ representing the pressure ratio between the head and tail nodes pressure.

Finally, the rotational speed n_C can be handled either as a boundary condition or as user input.

Valves

Similarly to compressors, valves model is inserted between two existing two-phase fluid nodes. The corresponding graph is illustrated in Figure 2.14.

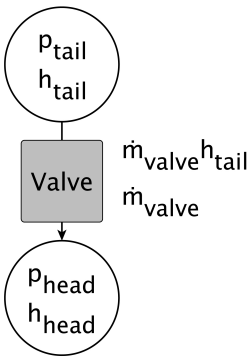

Figure 2.14: Valve graph.

The mass flow rate $\dot{m}_{valve}$ flowing through the valve is computed as:

$$\dot{m}_{valve} = C_q \, A_o \, \frac{\sqrt{2 \, \rho_{tail} \, (p_{tail} - p_{head})}}{k_{valve}}, \tag{2.47}$$

where:

- $C_q = 1/\sqrt{\zeta_{valve}}$ stands for the maximum flow coefficient and ζ_{valve} for the pressure drop coefficient;
- $A_o = o_{valve} \, A_{c,valve}$ is the current cross-sectional area, calculated from the opening ratio $o_{valve} = [0-1]$ and the maximum cross-sectional area $A_{c,valve}$, in m^2;
- ρ_{tail} denotes the density of the two-phase fluid in the tail node, measured in $\mathrm{kg\,m^{-3}}$;
- p_{tail} and p_{head} represent the pressure in the tail and head nodes, respectively, expressed in Pa;
- k_{valve} signifies the pressure loss gain, which can be used to rescale the pressure loss through the valve.

Users are asked to provide all the geometric parameters and coefficients, and can use the opening ratio o_{valve} either as a boundary condition or as input.

Finally, another mechanism for transporting two-phase fluid mass is included in the toolbox:

Natural circulation effect

When a heat exchanger forms a closed loop with a separator, the natural convection effect of two-phase fluids can be simulated. This modeling provides the mass flow rate entering the loop induced by the density gradient determined by heat transfer in the exchanger. This gradient results in a difference in static pressure between the liquid and vapor, created between the inlet and outlet of the heat exchanger. Figure 2.15 illustrates the

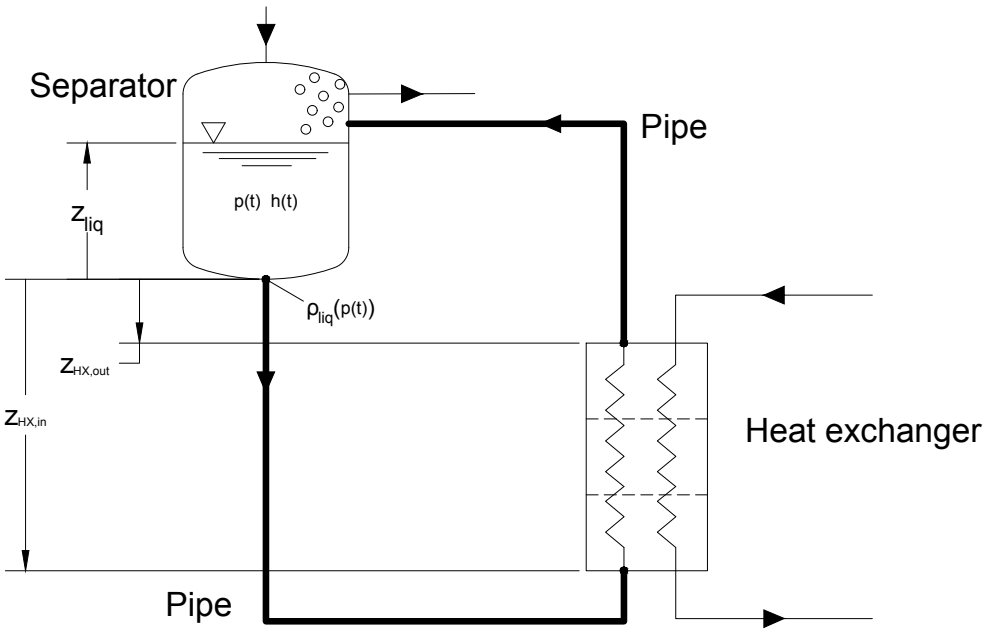

(a) Schematic.

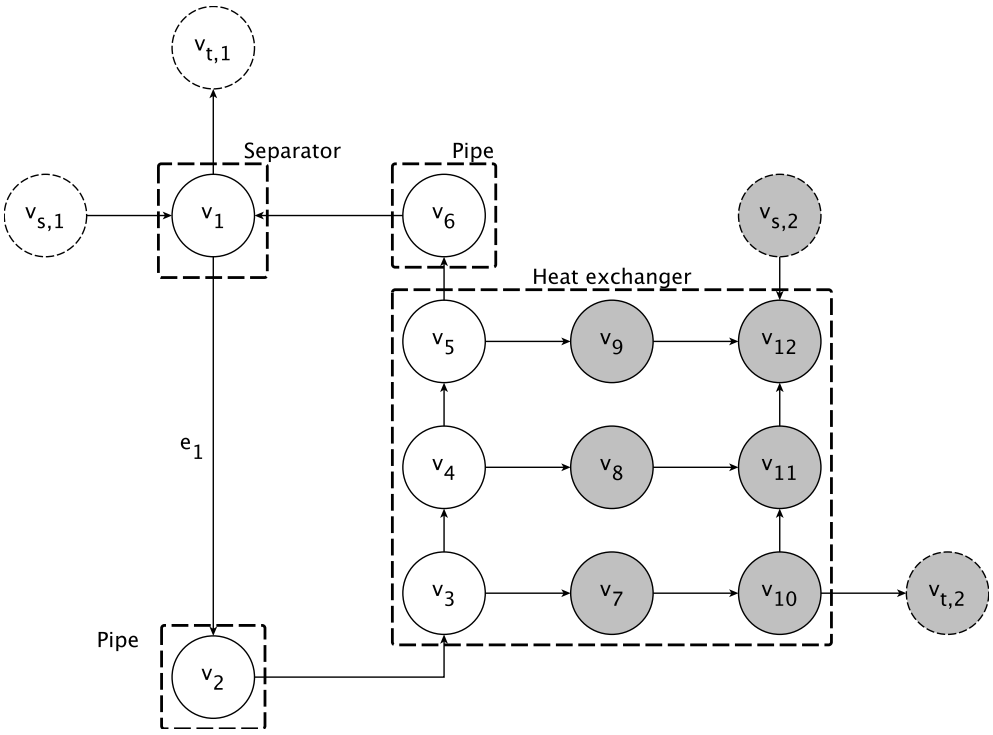

(b) Graph.

Figure 2.15: Natural circulation circuit loop.

schematic (Figure 2.15a) and the corresponding graph (Figure 2.15b) of a subsystem comprising a separator and a heat exchanger. They are interconnected through two pipes, forming a closed loop consisting of the fluid node of the separator v_1, three two-phase fluid nodes of the heat exchanger $v_3 - v_5$, and the nodes of the pipes v_2 and v_6.

The pressure increase, denoted as Δp_{nc}, arising from the density gradient, is estimated through a similar approach outlined in a prior publication [72]. In the present method, Δp_{nc} is directly proportional to the sum of products obtained by multiplying the differences between inlet and outlet heights of each component (measured from the bottom of the separator) with their corresponding fluid densities.

The liquid-vapor interface height z_{liq} is determined from the variable states of the separator node and multiplied by the density of the liquid phase ρ_{liq} within the separator. For other nodes in the loop, influenced by pressure losses and heat exchange, their densities are multiplied by the differences between inlet and outlet heights of the respective component. In cases where a component is discretized into multiple nodes, the density of each node is multiplied by the distance between the inlet and outlet heights. An exception is observed with the last node of the loop (v_6 in Figure 2.15b), associated with the difference between its inlet height and the liquid-vapor interface in the separator. The formulation can be generalized as follows:

$$\Delta p_{nc} = g \left[\rho_{liq}(z_{liq} - z_{1,out}) + \sum_{k=2}^{N_{loop}-1} \rho_k(z_{k,in} - z_{k,out}) + \rho_{n_{loop}}(z_{n_{loop},in} - z_{liq}) \right], \tag{2.48}$$

where N_{loop} is the number of nodes in the loop, $z_{1,out} = 0$ and $z_{k+1,in} = z_{k,out}$.

Therefore, once the graph is defined, users have to declare if they want to consider the natural circulation effect in the loop. If so, they must provide geometric characteristics regarding the heights of the inlet and the outlet of each component.

The calculation of the pressure increase is performed by a specific routine. Its outcome is then summed with the pressure at the tail node of edge e_1 to

determine the mass flow rate within that edge, using the momentum equation (Eq. 2.33).

2.5 Chiller Graph Modeling

The MCGM Toolbox is employed to model the chiller system introduced in Section 2.1. The associated graph, depicted in Figure 2.16, encompasses all the components visualized in Figure 2.1. It must be noted that the natural circulation effect is considered in the refrigerant loop composed by v_{LPR}, v_{Pipe6}, $v_{FE,1}$, $v_{FE,4}$, $v_{FE,7}$, and v_{Pipe7}.

As summarized in Table 2.2, the graph is composed of a total of 40 internal nodes, 18 of which have two states and 22 with one state, totaling 58 states in the dynamic model. The system comprises three sources, of which two, T_{air} and $\dot{Q}_{load}$, are treated as boundary conditions, and one, $P_{C,mec}$, is related to the compressor model. Finally, there are three input signals corresponding to the manipulable variables of the mass flow devices: the compressor speed n_C, the speed of the four axial fans n_{fan}, and the opening ratio of the valve o_{BPV}.

In the following subsections, information will be provided about the parameter values of the model components, with a particular focus on the method used to derive certain quantities for the gas-cooler.

2.5.1 Pipes

The chiller model incorporates most of the connecting pipes, acknowledging their non-negligible thermal capacity. Pipes are modeled as illustrated in subsection 2.4.2. Only one node for each pipe is considered, and their parameters are outlined in Table 2.3.

2.5.2 Heat exchangers

The gas-cooler (GC), the internal heat exchanger (IHX), and the flooded evaporator (FE) are a finned tube heat exchanger, a tube-in-tube heat exchanger in counterflow configuration, and a single pass brazed plate heat

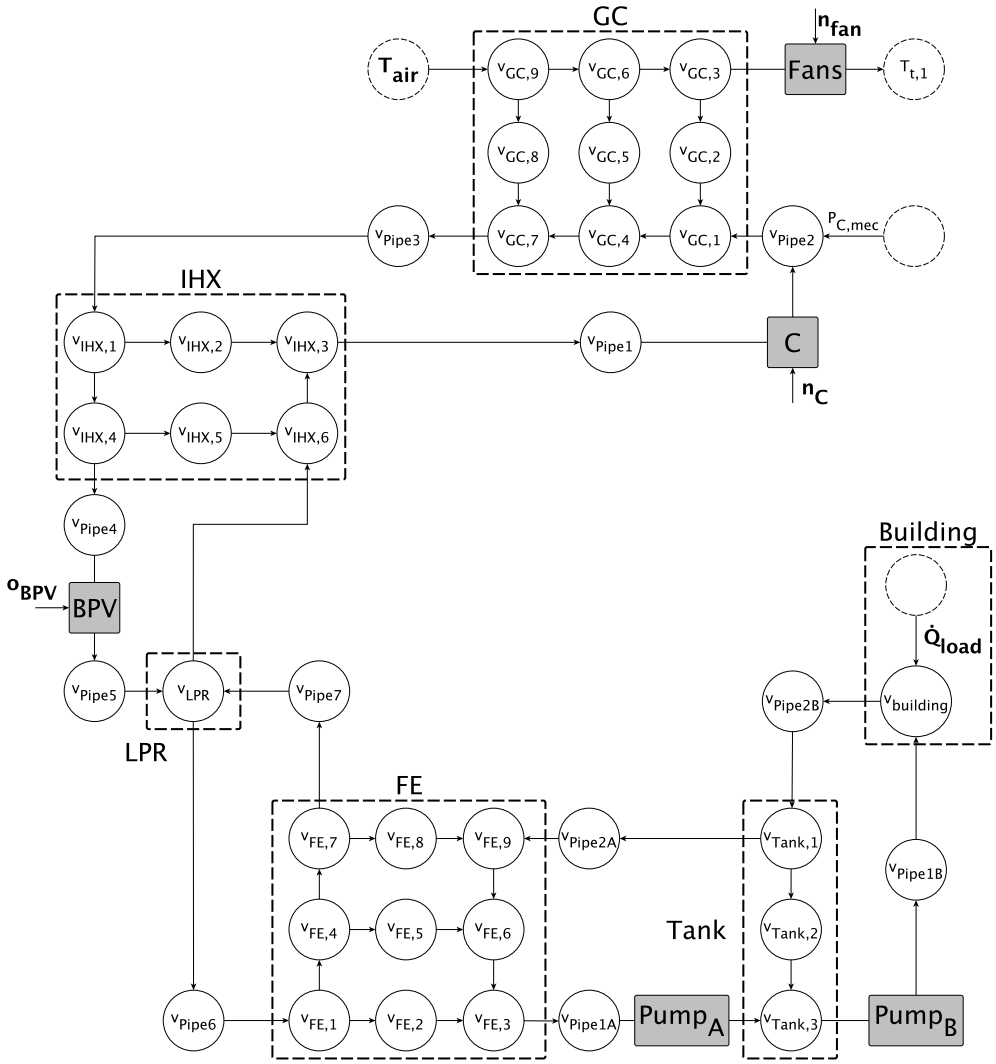

Figure 2.16: Chiller system graph.

exchanger in counterflow configuration, respectively. Therefore, the corresponding models can be arranged in counterflow configuration. Both the gas-cooler and the flooded evaporator comprises three basic elements, and function as two-phase to single-phase heat exchangers. Conversely, the internal heat exchanger is a two-phase to two-phase heat exchanger, obtained by combining two basic elements.

Table 2.4 summarizes the parameters considered in the current model for

Table 2.2: Chiller system graph data.

Node type	Node	Material/Fluid	Component type	Component name
Two-phase nodes	v_{Pipe1}	R744	Pipe	Pipe1
	v_{Pipe2}	R744	Pipe	Pipe2
	$v_{GC,1}$	R744	Heat exchanger	GC
	$v_{GC,4}$	R744	Heat exchanger	GC
	$v_{GC,7}$	R744	Heat exchanger	GC
	v_{Pipe3}	R744	Pipe	Pipe3
	$v_{IHX,1}$	R744	Heat exchanger	IHX
	$v_{IHX,3}$	R744	Heat exchanger	IHX
	$v_{IHX,4}$	R744	Heat exchanger	IHX
	$v_{IHX,6}$	R744	Heat exchanger	IHX
	v_{Pipe4}	R744	Pipe	Pipe4
	v_{Pipe5}	R744	Pipe	Pipe5
	v_{LPR}	R744	Separator	LPR
	v_{Pipe6}	R744	Pipe	Pipe6
	$v_{FE,1}$	R744	Heat exchanger	FE
	$v_{FE,3}$	R744	Heat exchanger	FE
	$v_{FE,7}$	R744	Heat exchanger	FE
	v_{Pipe7}	R744	Pipe	Pipe7
Single-phase nodes	$v_{GC,3}$	Air	Heat exchanger	GC
	$v_{GC,6}$	Air	Heat exchanger	GC
	$v_{GC,9}$	Air	Heat exchanger	GC
	$v_{FE,3}$	Water	Heat exchanger	FE
	$v_{FE,6}$	Water	Heat exchanger	FE
	$v_{FE,9}$	Water	Heat exchanger	FE
	v_{Pipe1A}	Water	Pipe	Pipe1A
	$v_{Tank,1}$	Water	Tank	Tank
	$v_{Tank,2}$	Water	Tank	Tank
	$v_{Tank,3}$	Water	Tank	Tank
	v_{Pipe1B}	Water	Pipe	Pipe1B
	$v_{Building}$	Water	Tank	Building
	v_{Pipe2B}	Water	Pipe	Pipe2B
	v_{Pipe2A}	Water	Pipe	Pipe2A
Solid nodes	$v_{GC,2}$	AISI316	Heat exchanger	GC
	$v_{GC,5}$	AISI316	Heat exchanger	GC
	$v_{GC,8}$	AISI316	Heat exchanger	GC
	$v_{IHX,2}$	Copper	Heat exchanger	IHX
	$v_{IHX,5}$	Copper	Heat exchanger	IHX
	$v_{FE,2}$	AISI316	Heat exchanger	FE
	$v_{FE,5}$	AISI316	Heat exchanger	FE
	$v_{FE,8}$	AISI316	Heat exchanger	FE

each side of these heat exchangers, detailing the total values of length L and heat transfer surface area A_w. The mass of solid material m_w of the three heat exchangers is equal to: 1299 kg for the gas-cooler, 15 kg for the internal-

Table 2.3: Pipes parameters.

	# nodes	A_c [m^2]	d_h [mm]	L [m]	f [−]	k_L [−]
Pipe1	1	4.91×10^{-4}	25	5	0.01	4
Pipe2	1	6.11×10^{-4}	27.9	30	0.01	8
Pipe3	1	6.11×10^{-4}	27.9	30	0.01	40
Pipe4	1	7.85×10^{-5}	10	2	0.01	0.1
Pipe5	1	7.85×10^{-5}	10	1	0.01	0.2
Pipe6	1	6.11×10^{-4}	27.9	2.1	0.01	12
Pipe7	1	6.11×10^{-4}	27.9	2.7	0.01	0.1
Pipe1A	1	4.91×10^{-4}	25	2	0	0
Pipe2A	1	4.91×10^{-4}	25	2	0	0
Pipe1B	1	1.96×10^{-3}	50	500	0	0
Pipe2B	1	1.96×10^{-3}	50	500	0	0

heat exchanger, and 34.9 kg for the flooded evaporator. The values L, A_w, and m_w are later divided among individual nodes, as explained in subsection 2.4.2.

For the first flow side of each heat exchanger, the specific nodes include:

- $v_{GC,1}$, $v_{GC,4}$, and $v_{GC,7}$ for the gas-cooler, which represent the internal volume of the tubes where the refrigerant flows;
- $v_{IHX,1}$ and $v_{IHX,4}$ for the internal heat exchanger;
- $v_{FE,1}$, $v_{FE,4}$, and $v_{FE,7}$ for the flooded evaporator, which represent the internal volume of the channels where the refrigerant flows.

Similarly, the corresponding nodes on the second flow side are:

- $v_{GC,3}$, $v_{GC,6}$, and $v_{GC,9}$ for the gas-cooler, which represent the internal volume of the air passages;
- $v_{IHX,3}$ and $v_{IHX,6}$ for the internal heat exchanger;
- $v_{FE,3}$, $v_{FE,6}$, and $v_{FE,9}$ for the flooded evaporator, which represent the internal volume of the channels where the water flows.

Table 2.4: Heat exchangers parameters.

		# nodes	A_c [m^2]	A_w [m^2]	d_h [mm]	L [m]	f [−]	k_L [−]
GC	Side 1	3	1.47×10^{-3}	54.8	5.94	55.4	0.01	20
	Side 2	3	7.21	1463.5	2.77	0.14	0.01	6.6
IHX	Side 1	2	5.34×10^{-4}	0.39	10	4.3	0.01	12
	Side 2	2	4.91×10^{-4}	0.34	25	4.3	0.01	1
FE	Side 1	3	1.83×10^{-2}	7.62	5.29	0.548	0.01	90
	Side 2	3	1.87×10^{-2}	7.62	5.29	0.538	0	0

Gas-cooler geometry

In the gas-cooler, the refrigerant R744 enters the first fluid side distributing itself in parallel among the tubes, and passes through the rows of the heat exchanger in a single pass. On the other side, an airflow is forced to pass externally around the tubes, through the channels created by the fins of the heat exchanger.

As will be discussed further in this dissertation, the gas-cooler is crucial in determining the performance of the chiller system. To aid the reader in understanding how design parameters of the gas-cooler impact its geometry, the derivation of the considered quantities as model parameters is described. This elucidation is essential in comprehending the intricate relationship between the design elements and the resultant configuration of the gas-cooler.

Defining subscript i for the first flow side and e for the second, the starting data are:

- length l_{GC};
- internal diameter of the tubes $d_{i,GC}$ and tube thickness $t_{t,GC}$, from witch the external diameter $d_{e,GC} = d_{i,GC} + 2\,t_{t,GC}$ is drawn;
- number of rows of tubes $N_{R,GC}$ and number of tubes for each row $N_{t,GC}$;
- row pitch $p_{R,GC}$, tube pitch $p_{t,GC}$, fin pitch $p_{f,GC}$, and fin thickness $t_{f,GC}$,
- wall density $\rho_{w,GC}$.

The following sizes can be calculated:

- tubes total length

$$l_{t,tot,GC} = l_{GC}\, N_{R,GC}; \tag{2.49}$$

- total number of tubes $N_{t,tot,GC}$:

$$N_{t,tot,GC} = N_{t,GC}\, N_{R,GC}; \tag{2.50}$$

- height of the gas-cooler h_{GC}:

$$h_{GC} = N_{t,GC}\, p_{t,GC}; \tag{2.51}$$

- width of the gas-cooler w_{GC}:

$$w_{GC} = N_{R,GC}\, p_{R,GC}; \tag{2.52}$$

- frontal area (total cross sectional area) with respect to the air flow $A_{fr,GC}$:

$$A_{fr,GC} = l_{GC}\, w_{GC}; \tag{2.53}$$

- ratio between the net cross-sectional area and the total cross sectional area σ_{GC}:

$$\sigma_{GC} = \frac{(p_{t,GC} - d_{e,GC})\,(p_{f,GC} - t_{f,GC})}{p_{t,GC}\, p_{f,GC}}; \tag{2.54}$$

- net cross-sectional area $A_{fr,n,GC}$:

$$A_{fr,n,GC} = \sigma_{GC}\, A_{fr,GC}; \tag{2.55}$$

- internal surface area $A_{i,GC}$:

$$A_{i,GC} = \pi\, d_{i,GC}\, l_{GC}\, N_{t,tot,GC}; \tag{2.56}$$

- external surface area $A_{e,GC}$:

$$A_{e,GC} = \left[2 \left(p_{t,GC}\, p_{R,GC} - \pi \frac{d_{e,GC}^2}{4} \right) + \pi d_{e,GC} (p_{f,GC} - t_{f,GC}) \right] \frac{l_{GC}}{p_{f,GC}}\, N_{t,tot,GC}; \tag{2.57}$$

- fin surface area $A_{e,f,GC}$:

$$A_{e,f,GC} = 2 \left(p_{t,GC}\, p_{R,GC} - \pi \frac{d_{e,GC}^2}{4} \right) \frac{l_{GC}}{p_{f,GC}}\, N_{t,tot,GC}; \tag{2.58}$$

- wall volume $V_{w,GC}$:

$$V_{w,GC} = \pi \left(\frac{d_{e,GC}^2 - d_{i,GC}^2}{4} \right) \frac{l_{GC}}{p_{f,GC}}\, N_{t,tot,GC} + \frac{A_{e,f,GC} t_{f,GC}}{2}; \tag{2.59}$$

Therefore, the overall parameters of the first fluid side can be set as:

- cross-sectional area $A_c = \pi d_{i,GC}^2 / 4$;
- heat transfer surface area $A_w = A_{i,GC}$;
- hydraulic diameter $d_h = d_{i,GC}$;
- total length $L = l_{t,tot,GC}$.

The corresponding values for the second fluid side are:

- cross-sectional area $A_c = A_{fr,n,GC}$;
- heat transfer surface area $A_w = A_{e,GC}$;
- hydraulic diameter $d_h = 4\, A_c\, L / A_w$;
- total length $L = w_{tot,GC}$.

Finally, the mass of the total mass of the solid nodes is $m_w = \rho_{w,GC}\, V_{w,GC}$.

2.5.3 Tanks

Tank

The water tank is modeled through three single-phase nodes, where both the first and the third have one inlet and one outlet port. The total volume of the tank $V = 1\,\mathrm{m}^3$, while the parameters regarding the fluid ports can be neglected, since the mass flow rate in the water circuit is not computed by any pump routine but provided as an external input parameter.

Building

The building is represented by a single-phase node featuring one inlet and one outlet port. The volume of this tank is $V = 0.1\,\mathrm{m}^3$, and similarly, the details concerning the fluid ports can be disregarded in this scenario as well.

2.5.4 Separator

The low pressure receiver (LPR) is an horizontally oriented cylindrical carbon steel receiver, with an internal volume $0.167\,\mathrm{m}^3$ and an internal diameter of 406 mm. However, the model interprets the receiver as a vertically oriented cylinder, hence treating the internal diameter as the height (h) of the volume. Consequently, a dataset describing the variation of the liquid-vapor interface is derived to accommodate this representation

The outlet port that connects v_{LPR} with v_{Pipe6} is collocated at the bottom of the separator, while the ports that lead to $v_{IHX,6}$ is collocated at the top and, therefore, the corresponding eight is equal to 406 mm.

Moreover, v_{LPR} forms a closed loop with Pipe6, the flooded evaporator FE, and Pipe7, and within this loop the natural circulation effect is considered. Table 2.5 summarizes the inlet/outlet heights associated with each node in the loop, and use to compute the pressure increase Δp_{nc} using Eq. 2.48.

Table 2.5: Inlet and outlet heights related to the nodes within the natural circulation circuit loop connected to the LPR.

	$z_{k,in}$ [m]	$z_{k,out}$ [m]
v_{LPR}	z_{liq}	0
v_{Pipe6}	0	-1.31
$v_{FE,1}$	-1.31	-1.13
$v_{FE,4}$	-1.13	-0.96
$v_{FE,7}$	-0.96	-0.78
v_{Pipe7}	-0.78	z_{liq}

2.5.5 Mass flow devices

Fans

The chiller system comprises four axial fans equal to each other and working in parallel, with an impeller diameter of $d_{fan} = 905\,\text{mm}$ and a nominal rotational speed $n_{fan,0} = 530\,\text{rpm}$ at a power supply frequency of 50 Hz.

Table 2.6 outlines the constant terms of the polynomial adopted to calculate the flow coefficient ϕ_{fan} with Eq 2.36. Similarly, Table 2.7 presents the values of the polynomial coefficients used in Eq. 2.41 to compute the total efficiency of the fan η_{fan}.

Table 2.6: Constant terms of the flow coefficient polynomial.

	$p_{\phi,0}$	$p_{\phi,1}$	$p_{\phi,2}$	$p_{\phi,3}$	$p_{\phi,4}$	$p_{\phi,5}$	$p_{\phi,6}$	$p_{\phi,7}$	$p_{\phi,8}$
ϕ_{fan}	0.1151	-0.9646	-118.6	8084	-228739	0	0	0	0

Table 2.7: Constant terms of the total fan efficiency polynomial.

	$p_{\eta,0}$	$p_{\eta,1}$	$p_{\eta,2}$	$p_{\eta,3}$	$p_{\eta,4}$	$p_{\eta,5}$	$p_{\eta,6}$	$p_{\eta,7}$	$p_{\eta,8}$
η_{fan}	-0.0554	-0.7410	265	-2194	0	0	0	0	0

Pumps

In subsequent sections of this dissertation, PumpA and PumpB are treated as external input parameters, each set with a fixed mass flow rate of $6\,\text{kg}\,\text{s}^{-1}$ and $1.89\,\text{kg}\,\text{s}^{-1}$, respectively.

Compressor

The compressor under consideration (C) is a reciprocating, semi-hermetic, single-stage compressor. It has a displacement volume of $V_C = 180.69\,\mathrm{cm}^3$ and a nominal rotational speed of $n_{C,0} = 1450\,\mathrm{rpm}$ when powered with a frequency of 50 Hz. The constant terms of the polynomials (Eq. 2.46) used to compute the efficiencies of the compressor are summarized in Table 2.8.

Table 2.8: Constant terms of the compressor efficiency polynomials.

	$p_{\eta,0}$	$p_{\eta,1}$	$p_{\eta,2}$	$p_{\eta,3}$	$p_{\eta,4}$	$p_{\eta,5}$	$p_{\eta,6}$	$p_{\eta,7}$	$p_{\eta,8}$
η_{is}	-2.0847	4.5377	-3.0425	1.0760	-0.2129	0.0223	-0.0010	0	0
η_v	0.6086	0.3208	-0.1460	0.0232	-0.0013	0	0	0	0
η_{mec}	0.8889	0.0065	-0.0004	-0.0002	0	0	0	0	0

Valve

The back-pressure valve (BPV) operates as an electrically controlled step motor valve, having a maximum opening diameter of 5.8 mm, which corresponds to a maximum cross-sectional area of $A_c = 1.06 \times 10^{-4}\,\mathrm{m}^2$. The assigned values for the pressure drop coefficient ζ_{valve} and the pressure loss gain k_{valve} are set to 2 and 1, respectively.

2.5.6 Boundary conditions and inputs

In the following sections, the temperature T_{air} of the external air entering the gas-cooler and the thermal cooling load $\dot{Q}_{load}$ provided to the building will be treated as boundary conditions. Conversely, the rotational speed of the compressor n_C, the rotational speed of the fans n_{fan}, and the opening ratio of the valve o_{BPV}, will be treated as input signals.

2.5.7 Initial conditions

The refrigerant (two-phase) nodes are categorized into two groups: high-pressure and low-pressure sides. Within the low-pressure side, a third category is represented by the node v_{Pipe1} at the compressor inlet. Consequently,

initial conditions for each category are computed starting with the predefined refrigerant mass (105 kg) and the pressure values for both sides. An iterative routine determines the specific enthalpy h_0 associated with nodes on both sides, from which the specific enthalpy in vapor-saturated condition is derived and applied to v_{Pipe1}. The resulting h_0 ensures that the total mass within the nodes matches the predefined refrigerant mass.

Initial values for air nodes are set to the initial external air temperature $T_{air}(t = 0)$, while predefined values are used for water nodes.

Finally, the temperature of the solid nodes, representing the walls of the heat exchangers, are set equal to the average value between the fluids.

2.5.8 Model Validation

The validation of the graph-based model, in the following referred to as GBM, is conducted in transient operation, comparing the thermal performance of the chiller model to a synthetic dataset generated using a dynamic model presented in [72], developed with Simcenter Amesim v2021.2. This reference model, hereafter labeled as AME, was previously validated against experimental data obtained from a real CO_2 chiller system located in a hotel in a tourist area in Northern Italy. The experimental data were collected within the MultiPACK Project (funded by the European Union's Horizon 2020 research and innovation program under grant agreement No 723137) and published in an open database [89]. For a detailed discussion on the results of this preliminary validation, the reader is referred to [72].

Four different sets of boundary conditions are considered, each obtained by combining different levels of external air temperature T_{air} and thermal load $\dot{Q}_{load}$ (refer to Table 4.1). These four sets are summarized as follows:

- LTL - LT: $\dot{Q}_{load} = 21.3\,\text{kW}$, $T_{air} = 20.7\,°\text{C}$;
- LTL - HT: $\dot{Q}_{load} = 21.3\,\text{kW}$, $T_{air} = 30.4\,°\text{C}$;
- HTL - LT: $\dot{Q}_{load} = 63.9\,\text{kW}$, $T_{air} = 20.7\,°\text{C}$;
- HTL - HT: $\dot{Q}_{load} = 63.9\,\text{kW}$, $T_{air} = 30.4\,°\text{C}$.

During simulations, these values are kept fixed while the values of the manipulable variables of the mass flow devices are varied as depicted in Figure 2.17. Two different sets of input signals are used: one for simulations at the low thermal load (LTL) value, and one for simulations at the high thermal load (HTL). In the first case, the compressor speed n_C, the fan speed n_{fan}, and the opening of the valve o_{BPV} range between 1450 and 1595 rpm, 477 and 530 rpm, and 0.08 and 0.1, respectively. In the second case, the inputs vary between 1450 and 1740 rpm, 424 and 636 rpm, and 0.07 and 0.1.

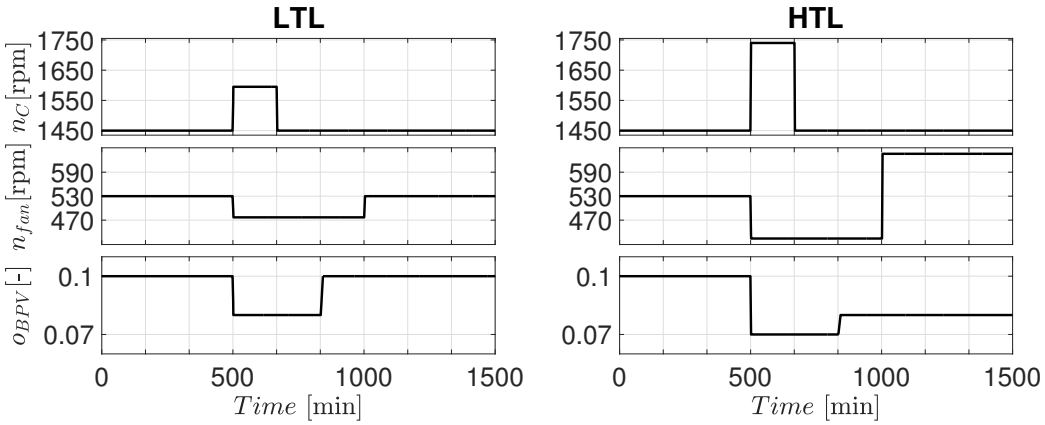

Figure 2.17: Input signals.

The validation is carried out comparing the results of both models, and, in particular, the operating pressures at the inlet and the outlet of the compressor, p_6 and p_1 respectively, the refrigerant temperature T_2 at the gas-cooler outlet, the supply water temperature T_B, the compressor power consumption P_C, the power consumption of each fan P_{fan}, and the instantaneous cooling capacity $\dot{Q}_c$ calculated according to the following equation:

$$\dot{Q}_c = \dot{m}_C \, (h_6 - h_2), \tag{2.60}$$

where $\dot{m}_C$ is the refrigerant mass flow rate provided by the compressor, h_6 is the refrigerant specific enthalpy at the compressor inlet, and h_2 is the refrigerant specific enthalpy at the gas-cooler outlet.

Figure 2.18 shows the trends of the validation variables for both the graph-based model (GBM) and the reference (AME) model for all the considered

sets of boundary conditions. The solid lines represent the results for the low temperature (LT) cases, while the dashed lines correspond to the simulations at the high temperature (HT).

Table 2.9 summarizes the mean values of graph-based model results and two summary statistics computed with respect to the results of the reference model: the mean percentage errors (MPE) are calculated to compare the refrigerant pressures p_6 and p_1, the power consumption of the compressor P_C and of each fan P_{fan}, and the instantaneous cooling capacity $\dot{Q}_c$; the mean absolute errors (MAE) are used to compare the values of the refrigerant temperature T_2 at the gas-cooler outlet and the supply water temperature T_B.

Table 2.9: Comparison between graph-based model (GBM) and Simcenter Amesim model (AME) simulation results.

		LTL		HTL	
		LT	HT	LT	HT
p_1	GBM [bar]	60.2	71.5	66.5	83.3
	MPE [%]	1	0.1	2.7	4.2
p_6	GBM [bar]	32	37.9	40.3	45.9
	MPE [%]	1	0.4	2.1	2.3
$\dot{Q}_c$	GBM [W]	23259	22328	64085	63307
	MPE [%]	-3	-2.4	-0.5	-0.2
P_C	GBM [W]	14072	16766	14844	19534
	MPE [%]	1.1	0.2	3.6	5.3
P_{fan}	GBM [W]	378	366	445	430
	MPE [%]	0.7	0.8	0.8	0.9
T_2	GBM [°C]	22.0	30.8	25.0	32.9
	MAE [°C]	0.4	0.4	1.3	1.6
T_B	GBM [°C]	-1.5	4.6	9.4	14.6
	MAE [°C]	0.1	0.4	0.5	0.5

Small differences can be observed between the trends of the graph-based model and the reference model at LTL. Conversely, slightly larger discrepancies are noticeable in the results at HTL, particularly concerning the re-

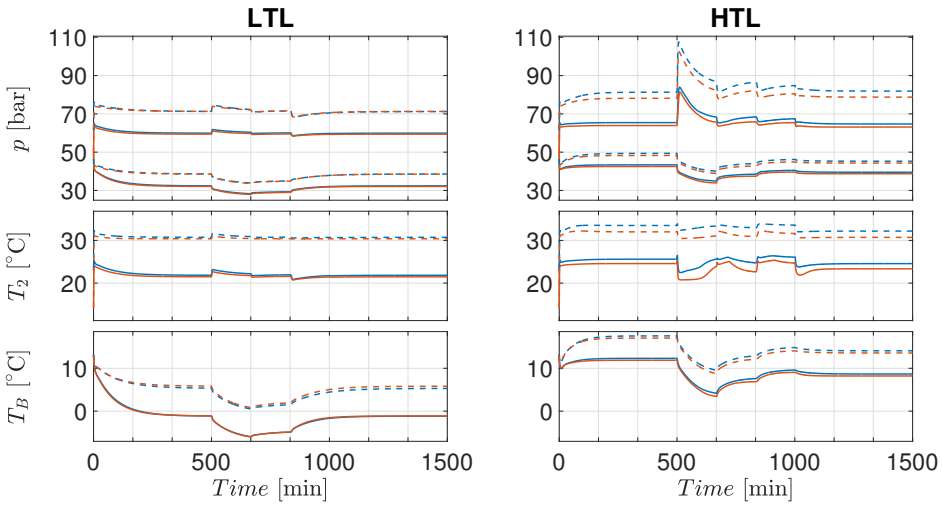

(a) Refrigerant pressures (p_1 and p_6) at the compressor inlet and outlet, refrigerant temperature T_2 at the gas-cooler outlet, and supply water temperature T_B

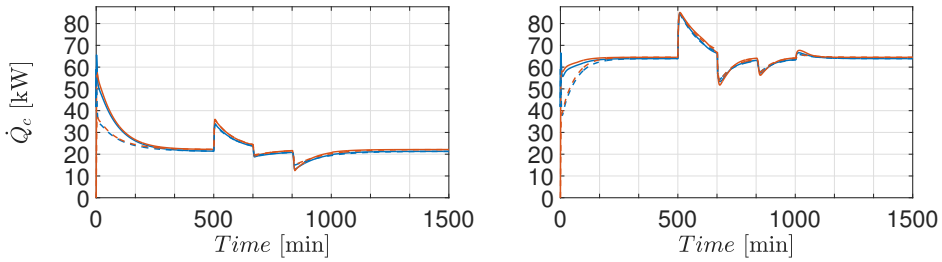

(b) Cooling capacity $\dot{Q}_c$

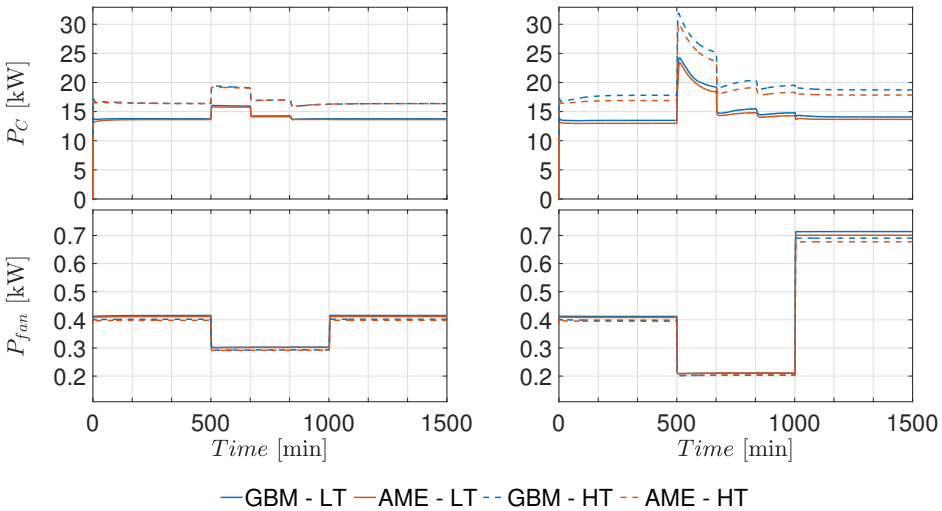

(c) Compressor power consumption P_C and power consumption P_{fan} of each fan

Figure 2.18: Comparison between graph-based model (GBM) and Simcenter Amesim model (AME) simulation results.

frigerant pressures p_6 and p_1. These differences lead to greater deviations in the compressor power consumption P_C and the refrigerant temperature T_2 at the gas-cooler outlet. In general, the GBM tends to overestimate most validation variables, with the exception of the cooling capacity, which is consistently underestimated in all cases. The maximum MPEs for the high refrigerant pressure p_1 and the low refrigerant pressure p_6 are equal to 4.2 % and 2.3 %, respectively, while the corresponding values for the power consumption of the compressor P_C and each fan P_{fan} are equal to 5.3 % and 0.9 %. Additionally, the maximum MAEs for the refrigerant temperature T_2 at the gas-cooler outlet and the supply water temperature T_B are equal to 1.6 °C and 0.5 °C, respectively. It is noteworthy that these values pertain to the set of boundary conditions HTL-HT. On the other hand, the maximum MPE (in absolute value) for the cooling capacity $\dot{Q}_c$ is equal to −3 %, and it corresponds to the set of boundary conditions LTL-LT.

2.6 Chiller Control System

In the considered CO_2-based vapor compression system, the main control objectives encompass the following aspects:

- absorption and removal of a certain amount of heat from the cooling space (i.e., the cooling demand) and rejecting that heat into the atmosphere: this can be reflected in providing a certain cooling capacity to the continuous secondary flow entering the evaporator, consequently cooling down the water in the water tank. The primary control objective is to maintain a predefined setpoint for the water outlet temperature from the tank, which is supplied to the building to meet its cooling requirements. It is noteworthy that both external ambient conditions and the mass flows and temperatures within the water loops act as measurable disturbances affecting the refrigeration system.

- Achieving the desired cooling capacity with energy efficiency as high as possible, namely, minimizing the overall power consumption.

- Satisfying operating constraints and controlling certain thermodynamic states of the refrigerant, as, for example, ensuring an adequate evaporator superheating (SH), in terms of system efficiency and preventing component failure. Indeed, an excessively high SH implies insufficient refrigerant, leading to system inefficiency; conversely, if SH is too low, it indicates a flow of liquid into the evaporator, posing a risk of compressor damage. Additionally, an appropriate value for the refrigerant high pressure and the gas-cooler outlet temperature is crucial to guarantee optimal performance of the system, especially when operating under supercritical conditions [11, 2, 12, 13, 14].

The system outputs are the refrigerant high pressure p_3, the gas-cooler outlet temperature T_2, and the supply water temperature T_B, while the system manipulable input variables are the back pressure valve opening ratio o_{BPV}, the fan rotational speed n_{fan}, and the compressor rotational speed n_C (see Figure 2.1). Due to the intrinsic complexity of the vapor compression cycle, chiller control presents challenges. The presence of multiple inputs and multiple outputs (MIMO), significant thermal inertia, possible dead times, substantial coupling among system variables (due to the effect of inputs essentially "feeding back" through the cycle), nonlinearities, and varying operating conditions complicate the control design.

To face these challenges, we employ a combined static-feedforward and feedback control architecture to ensure satisfactory performance over a wide range of operating conditions [32]. This integrated control solution maintains a balance: the static-feedforward element, based on the principle of preemptive load counter-action, operates in open-loop, taking control actions to address a specific static disturbance. Simultaneously, it allows a conventional feedback control loop (i.e., the system output is routed back as input as part of a chain of cause-and-effect that forms the loop) to dynamically accomplish the following objectives: reject unmeasured disturbances and external influences, provide set point tracking capability, and compensate for the inherent simplifications in the predictive part of the feedforward element, which may lead to imperfect preemptive disturbance rejection.

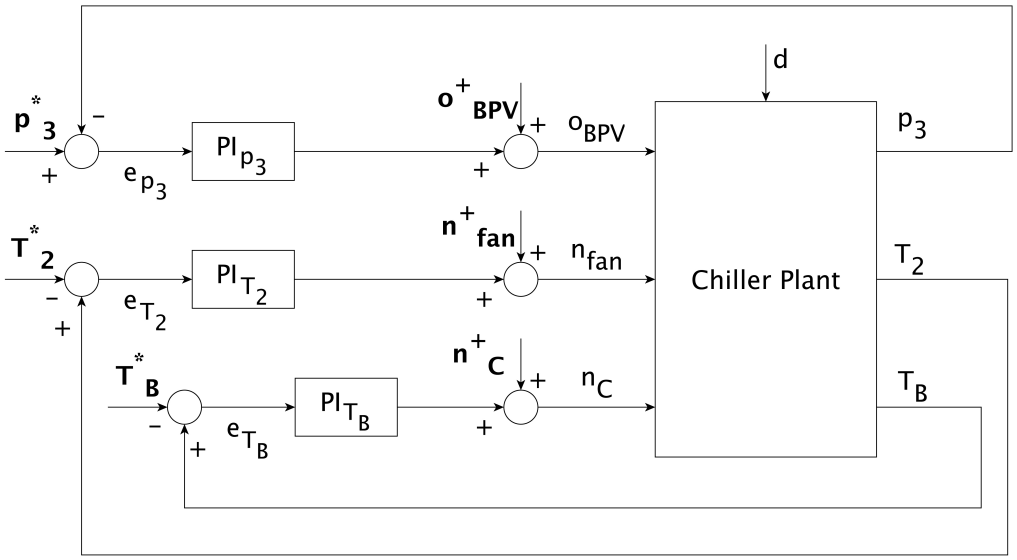

Figure 2.19: Combined feedback and feedforward control architecture; $\mathbf{o^+_{BPV}}$, $\mathbf{n^+_{fan}}$, and $\mathbf{n^+_C}$ in bold text correspond to the feedforward inputs.

In this context, we use a decentralized multi-loop architecture to regulate the three chiller outputs rather than a single centralized MIMO control loop [90, 91, 92, 93, 94, 95]. First the plant is suitable decomposed into three single-input and single-output (SISO) subsystems, then independent proportional-integral (PI) controllers and feedforward actions are designed for each subsystem. The decentralized control has the advantage of easy implementation and tuning, and it can exhibit advantage regarding reliability: if a fault occurs in another PI controller or actuator, the independent controller will persist in attempting to bring its associated variable to its set-point. Conversely, in a system heavily dependent on the coordination of all loops, the failure of one component may lead to failure of the overall structure. This risk is particularly notable in the centralized control. The reliability advantage is among the various reasons practitioners find the use of separate SISO loops appealing, as opposed to centralized or highly coordinated approaches.

The combined control architecture, Figure 2.19, includes:

Feedback with three loop actions:

CL_1 the refrigerant high pressure is regulated by the PI_{p_3} acting on the back-pressure valve opening ratio;

CL_2 the gas-cooler outlet temperature is controlled by the PI_{T_2} manipulating the fan rotational speed;

CL_3 the supply water temperature is regulated by the PI_{T_B} adjusting the compressor rotational speed.

Static feedforward with three open loop actions:

OL_1 the back pressure valve opening ratio is an output of the control co-design task;

OL_2 similarly, the fan rotational speed is obtained by solving the control co-design problem;

OL_3 the compressor rotational speed is determined to satisfy an estimation of the required cooling capacity (i.e., rejecting the disturbance on the supply water temperature T_B).

It is important to highlight that the static-feedforward tasks OL_1 and OL_2 align with the primary objective of the control design subproblem within the CCD optimization problem, as elaborated in subsequent discussions.

Chapter 3

Control Co-Design

3.1 Background

Control Co-Design (CCD) is an interdisciplinary approach that aims to optimize both the system architecture and its control policies, by addressing the intricate relationship between them and accounting for both physical and design couplings from the early stages of design [28] to satisfy overall performance, stability and robustness requirements. CCD represents a class of integrated engineering methods that can be considered as part of the Multidisciplinary Design Optimization (MDO) method [36].

High-fidelity models play an essential role in allowing CCD strategies to fully harness these attributes within thermal-fluid systems design, particularly in applications such as HVAC&R. In these systems, small alterations in specific physical component design variables can trigger significant impacts on the complex, nonlinear phenomena involved, such as heat transfer [50]. Hence, accurately reproducing the dynamics involved, especially the interactions among system components and between the plant and its control system, becomes pivotal in ensuring the reliability and accuracy of the design process within such complex systems. Moreover, high-fidelity models play a crucial role in mitigating uncertainty sources that could potentially impede successful implementation of CCD methods [39]. By accurately representing system dynamics and interactions, these models contribute significantly to

enhancing the reliability and effectiveness of the CCD approach [96].

Managing uncertainties within CCD methodologies is indeed a critical aspect due to the deterministic nature of most methods versus the inherent uncertainties within CCD problems (e.g., optimization variables, problem data, disturbances, noise, etc.). This discrepancy often leads to unreliable solutions when applying CCD optimization techniques in practical scenarios, as highlighted by [36, 37]. The significance of addressing these uncertainties is emphasized in literature, with various authors proposing solutions to enhance the robustness and practical applicability of CCD methodologies [39, 97, 98]. This effort reflects the continuous endeavor to strengthen these methodologies for real-world deployment.

Control Co-Design has been applied across various engineering problems, notably in the design of aircraft [99, 100, 98, 52], renewable energy production systems [101, 102], electric vehicles [103], and more [104, 105, 38, 106, 107]. Recently, it has captured considerable attention among researchers who have sought to implement CCD methods for designing thermal-fluid systems, particularly within the domain of HVAC&R systems.

In [43], authors introduce a co-design approach for optimizing HVAC systems by analyzing the inter-dependencies between the control algorithm and the embedded platform. It presents six control algorithms that consider sensing accuracy and examines how it correlates with both the number and positions of temperature sensors.

Nash et al. [48] address the challenges of modeling and controlling a flash boiling cooling system and proposes a combined plant and control design optimization approach to overcome these challenges. It involves deriving a nonlinear dynamic model of the system, optimizing process parameters and open loop control signal, and demonstrating the effectiveness of the approach through simulations. The potential applications of flash boiling for rapidly cooling transient heat loads are also discussed.

In [49] a novel approach is proposed for co-design of thermal-fluid systems, explicitly focusing on system efficiency measured through the entropy generation rate as a key design metric. Authors leverage a nested co-design

architecture to trade off nominal (steady-state) efficiency with transient efficiency while also ensuring robustness to high transient disturbances. They use highly parameterized nonlinear and linearized first principles models instead of empirical models, facilitating optimization across a broader range of design variables.

Vasisht et al. [44, 45] introduce a co-design framework using Bayesian Optimization for commercial building HVAC systems. This work addresses the limitations of traditional sequential approaches and oversizing guidelines, emphasizing the importance of control co-design in achieving optimal solutions and efficient operations. The co-design framework is used to optimize the number of chillers, their capacities, and switching thresholds to minimize total (capital and operational) costs and enhance energy efficiency while maintaining building cooling demand satisfaction. The optimization is performed exploiting a chiller plant emulator based on a co-simulation environment.

A Hierarchical Control Co-Design (HCCD) algorithm that optimizes system performance characteristics, with an emphasis on robustness to transient disturbances during real-time operation, is presented in [50]. The algorithm uses a Model Fidelity-Based Decomposition (MFBD) framework to address coupling issues between subproblems in highly coupled systems. The algorithm is applied to a thermal management system of an aircraft, and its performance is benchmarked against an all-at-once (AAO) system-level nested CCD approach. The findings indicate that the MFBD HCCD algorithm achieves solutions comparable to the AAO CCD but in approximately half the time.

Risbeck et al. [46] employ physics-based balances to model the behavior of an air handling unit (AHU) system, and they utilize phenomenological models for the control system to estimate airflows and energy usage. This model is integrated with a dynamic building model, incorporating thermal dynamics of the spaces and a model for airborne disease transmission. Although they do not explicitly mention CCD, their goal is to conduct multi-objective optimization to balance infection risk and energy consumption. Their optimization framework aims to identify Pareto-optimal solutions by exploring

various design variables and operational parameters.

The authors in [47] discuss the energy performance comparison of a chiller plant using conventional staging and a co-design approach in the early design phase of hotel buildings. It presents a case study of a hotel in Cuba and applies a genetic algorithm (GA) to optimize the chiller plant operation. The research considers different occupancy levels and cooling profiles, and proposes six chiller plant configurations. The outcomes reveal that the co-design approach significantly improves the chiller plant operation, positively impacting energy efficiency. Additionally, the study points out potential areas for future exploration, including expanding the energy analysis to secondary circuits and investigating alternative operational strategies to achieve further energy savings.

This chapter begins by addressing issues regarding the definition of the CCD optimization problem, specifically focusing on the coupling between the design and control optimization stages in Section 4.1. The overall design objective is detailed in Section 3.3, wherein the separate definition of the design and control objective functions is discussed. Subsequently, Section 3.4 provides an overview of the results obtained from a Global Sensitivity Analysis (GSA), outlining the significance of the design variables and offering additional insights into the coupling between design and control subproblems. Following this, Section 3.5 introduces and elaborates on the most prevalent strategies employed to solve CCD problems. Finally, Section 3.6 delves into the description of the black-box optimization method, placing particular emphasis on the Bayesian optimization approach.

3.2 Optimization Problem

Control Co-Design involves optimizing both the physical design parameters and control strategies of the system concurrently, aiming to find the most effective configuration and control policies that align with predefined objectives, while considering system dynamics and constraints.

The overarching optimization problem seeks the optimal solution of the

objective function $J(\xi)$ within the multidimensional space $\Xi \subset \mathbb{R}^D$, where ξ represents the overall design vector. Formally, the optimization problem can be formulated as follows:

$$\min_{\xi \in \Xi} \; J(\xi) \tag{3.1}$$

$$\text{subject to: } g(\xi) \leq 0 \tag{3.2}$$

$$h(\xi) = 0 \tag{3.3}$$

$$\underline{\xi} \leq \xi \leq \overline{\xi} \tag{3.4}$$

$$\text{with: } \xi \; = \; [\xi_{\mathcal{P}}, \xi_{\mathcal{C}}] \in \Xi \tag{3.5}$$

$$\Xi \subset \mathbb{R}^D \tag{3.6}$$

$$J : \Xi \to \mathbb{R}, \tag{3.7}$$

where $g(\xi)$ and $h(\xi)$ denote inequality and equality constraints, respectively, while $\underline{\xi}$ and $\overline{\xi}$ define the boundaries of the overall design vector space.

In complex systems, formulating such problem can be exceptionally challenging due to the inherent difficulties in analyzing the system as a whole and defining overall optimization objectives, especially when dealing with multiple, and at times conflicting, goals. An effective and commonly used strategy to tackle these complexities involves decomposing the problem into distinct subproblems, which often requires breaking down the system into subsystems, thus facilitating the implementation of discipline-specific analysis and optimization methods. Numerous works delve into diverse methodologies designed to decompose complex problems, such as penalty methods (e.g., Analytical target cascading [108]), model fidelity-based methods [50], decomposition based on Control Proxy Functions [38, 105], and others [109, 110, 96].

The overall optimization problem can be viewed as a composition of design and control optimization problems. As such, the objective function J usually consists of two distinct elements: one related to the plant design, denoted as $J_{\mathcal{P}}$, and the other associated with the optimization of the control system, denoted as $J_{\mathcal{C}}$. In the most comprehensive problem formulation, all

objective functions and constraints within these subproblems may depend on both plant design variables $\xi_{\mathcal{P}}$ and control variables $\xi_{\mathcal{C}}$ at the same time. Hence, the overall optimization problem can be rewritten as follow:

$$\min_{\xi_{\mathcal{P}},\xi_{\mathcal{C}}} \; J(J_{\mathcal{P}}(\xi_{\mathcal{P}},\xi_{\mathcal{C}}), J_{\mathcal{C}}(\xi_{\mathcal{P}},\xi_{\mathcal{C}})) \tag{3.8}$$

$$\text{subject to: } g_{\mathcal{P}}(\xi_{\mathcal{P}},\xi_{\mathcal{C}}) \leq 0 \tag{3.9}$$

$$g_{\mathcal{C}}(\xi_{\mathcal{P}},\xi_{\mathcal{C}}) \leq 0 \tag{3.10}$$

$$h_{\mathcal{P}}(\xi_{\mathcal{P}},\xi_{\mathcal{C}}) = 0 \tag{3.11}$$

$$h_{\mathcal{C}}(\xi_{\mathcal{P}},\xi_{\mathcal{C}}) = 0 \tag{3.12}$$

$$\underline{\xi}_{\mathcal{P}} \leq \xi_{\mathcal{P}} \leq \overline{\xi}_{\mathcal{P}} \tag{3.13}$$

$$\underline{\xi}_{\mathcal{C}} \leq \xi_{\mathcal{C}} \leq \overline{\xi}_{\mathcal{C}}. \tag{3.14}$$

In this scenario, an inter-dependency arises between the design and control optimization problems, often termed as coupling. Bi-directional coupling characterizes the problem when both design and control optimization problems depend on $\xi_{\mathcal{P}}$ and $\xi_{\mathcal{C}}$, and the variables influencing both optimization problems are termed coupling variables. However, in certain instances, the objective function and constraints of one subproblem may not rely on the decision variables of the other, resulting in uni-directional coupling. On the other hand, when the objective function and constraints of the artifact solely depend on design variables, and those of the controller exclusively on control variables, the problem lacks any coupling and is formally termed as uncoupled. Finally, it must be noted if coupling exists, then the solution of the overall optimization problem is not a single point, but a Pareto front [38, 104, 96].

As will be described in Section 3.5, in situations where the design and control optimization problems show weak coupling, the two subproblems may be addressed separately. However, when coupling is substantial, attempting to solve these problems separately lead to solutions that deviate significantly from the optimal ones [111]. Therefore, accurately measuring the coupling is crucial to discern its nature and determine the best strategy for solving the

CCD problem. Since the number of coupling variables is not an adequate metric to assess the strength of coupling, several studies can be found in the literature that focuses on developing methods to measure it, exploiting sensitivity quantities [111, 112, 113, 109, 114, 104, 106].

Although no direct measure of the coupling will be derived in this work, some preliminary insights about the existing coupling between the considered design and optimization problems will be drawn from the results of the Global Sensitivity Analysis (GSA) presented in Section 3.4. As will be seen, performing GSA with the Morris screening method can also shed light on the mutual impact of design and control variables on the optimization subproblems.

In the following section, the overall design objective is determined by separately defining the design and control objective functions.

3.3 Objective Functions

The choice of the objective functions must mirror the true intent of the designer in order to ensure successful design optimization [96]. Due to the complex nature of HVAC&R applications, it is common practice to define plant design and control objectives separately. Yet, this does not guarantee that the CCD problem is multiobjective [36]. Indeed, if no coupling exists between the subproblems, solving the overall optimization problem may lead to the same result as optimizing the subproblems individually. In this sense, taking advantage from the inherent holistic perspective of CCD would require to abandon traditional design paradigms and embrace an integrated system design approach. Following this would mean, for example, to move from plant design objective functions that overlook dynamics or the impact of control system action to objective functions encompassing metrics related to such aspects. In the HVAC&R sector, this shift in paradigm is still an ongoing challenge.

Nevertheless, a significant rationale behind separating these problems lies in the simplicity of formulating each individually. This approach facilitates

the implementation of a wide range of highly efficient computational methods, specifically designed for solving them in isolation. Furthermore, the separation of design and control objectives provides a reference point compared to the common practice, where designing a chiller system and its control system often occurs in separate and sequential stages. Therefore, breaking down the optimization problem into two subproblems aligns with one of the aims of this dissertation, which is to assess the advantages offered by implementing co-design methods in the HVAC&R domain by comparing the results obtained with a traditional design strategy against those achieved using a simultaneous approach. However, some precautions will be taken to incorporate holistic considerations during the definition of the optimization problems, as will be described in Section 4.1.

Before proceeding to illustrate the two objective functions, it is imperative, for the sake of understanding the subsequent motivations, to clearly define the overall objective of the CCD problem. Generally, a CCD problem in the HVAC&R domanin may have multiple competing objectives, such as initial capital investment, maintenance and operating costs, energy consumption, peak load, control system performance, etc. In the following subsections, the focus will be on elucidating the significance of the gas-cooler design, its synergy with the control system, and their joint influence on the energy consumption of the chiller plant. Given the natural correlation between the design variables (primarily geometric parameters) and the overall dimensions of the components, the design objective function will primarily target the overall dimensions of the gas-cooler. Similarly, considering the established connection in these types of systems between control variables and energy performance, the control objective function will encompass the total power consumption of the system. In summary, the objective of the CCD problem is to maximize the energy efficiency of the chiller system while minimizing the overall dimensions of the gas-cooler.

3.3.1 Design objective function

The pivotal role of the gas-cooler in influencing the performance of CO_2 refrigeration systems is supported by numerous studies [31, 115, 116, 117]. Authors unanimously agree on its significant impact on the gas-cooler/condenser pressure and overall power consumption, highlighting the critical importance of its optimal design. Moreover, they emphasize that achieving the optimal gas-cooler design poses a non-trivial challenge, primarily due to large variations in the thermophysical properties of the refrigerant and the diverse operating conditions characterizing the annual operation of the refrigerating systems. The presence of strong nonlinearities in underlying physics, coupled with complex interactions among chiller components, significantly amplifies the design complexities. As a result, achieving an optimal gas-cooler configuration demands meticulous consideration of these multifaceted factors, making it a demanding yet crucial aspect in enhancing the efficiency and functionality of CO_2 refrigeration systems.

The aforementioned aspects serve as motivation to focus optimization efforts on the gas-cooler. This is also supported by the existence of a dynamic model capable of capturing the dynamics and interactions with the other components and the control system, thus enabling comprehensive system-level considerations. For this reason, the design objective function is represented by the overall volume of the gas-cooler, as defined in Eqs. 3.15-3.16:

$$J_{\mathcal{P}}(\xi_{\mathcal{P}}) \;=\; V_{GC,overall} \tag{3.15}$$

$$\text{with } V_{GC,overall} \;=\; l_{GC}\, h_{GC}\, \left(w_{GC} + \Delta w_{GC}\right), \tag{3.16}$$

where Δw_{GC} is the width of the duct transition, which is considered as a function of gas-cooler height h_{GC} and fan impeller diameter d_{fan} (see Figure 3.1), as per Eq. 3.17:

$$\Delta w_{GC} = \Delta w_{GC,0}\, \frac{h_{GC} - d_{fan}}{h_{GC,0} - d_{fan,0}}, \tag{3.17}$$

with $\Delta w_{GC,0}$, $h_{GC,0}$, and $d_{fan,0}$, equal to the corresponding nominal design values (i.e., 100 mm, 1240 mm, and 905 mm, respectively).

In turn, gas-cooler height h_{GC} and width w_{GC} are calculated as follows:

$$h_{GC} = p_{t,GC}\, N_{t,R,GC} \tag{3.18}$$

$$w_{GC} = p_{R,GC}\, N_{R,GC}, \tag{3.19}$$

based on the tube pitch $p_{t,GC}$, row pitch $p_{R,GC}$, number of tubes for each row $N_{t,R,GC}$, and number of rows $N_{R,GC}$ of the gas-cooler.

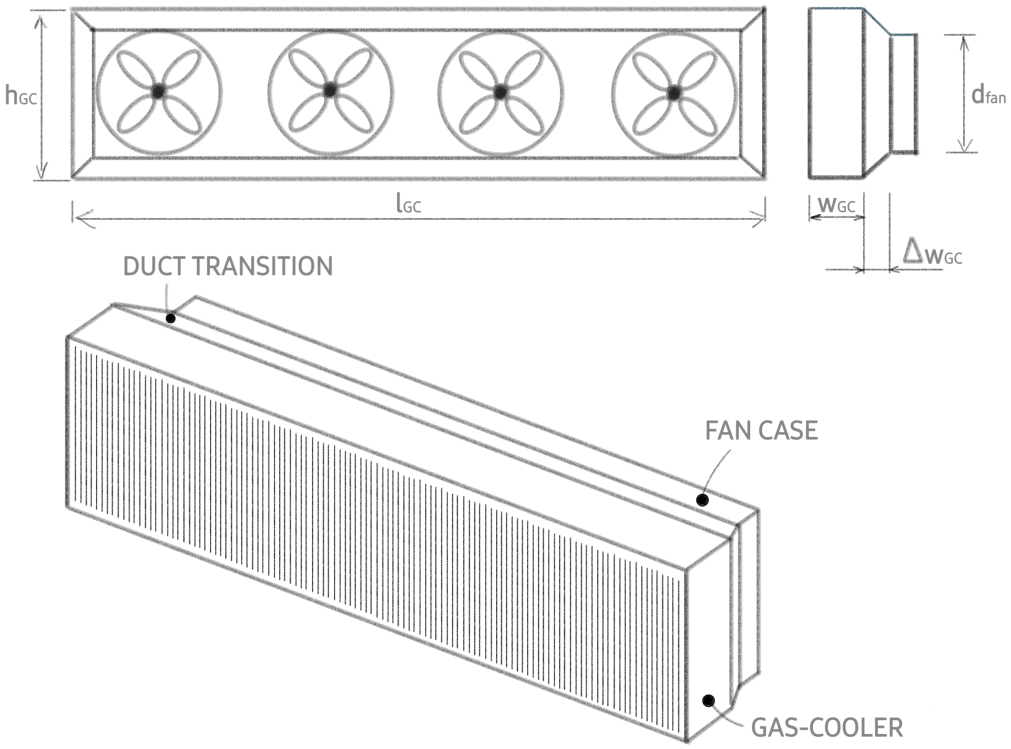

Figure 3.1: Gas-cooler sketch.

As can be seen, the design objective function depends only on geometric parameters. The tube pitch $p_{t,GC}$, row pitch $p_{R,GC}$, and fan impeller diameter d_{fan} will be regarded as design variables due to their direct impact on the objective function. Although the internal diameter of the tubes $d_{i,GC}$ and the fin pitch $p_{f,GC}$ do not affect the objective function directly, they modify the cross-sectional area, the heat transfer surface area and the hydraulic diameter of both the first fluid and second fluid sides, as described in subsection 2.5.2,

thereby influencing the heat exchange and pressure losses in the gas-cooler. For this reason, they will also be incorporated into the design variables vector due to their potential impact on performance. All other geometric parameters will remain fixed at their nominal values. Section 3.4 will elaborate on the use of GSA to reduce the number of design variables based on their importance in optimization.

3.3.2 Control objective function

Designing the control objective function typically involves integrating elements concerning the performance of the overall system, encompassing energy consumption, as well as performance metrics of the control system such as response speed, accuracy, and control effort [118]. However, this work specifically concentrates solely on the steady-state performance of the overall system, as will be detailed in Chapter 4.

Considering the combined static-feedfoward and feedback control architecture depicted in Section 2.6, optimizing the performance of the chiller system primarily involves decisions about the static-feedfoward for the rotational speed of the fans (n_{fan}) and the opening of the back-pressure valve (o_{BPV}). Given that the optimization focus is solely on the steady-state energy efficiency of the plant-controller system, only the feedforward variables n_{fan} and o_{BPV} are considered as control parameters.

The control objective function is determined by the total power consumption P_{tot} of the system, which comprises the combined power consumption of the compressor P_{comp} and the four gas-cooler fans P_{fans}. This function depends on the operating conditions and both the design and control variables.

On one hand, the interaction between gas-cooler design, fan impeller diameter, and fan rotational speed influences the power consumption of the fans by altering air flow rates and pressure drops within the gas-cooler [119]. On the other hand, this interaction also affects heat exchange within the gas-cooler, consequently impacting its internal pressure levels.

Moreover, this interaction overlaps with the interaction between the valve opening and the compressor's rotational speed regulated by its decentralized

controller. This adjustment modifies pressure levels, subsequently influencing the power consumption of the compressor.

The control objective function is represented as follows:

$$J_{\mathcal{C}}(\xi_{\mathcal{P}}, \xi_{\mathcal{C}}) = P_{tot} \tag{3.20}$$

$$\text{with } P_{tot} = P_{comp} + P_{fans}, \tag{3.21}$$

3.4 Decision Variables Selection through Global Sensitivity Analysis

Sensitivity Analysis (SA) methods serve as indispensable tools employed to explore how the uncertainty in a model's output can be attributed to various sources of uncertainty within the inputs of the model [120, 121]. These methods help in understanding and quantifying the impact of different input variables or parameters on the output of a model, elucidating which factors contribute most significantly to the overall uncertainty in the predictions of the model [122].

SA methods can be categorized into local and global approaches, distinguished by the range of variation applied to the inputs. Local Sensitivity Analysis focuses on assessing the effects of small input alterations on the output of the model. These slight perturbations typically center around nominal values. This deterministic method involves computing or estimating the partial derivatives of the model output at a specific point. It is worth noting that conventional local sensitivity methods, based on linear assumptions, may have limitations when applied to nonlinear systems.

Compared to local analysis, the Global Sensitivity Analysis (GSA) methods encompass the complete range of parameters under scrutiny. They thoroughly explore both input and output spaces, eliminating limitations tied to localized points or individual input parameters. This approach allows for a more comprehensive assessment of how inputs influence outputs and offer several benefits, including the identification and prioritization of the most influential inputs. They also identify non-influential inputs, making it possi-

ble to set them to nominal values. Furthermore, these methods map output behavior as a function of inputs, with a particular focus on specific input domains if necessary. Additionally, they enable the calibration of certain model inputs using available information [121, 122].

As pointed out in [120], a reliable global sensitivity measure should provide multidimensional averaging, that is to assess the impact of a factor when all the others are simultaneously varying, while exploiting the whole domain of each input. Also, it is essential for a GSA method to be model-independent, ensuring its applicability regardless of whether the model is additive or linear. Moreover, it is crucial for a global sensitivity measure to effectively account for interaction effects. These are particularly notable in nonlinear and non-additive models, where the combined effect of altering two factors deviates from the sum of their individual impacts. However, it must be noted that applying these methods to nonlinear systems can pose challenges due to the necessity to evaluate the entire input range [123].

In this study, a GSA using the Elementary Effects (EE) method, also known as Morris method [124], is performed to rank the influence of both design and control variables on the objective functions outlined in Section 3.3. This method is particularly advantageous for its computational efficiency, making it well-suited for scenarios involving a large number of input variables and/or computationally intensive numerical models.

Following a similar workflow to the one presented in [125], the results of this analysis are used to narrow down the attention to the most influential variables affecting both the plant and the control system. This facilitates a reduction in the number of variables under consideration for the optimization. Additionally, the EE method enables exploration of the nonlinear influence of each variable on the objective functions and the strength of the mutual interaction among these variables. Thus, it provides valuable insights into potential couplings between design and control optimization subproblems.

3.4.1 Global Sensitivity Analysis and Morris Method

The Elementary Effects (EE) method stands as a simple yet powerful screening technique, rooted in the concept of elementary effects proposed by Morris in [124]. It falls within the category of "One At a Time" (OAT) designs, where each input is varied while fixing the others, and sticks to the concept of local variation around a base point. Nevertheless, this method attempts to overcome the limitations of the derivative-based approach by broadening the ranges of input variations and multiple local measures, thus eliminating dependence on a single sample point [121].

The EE method primarily aims to compute two sensitivity measures used to categorize inputs into three groups: inputs having negligible effects, inputs having prominent linear effects without interactions, and inputs exhibiting substantial nonlinear effects and/or interactions with other factors.

The method involves discretizing the input space for each variable and executing a specified number, denoted as r, of One At a Time (OAT) designs. In this study, these designs are randomly selected within the input space using the sampling strategy proposed by Campolongo et al. in [126]. This technique employs Sobol' quasi-random sequences to construct a radial OAT design.

Radial samplings operate by altering one factor at a time from a starting random point within the input factor space. For a given starting point $\overline{x}_0 = (a_1, a_2, \ldots, a_k)$, k random points $\overline{x}_i = (a_1, a_2, \ldots, b_i, \ldots, a_k)$ are generated by modifying only one input variable at each step. For each of these random points, the elementary effect of the corresponding input is computed using the following equation:

$$EE_i = \frac{y(\overline{x}_i) - y(\overline{x}_0)}{\overline{x}_i - \overline{x}_0}, \tag{3.22}$$

where y is the model response.

This sampling is then repeated r times, yielding the same number of elementary effects for each input variable. Finally, once the EEs are defined, two sensitivity measures are computed for this method: the mean value μ^*

(as proposed in [127]) and the standard deviation σ. These are calculated as:

$$\mu_i^* = \frac{\sum_{j=1}^{r} |EE_{i,j}|}{r} \tag{3.23}$$

$$\sigma_i = \sqrt{\frac{1}{r}\sum_{j=1}^{r}\left(EE_{i,j} - \frac{\sum_{j=1}^{r} EE_{i,j}}{r}\right)}. \tag{3.24}$$

Here, $EE_{i,j}$ represents the elementary effect of the i^{th} variable obtained in the j^{th} repetition. The μ_i^* value quantifies the influence of the i^{th} input on the output; higher μ_i^* values indicate more significant effects on the model response under consideration. Conversely, the standard deviation σ_i measures the nonlinearity of the i^{th} input effect on the output and/or the interaction strength with other inputs. Thus, a variable exhibiting a high σ_i is deemed to have nonlinear effects and/or involvement in interactions with at least one other variable [121, 126, 122].

The total number of model evaluations N is given by:

$$N = r\,(k+1). \tag{3.25}$$

3.4.2 Decision Variables Selection

In the present work, the SAFE toolbox, presented in [128, 129], is used as a tool to perform GSA on the design, control, and overall objective functions. This toolbox ensures a trade-off between quality of GSA implementation and user accessibility. Moreover, its conception aims to democratize GSA, thus allowing non-specialist users to effortlessly implement workflows that exploit its features for sampling, sensitivity index calculation, and visualization [130].

The general idea is to identify and rank the most influential subset of design and control variables for subsequent optimization stages. To do so, three different GSAs are carried out, each corresponding to a distinct objective function, maintaining the same set of input variables while changing the set of investigated output. Furthermore, an analysis of the GSA outcomes could offer valuable insights into potential couplings between the two

subproblems.

The number of the considered elementary effects r is fixed 30, and the number of inputs k corresponds to the size of the starting vector of overall design variables. This vector is formed by combining the initial design and control variables, outlined in subsections 3.3.1 and 3.3.2. The former encompasses parameters such as the internal diameter of gas-cooler tubes $d_{i,GC}$, gas-cooler fin pitch $p_{f,GC}$, gas-cooler row pitch $p_{R,GC}$, gas-cooler tube pitch $p_{t,GC}$, and fan impeller diameter d_{fan}. The latter involves the feedforward input variables within the chiller system, coupled with the multiple feedback loops, as detailed in Section 2.6. Corresponding nominal values are available in Table 3.1 and Table 3.2, respectively.

Table 3.1: Nominal values of the starting design variables.

$d_{i,GC,0}$	5.94 mm
$p_{f,GC,0}$	2.1 mm
$p_{R,GC,0}$	23.4 mm
$p_{t,GC,0}$	23.4 mm
$d_{fan,0}$	905 mm

Table 3.2: Nominal values of the control variables for the system operating in a fully open-loop configuration.

$n_{C,0}$	1450 rpm
$n_{fan,0}$	530 rpm
$o_{BPV,0}$	0.1

Hence, k is equal to 7, resulting in eight points for each radial sampling and a total of 240 evaluations, computed as in Eq. 3.25. The investigated input variables and their assigned domain are summarized in Table 3.3.

The parallel coordinate plot depicted in Figure 3.2 serves as a means to visualize simulations presented as a set of trajectories [122]. This representation aims to illustrate the radial sampling of the input space and assess whether the reduced number of elementary effects impacts the sensitivity analysis by potentially omitting thorough exploration. Complete coverage of

Table 3.3: Lower and upper bounds of the starting vector of overall design variables.

	$\underline{\xi_0}$	$\overline{\xi_0}$
$d_{i,GC}$	5 mm	6.8 mm
$p_{f,GC}$	1.78 mm	2.42 mm
$p_{R,GC}$	19.9 mm	26.9 mm
$p_{t,GC}$	19.9 mm	26.9 mm
d_{fan}	769 mm	1041 mm
n_{fan}	318 rpm	636 rpm
o_{BPV}	0.045	0.125

the input space is indicated by the trajectory lines intersecting each input (represented as vertical lines) along their entire length.

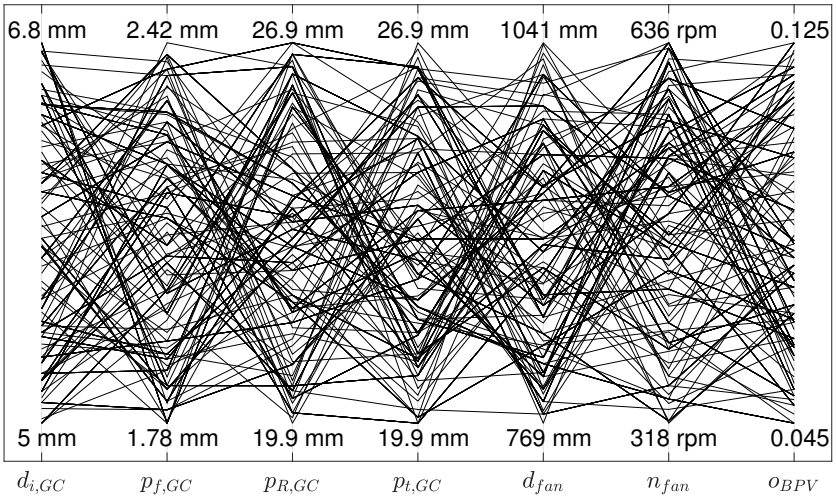

Figure 3.2: Parallel coordinate plot.

The results of the GSA are shown in Figure 3.3 and summarized in Table 3.4. They refer to the case with external air temperature T_{air} and thermal cooling load $\dot{Q}_{load}$ equal to 30.4 °C and 21.3 kW, respectively. Here, the same notation considered in Table 4.1 for the boundary conditions is used. Therefore, $T_{air} = 30.4\,°C$ corresponds to the condition HT, while $\dot{Q}_{load} = 21.3\,kW$ is referred to as LTL.

Table 3.4: Mean (μ^*) and standard deviation (σ) of elementary effects for the objective functions, for HT-LTL (refer to Table 4.1) with T_B^* equal to 5.5 °C.

	Design objective function		**Control objective function**		**Overall objective function**	
	μ^*	σ	μ^*	σ	μ^*	σ
$d_{i,GC}$	0	0	0.03	0.02	0.02	0.01
$p_{f,GC}$	0	0	0.11	0.04	0.06	0.03
$p_{R,GC}$	0.48	0.04	0.10	0.04	0.13	0.03
$p_{t,GC}$	2.12	0.18	0.20	0.06	0.72	0.10
d_{fan}	0.92	0.08	2.07	1.32	0.96	0.71
n_{fan}	0	0	1.80	1.10	1.07	0.64
o_{BPV}	0	0	7.71	0.83	4.63	0.50

The initial analysis investigates the most significant input variables with respect to the design objective function. Notably, the gas-cooler tube pitch $p_{t,GC}$ emerges as the most influential variable, succeeded by the fan impeller diameter d_{fan} and the gas-cooler row pitch $p_{R,GC}$, in that order. These three variables exhibit linear effects without any discernible interactions, indicated by their considerably low standard deviation values. Conversely, the remaining variables demonstrate a negligible impact on the design objective function, registering zero effect.

In the second case, the influence of the back-pressure valve opening o_{BPV} on the control objective function (i.e., total power consumption of the system, as per Eq. 3.20) is remarkably dominant and predominantly linear. It is followed by the fan impeller diameter d_{fan} and rotational speed n_{fan}, which exhibit nearly equivalent effects, while the remaining variables have negligible contributions. It is interesting to note how d_{fan} and n_{fan} exhibit a similar standard deviation value, comparable to the mean value, thus suggesting potential nonlinear effects and/or interactions among the variables. This observation, along with purely physical considerations, hints at a potential coupling between these variables resulting in a uni-directional coupling between the variable d_{fan} and the control objective function. Indeed, this

aligns with the understanding that the performance of the fans is not only affected by the rotational speed but also by their size.

Finally, the GSA is performed on the overall objective function J calculated using the weighted-sum method, as will be explained in subsection 4.1.2, through the following equation:

$$J(\xi_{\mathcal{P}}, \xi_{\mathcal{C}}) \;=\; \theta\, J_{\mathcal{P}}(\xi_{\mathcal{P}}) + (1-\theta)\, J_{\mathcal{C}}(\xi_{\mathcal{P}}, \xi_{\mathcal{C}}). \tag{3.26}$$

The results outlined in Table 3.4 and Figure 3.3c refers to the case with the weight θ fixed at 0.4. The analysis reaffirms the prominence of the valve opening o_{BPV} as the most influential variable, succeeded by rotational speed n_{fan}, fan impeller diameter d_{fan}, and gas-cooler tube pitch $p_{t,GC}$, in descending order of impact. The remaining variables exhibit negligible effects on the objective function. As expected, d_{fan} and n_{fan} demonstrate potential nonlinear effects or mutual interactions, aligning with the earlier discussion.

Thanks to these results, it is possible to reduce the number of overall design variables.

The valve opening o_{BPV}, along with impeller diameter d_{fan} and rotational speed n_{fan} of the fans, cannot be neglected due to their relevant effect on the objective functions, while the gas-cooler internal tube diameter $d_{i,GC}$ has a negligible impact in all considered scenarios.

Furthermore, it is plausible to consider the tube pitch $p_{t,GC}$ and row pitch $p_{R,GC}$ as a combined parameter $p_{R/t,GC}$. This approach also aligns with common industrial practices in finned-tube heat exchanger design, often employing equal values for these parameters. This method preserves information about the impact of the row pitch while minimizing the count of individual variables.

Lastly, the gas-cooler fin pitch $p_{f,GC}$ has no effect on the design objective function and very little effect on both control and overall objective functions. However, it must be included as it plays a role in one of the inequality constraints considered in the design optimization problem (see subsection 4.1.1).

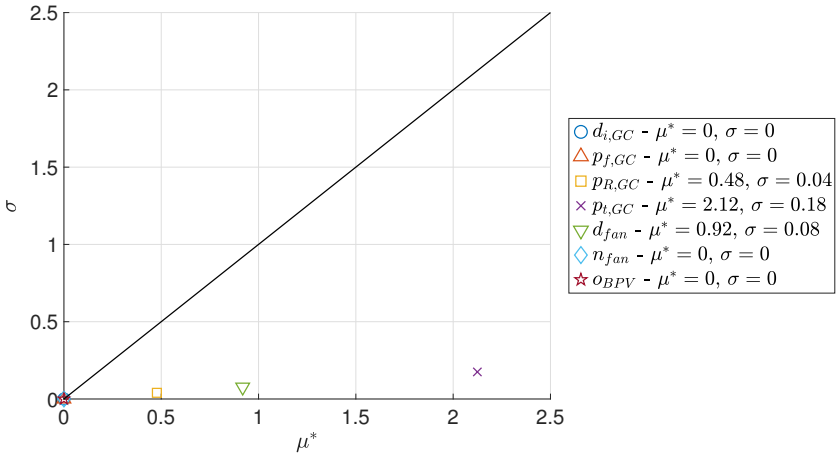

(a) Design objective function

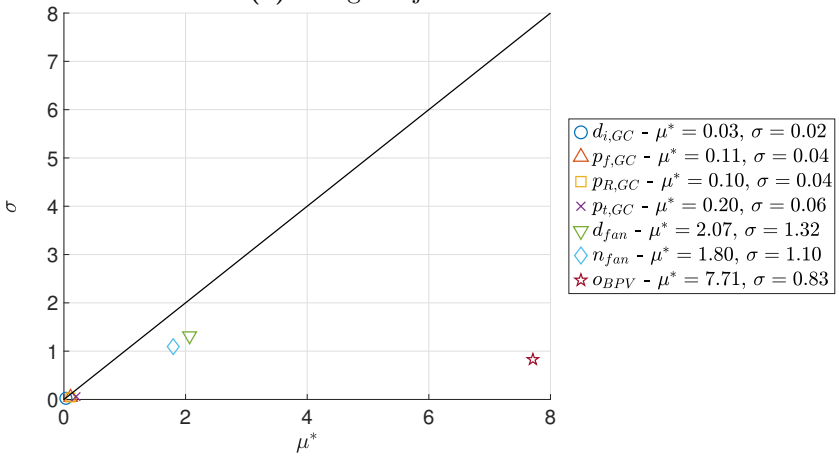

(b) Control objective function

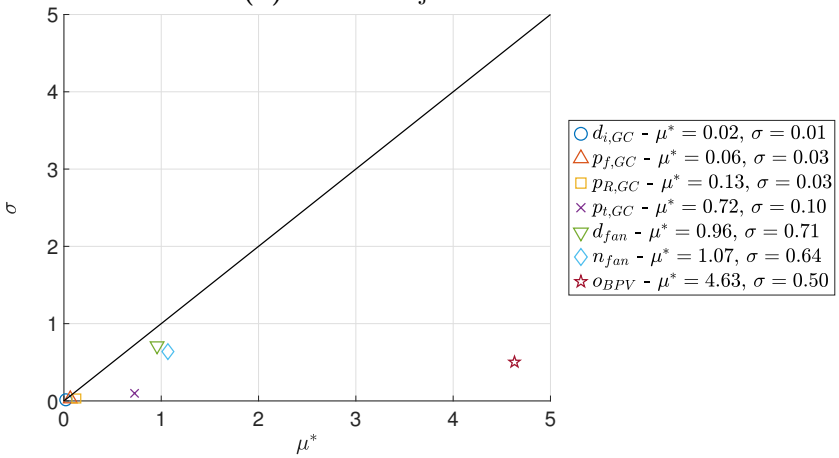

(c) Overall objective function calculated using the weighted-sum method employing $\theta = 0.4$

Figure 3.3: Mean (μ^*) and standard deviation (σ) of elementary effects for the objective functions, for HT-LTL (refer to Table 4.1) with T_B^* equal to 5.5 °C.

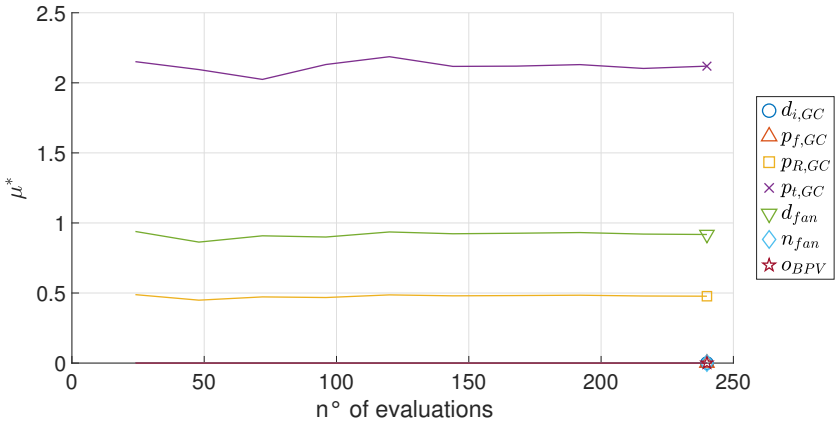

(a) Design objective function

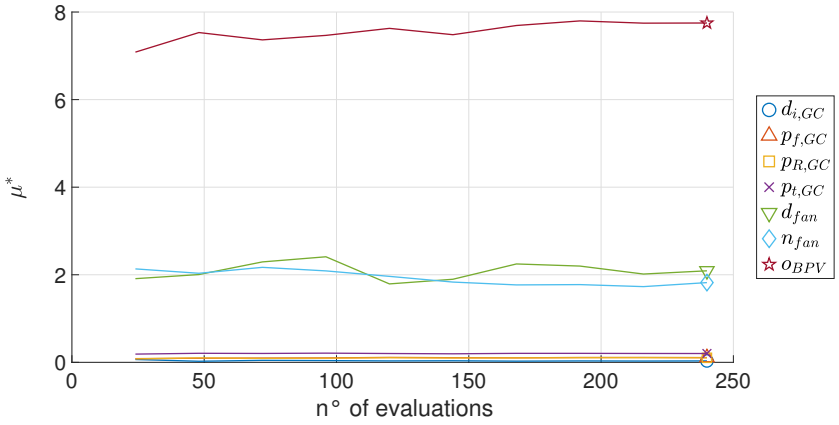

(b) Control objective function

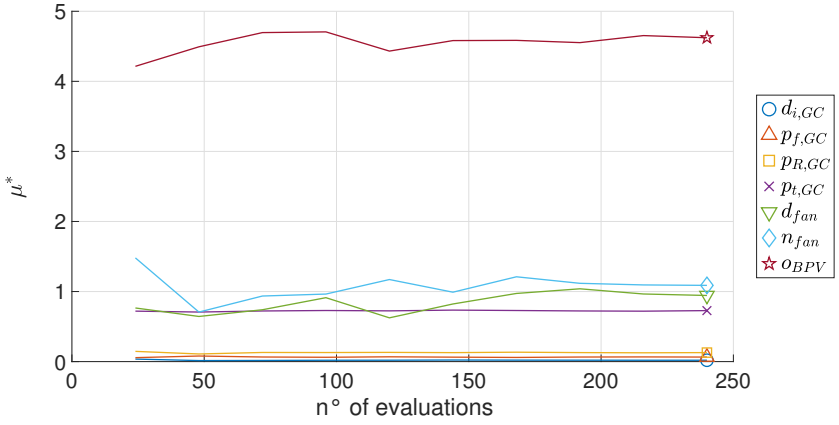

(c) Overall objective function calculated using the weighted-sum method employing $\theta = 0.4$

Figure 3.4: Convergence plots.

Therefore, the vector ξ of the combined design and control variables, to be used in the optimization problems outlined Chapter 4, is structured as follows:

$$\xi = \left\{ p_{f,GC},\, p_{R/t,GC},\, d_{fan},\, n_{fan},\, o_{BPV} \right\}. \tag{3.27}$$

In Figure 3.4, the convergence plots display the mean value of each input as a function of the number of model evaluations, for all the considered objective functions. As the sample size increases, the fluctuation in the mean values converges toward their actual values, indicating the correct selection of the number of elementary effects, r, and a uniform exploration of the input space through the radial sampling strategy.

3.5 Optimization Strategies

In the realm of CCD, the interconnected relationship between design and control optimization creates a need for a spectrum of optimization strategies that effectively balance the complexities between system design and control mechanisms. The present study will adopt the classification outlined in [38, 131] and illustrated in Figure 3.5. These strategies encompass a variety of methodologies, spanning from conventional sequential and iterative approaches to the computationally more intensive simultaneous strategy and the complex nested optimization schemes. Additionally, partitioned optimization strategies adopt a methodical approach by addressing subsystems individually, refining each component before integrating them into a unified, comprehensive solution. This varied landscape of optimization strategies reflects the intricate relationship between system architecture and its governing controls, addressing the essential synergy required for achieving optimal performance in Control Co-Design scenarios.

The choice of the most suitable optimization strategy is application dependent, as it heavily relies on the nature and strength of the couplings established between the system and its control system. Also, in cases where the coupling is non-negligible, there emerges the possibility of dividing optimization strategies into two distinct categories. The first category encompasses

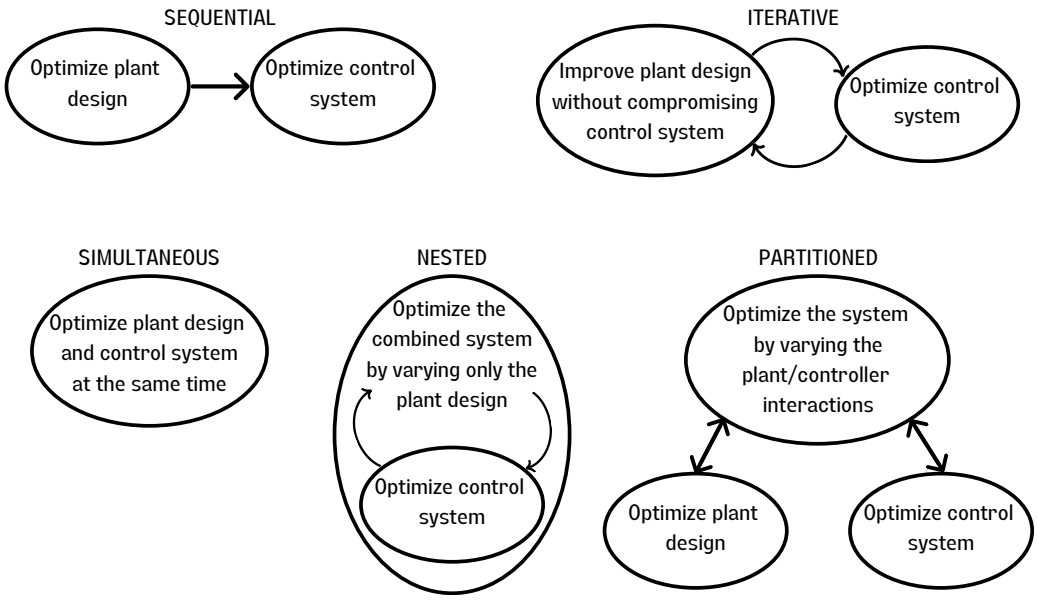

Figure 3.5: Optimization strategies classification (after [38]).

the sequential and iterative methods, which are relatively simpler to implement and faster in reaching solutions [111]. However, they do not assure convergence towards either a feasible or an optimal solution. Conversely, the second category comprises the simultaneous, nested, and partitioned methods. While these approaches guarantee optimality, they are more intricate to implement owing to the complexity of the optimization problems and the existence of non-convex coupling constraints. Additionally, their computational demands increase significantly due to the size of the problem.

3.5.1 Sequential Optimization

The sequential approach is the conventional and typically the most practical method for solving CCD problems. This preference is closely tied to industry practices, where the complex nature of engineering systems and the size of professional teams often make coordinating a simultaneous design across all groups impractical, thus leading to the perception that the sequential approach is the primary and sometimes the only viable option [96, 28].

This method usually starts by optimizing the system design and then moves on to optimize the control system, considering the optimized design variables as parameters in the control optimization process. In instances of uni-directional coupling, the controller architecture is entirely disregarded in the design optimization, resulting in an optimal solution only for the plant. Yet, in situations involving bi-directional coupling, the control variables are fixed to predefined values and considered as parameters in the design optimization, potentially leading to a solution that might not be optimal for both subproblems.

Numerous studies in the literature propose modified sequential approaches to address these limitations, aiming to preserve the advantages of the method, such as simplicity and low computational load.

Among these methods, one uses the notion of system controllability in open-loop, independent of controller design, in conjunction with the Gramian matrix [132, 112, 133, 105]. The authors have demonstrated how the general formulation of the control problem does not allow a priori determination of the existence and intensity of coupling. However, they have highlighted a relationship between the Gramian matrix and the coupling, enabling the a priori computation of coupling for a significant set of crucial control design problems. Then, the relationship between controllability and coupling can be exploited to formulate Control Proxy Functions (CPFs), which can be used to modify the sequential method. By incorporating the CPF into the design objective function and solving the resulting open-loop design optimization problem, a system configuration is obtained. This configuration can be utilized in the control optimization problem, resulting in an optimal or near-optimal solutions.

Another approach involves the incorporation of control objectives, often in the form of constraints, within the system design phase. This is achieved by leveraging the eigenvalues of the Gramian controllability matrix to define the control objective function. By employing a sequential approach in this manner, it ensures the attainment of a system design with enhanced controllability [99].

3.5.2 Iterative Optimization

The iterative optimization involves an incremental refinement process, continuously adjusting both system design and control strategies. The solution obtained from optimizing the system design is used in the optimization of the control system, and vice versa. This reciprocal exchange ensures that each optimization step considers the insights gained from the other, aiming for an improved overall solution. Despite being advantageous in maintaining the separation of the two subproblems, in the presence of coupling this approach might not guarantee an optimal solution.

Nonetheless, some studies suggest that this strategy can be proficiently modified to identify optimal solutions for CCD problems of linear control systems [134, 135].

3.5.3 Simultaneous Optimization

This optimization strategy aims to tackle the CCD optimization problem presented in Eqs.3.8-3.14. By merging design and control objectives within a unified framework, it combines constraints and variables from individual subproblems. Yet, this integration can lead to non-convexity, even when individual objectives are convex [111], and results in a larger optimization problem, thereby increasing computational demands. Additionally, the common practice of linearly combining objective functions may be limited in identifying points on a non-convex Pareto frontier.

The simultaneous approach ensures system optimality upon finding a solution. However, it does come with some challenges. Notably, the need to formulate and combine two distinct objectives from different disciplines presents a significant obstacle. Additionally, committing to a controller architecture early in the process, before finalizing the plant design, can be a demanding aspect of this method. Moreover, adopting this approach means forgoing the use of specialized optimization algorithms developed to solve specific subproblems, potentially limiting the efficiency of the optimization process [37].

3.5.4 Nested Optimization

Also referred to as bi-level optimization, this optimization strategy involves two nested optimization loops. In the outer loop, the combined system (plant and control architecture) is optimized, only focusing on the plant design variables. The resulting optimized design is then fed into the inner loop to seek the optimal solution for the control system. The process is then iterated using these optimal values as starting points. However, it guarantees optimality only for uni-directional coupling scenarios [38].

An advantageous aspect of nested optimization is its capacity to leverage established optimal control algorithms to efficiently solve the inner-loop problem [37].

3.5.5 Partitioned Optimization

Partitioned optimization strategies divides a complex problem into smaller, more manageable subproblems, and can be used to solve co-design problems with bi-directional coupling, while ensuring optimality. Each subproblem is solved independently but is coordinated to maintain consistency across the entire system. Therefore, design and control optimization subproblems are overseen by a master problem that manages their interactions, and optimization is achieved by coordinating the enhancement of both the artifact and the controller while considering their mutual influence.

3.6 Black-box Optimization and Bayesian Optimization

As described in Chapter 2, the CCD problem addressed in this dissertation relies on a physics-based model of a chiller system. These kind of models possess accurate predictive capabilities embedded within their mathematical structures. However, these qualities often come at the expense of increased nonlinearity and numerical stiffness, making these models challenging to simulate. Furthermore, obtaining closed-form solutions or analytical

representations becomes often impracticable due to these complexities.

In this context, black-box optimization methods are crucial in addressing challenges related to real-world engineering optimization problems. They become particularly essential when traditional methodologies fail due to the difficulty in obtaining analytical expressions for key parts of the optimization problem, such as the function J in Eqs. 3.1-3.7. Within the realm of black-box optimization methods, metaheuristics (e.g., Genetic Algorithm, Particle Swarms, Simulated Annealing, etc.) play a pivotal role due to their ability in efficiently exploring the search space with no or little information about it [136, 137, 138, 139, 140]. Each metaheuristic initializes with an initial set of values and iteratively generates new samples using a specified mechanism based on current samples and their corresponding objective function values. The fundamental differences between metaheuristics stem from the distinct mechanisms employed by each algorithm to generate new reliable samples. This iterative process involves a balance between exploration, emphasizing global search, and exploitation, which focuses on refining solutions locally.

The selection of the most appropriate method for a specific problem class is a critical aspect, subject to what are known as No Free Lunch Theorems (NFLT) [141]. These suggest that, without prior knowledge on the geometry of the objective function J (i.e., uniform distribution over the space of all the possible objective functions), there is no universally superior optimization method. In practice, the effectiveness of an optimization algorithm depends on how well it aligns with the structure of the problem [136, 139, 140, 141]. Therefore, the choice of the most appropriate optimization algorithm is problem-dependent. This is particularly evident in MDO problems that employ high-fidelity numerical models, where selecting the best algorithm is also tied to the computational cost of model evaluations, a factor that notably impacts the overall computational cost of the optimization [142].

A key aspect of NFLT is their evident connection with Bayesian analysis [136, 140, 141]. For an optimization problem such as the one defined in Eqs. 3.1-3.7, adopting a black-box optimization approach implies that information about the objective function is confined to a finite sample dataset

$\mathcal{D} = \left\{(\xi_1, \hat{J}(\xi_1)), (\xi_2, \hat{J}(\xi_2)), \cdots, (\xi_n, \hat{J}(\xi_n))\right\}$, where ξ_i are the evaluation points and $\hat{J}_i$ are the unknown function evaluations. Within the Bayesian framework [143, 144], solving the optimization problem becomes an inferential task, achieved by leveraging the dataset $\mathcal{D}$ alongside a prior distribution $P(J)$ defined over the function space (i.e., a probabilistic surrogate model that approximates the objective function J). By combining the likelihood $P(\mathcal{D}|J)$ with the prior $P(J)$, it is possible to obtain a posterior

$$P(J|\mathcal{D}) \propto P(\mathcal{D}|J)\, P(J), \tag{3.28}$$

that can be used to provide insights into the promising regions of the search space and iteratively refine the belief concerning the functional model. Assuming a prior in the Bayesian logic is equivalent to consider a nonuniform distribution over the space of possible objective functions from the NFLT point of view.

In this scenario, akin to the Bayesian approach, each metaheuristic inherently assumes a functional model, albeit more or less implicitly. Consequently, every method carries its own implicit prior, shaped by the encoded parameters and the employed search operators. The prior essentially dictates the approach of each algorithm in balancing between local search (exploitation) and global search (exploration). So, all metaheuristics rely on a model class similar to the Bayesian prior for the objective function. This model class is integrated with sampled points at each iteration to direct the search toward the most promising directions. Nevertheless, by naturally incorporating Bayesian principles, the Bayesian optimization (BO) method exhibits several advantages, especially in overcoming inherent limitations associated with solving CCD problems in the HVAC&R sector. However, it must not be forgotten that also Bayesian optimization is susceptible to the curse of dimensionality [136].

Bayesian optimization is a method used to globally optimize unknown objective functions, particularly advantageous when function evaluations are expensive or resource-intensive [145, 146]. The theoretical foundation of this

data-driven technique lies in Bayesian inference and it employs probabilistic models and a surrogate function to capture the uncertainty in the unknown function's behavior. By iteratively evaluating the objective function at carefully chosen points, Bayesian optimization updates its surrogate model and uses it to guide the search towards regions of the search space that are likely to contain the global optimum, effectively minimizing the number of costly evaluations required to identify the optimal solution. Its adaptability to handle expensive objective function observations makes Bayesian optimization highly suitable for scenarios where computational resources or evaluations are limited [147].

Again, the cornerstone of Bayesian optimization is given by the choice of the prior, pivotal in inferring insights about the geometry of the objective function from a sampled dataset during a training phase. As seen, this capability is crucial, especially in addressing black-box optimization problems, such as those encountered within the context of CCD. Additionally, BO demonstrates flexibility by allowing the exploration of different priors while maintaining a consistent optimization framework. This adaptability permits the testing of various prior assumptions without altering the underlying structure of the optimization process.

Bayesian optimization finds application across a wide spectrum of fields [148]. Within the HVAC&R sector, numerous studies demonstrate its efficacy in tackling various challenges, spanning from model calibration [149, 150] to control optimization [151, 152, 153, 154].

Control Co-Design community has witnessed a growing interest in BO, evident in its application across various domains [155, 100, 156, 101]. Nevertheless, its specific implementation for solving CCD problems in HVAC&R applications remains limited [45, 44]. However, despite this limitation, the range of studies showcasing the adaptability and efficacy of BO method in tackling multifaceted challenges within the HVAC&R realm is noteworthy. As such, BO emerges as a reliable tool with the potential to effectively address the specific CCD problem delineated in this dissertation.

In the following subsection, a brief overview of the Bayesian optimization

method adopted in this study will be presented.

3.6.1 Bayesian optimization method

Bayesian optimization method can be used to solve Control Co-Design optimization problems, by integrating them into black-box optimization frameworks. Within these frameworks, the optimization problem is treated as a black-box, allowing the implementation of Bayesian optimization techniques to efficiently explore and exploit the search space, iteratively improving the solution without requiring detailed knowledge of the internal structure of the problem.

The BO framework is characterized by two main elements. The first ingredient is a probabilistic surrogate model, acting as a prior, alongside an observation model defining the data generation process. This prior function encapsulates the belief about the space of possible objective functions. By combining the prior with evaluations $\hat{J}_i$ of the unknown objective function J, a posterior distribution is computed using Bayes' theorem, as outlined in Eq. 3.28. The posterior updates the belief about objective function and can be used to generate a predictive distribution for J at each optimization variable in ξ.

The second key element is the acquisition function, which interacts with the posterior to formulate a utility function. By maximizing the acquisition function, it is possible to determine the subsequent evaluation point. Thus, the acquisition function directs the search toward subsets of Ξ where the optimal solution is more likely to be located, effectively balancing exploration and exploitation within the search space [157].

Therefore, the choice of the prior is a crucial point and relies on assumptions made about the unknown objective function. For the CCD case considered in this work, J is presumed to belong to the category of smooth and well-behaved functions, making Gaussian Process (GP) an appropriate choice as a probabilistic surrogate model. GPs are flexible probabilistic

models that offer non-parametric modeling, capable of adapting to complex function shapes without assuming specific forms. Particularly advantageous in Bayesian optimization, GPs excel in handling noisy or computationally expensive functions, facilitating efficient exploration of the search space while ensuring a balance between exploration and exploitation. Their ability to quantify uncertainty enables informed decisions about where to sample next, making them particularly useful for optimizing black-box functions with limited evaluations.

This class of non-parametric models is defined by a mean function $\mu_0 : \Xi \to \mathbb{R}$ and a positive definite covariance function (kernel) $\kappa : \Xi \times \Xi \to \mathbb{R}$. Defined $\mathbf{J}$ and $\hat{\mathbf{J}}$ as the vectors of the unknown function values $J_i = J(\xi_i)$ and the noisy observations $\hat{J}_i$ of J on a finite set of n evaluation points ξ_i, GP considers that both vectors are normally distributed:

$$\mathbf{J}|\Xi \sim \mathcal{N}(\mathbf{m}, \mathbf{K}) \tag{3.29}$$

$$\hat{\mathbf{J}}|\mathbf{J}, \sigma^2 \sim \mathcal{N}(\mathbf{J}, \sigma^2\,\mathbf{I}), \tag{3.30}$$

where $\mathbf{m} = \{m_i\}$ is the mean vector with elements $m_i = \mu_0(\xi_i)$, and $\mathbf{K} = [K_{i,j}]$ is the covariance matrix (Gram matrix) of elements $K_{i,j} = \kappa(\xi_i, \xi_j)$.

Given a set of n normally distributed observations $\mathcal{D}_n = \left\{(\xi_i, \hat{J}_i)\right\}_{i=1}^{n}$ and an arbitrary evaluation point ξ, the posterior mean function (model prediction) μ_n and the posterior variance function (model uncertainty) σ_n^2 are calculated as follows:

$$\mu_n(\xi) = \mu_0(\xi) + \mathbf{k}(\xi)^T \left(\mathbf{K} + \sigma^2\mathbf{I}\right)^{-1} \left(\hat{\mathbf{J}} - \mathbf{m}\right) \tag{3.31}$$

$$\sigma_n^2(\xi) = \kappa(\xi, \xi) - \mathbf{k}(\xi)^T \left(\mathbf{K} + \sigma^2\mathbf{I}\right)^{-1} \mathbf{k}(\xi), \tag{3.32}$$

where $\mathbf{k}(\xi)$ is a vector of covariance terms between the arbitrary point ξ and the n evaluation points ξ_i collected in $\mathcal{D}_n$.

The covariance function κ determines the structural attributes of the objective functions that can be fitted (e.g., smoothness, robustness to additive noise, etc.). Here, as suggested by [157], the automatic relevance determination (ARD) Matérn 5/2 kernel function is considered. This covariance

function yields sample functions that are twice differentiable, aligning with the assumptions made by quasi-Newton methods, for example. It is more suitable for solving practical optimization problems compared to the commonly used squared exponential function, which generates sample functions that are unrealistically smooth. Hence, the covariance between two points ξ and ξ' is given by Eq 3.33.

$$\kappa(\xi, \xi') = \theta_0 \left(1 + \sqrt{5\, r^2(\xi, \xi')} + \frac{5}{3} r^2(\xi, \xi')\right) \exp\left(-\sqrt{5\, r^2(\xi, \xi')}\right), \quad (3.33)$$

with

$$r^2(\xi, \xi') = \sum_{d=1}^{D} \frac{(\xi_d - \xi'_d)^2}{\theta_d^2}, \quad (3.34)$$

where d indicates the d^{th} dimension of the points ξ and ξ' in the multidimensional space $\mathbb{R}^D$. The covariance amplitude θ_0 and the length scales $\theta_{1:D}$ are known as the hyperparameters of the kernel function.

As previously described, the acquisition function is responsible for the exploration-exploitation trade-off of BO method. The ideal acquisition function aims to find a balance between exploration, which involves exploring regions of higher variance, and exploitation, targeting areas where prediction errors are minimized. In the present work, a modified expected improvement (EI) function, $\mathbb{EI}$, is used. This function, implemented by *bayesopt* library in Matlab™[158], integrates an ϵ-greedy strategy to prevent the algorithm from becoming trapped in a local minimum, a problem that can occur with the traditional EI approach. This is done by combining the original EI approach with a random choice based on probability measures (for details on the algorithm see [159]). In the original approach, the new evaluation point ξ_{n+1} is obtained by maximizing the expected improvement with respect to the current optimum value, as follows:

$$\xi_{n+i} \;=\; \arg\max_{\xi} \mathbb{EI}(\xi; \mathcal{D}_n), \quad (3.35)$$

where $\mathbb{EI}(\xi; \mathcal{D}_n)$ is calculated as the maximum value between 0 and the difference between the lowest posterior mean μ_n^*, computed on the points in $\mathcal{D}_n$,

and the posterior mean of the arbitrary point $\mu_n(\xi)$:

$$\mathbb{EI}(\xi; \mathcal{D}_n) = \mathbb{E}\left[\max(0, \mu_n^* - \mu_n(\xi))\right]. \tag{3.36}$$

For more details on Bayesian optimization formalism, Gaussian Processes, and acquisition functions, refer to [143, 144, 159, 160, 161, 162, 163].

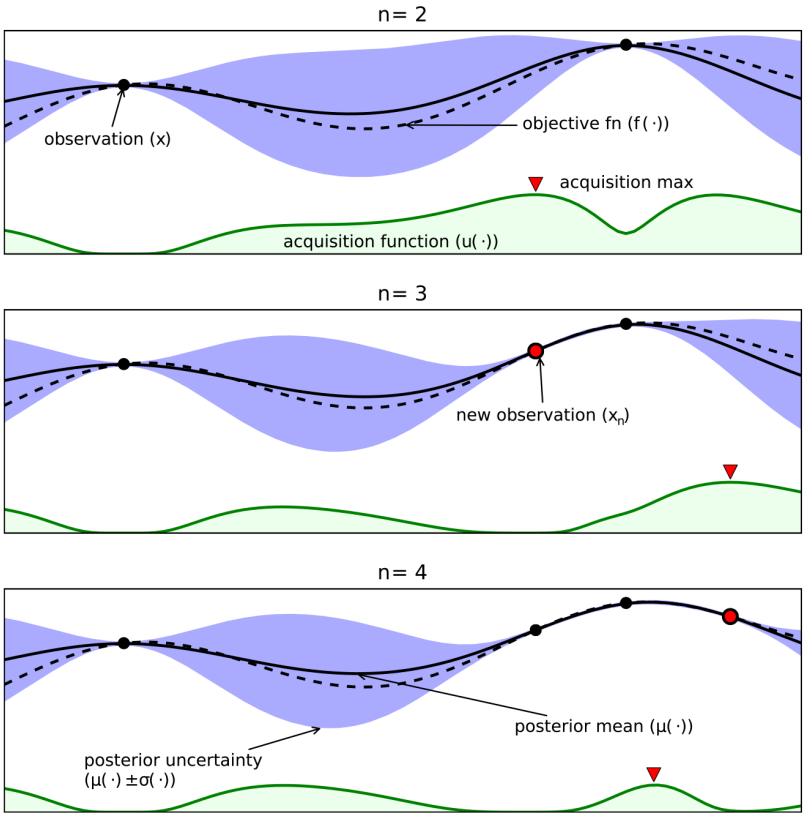

Figure 3.6: Bayesian optimization across three iterations [160].

Finally, Figure 3.6 summarizes the Bayesian optimization procedure for a one-dimensional maximization problem. The dashed curve represents the unknown objective function, while the continuous curve depicts the posterior mean. The shaded area around the mean curve shows the posterior confidence interval. During the initial iteration ($n = 2$), the prior is combined with two objective function evaluations to compute the posterior, which is

subsequently used to calculate the acquisition function, shown in the lower shaded plots. The acquisition function is high in regions where the model predicts a high objective function value and where prediction uncertainty is high, thus fostering exploitation and exploration, respectively. By maximizing the acquisition function, a new evaluation point is determined, and this process repeats over three iterations. As can be seen, the posterior updates at each step, gaining knowledge about J, and its uncertainty at the observed point decreases accordingly.

Chapter 4

Results

In order to evaluate the benefits, drawbacks, and potential opportunities associated with implementing CCD strategies in the HVAC&R sector, a comparison between the results provided by two different optimization approaches is carried out. On the one hand, a more traditional workflow, often adopted by the experts in this field, using the sequential optimization is considered. On the other, the simultaneous optimization approach is used due to its ability to ensure optimality even in the presence of bi-directional couplings. This choice is supported by the fact that, despite determining a larger optimization problem, in the considered case, the total number of variables remains relatively low.

In Section 4.1, the optimization problems of both the sequential and simultaneous approaches are formulated, and their respective black-box optimization frameworks are introduced. In both scenarios, Bayesian optimization is successfully implemented, allowing optimal values to be reached with a restricted number of iterations. Using the dynamic model, the chiller system operation is simulated across nine different operating conditions, defined by combinations of three external air temperature levels and three thermal loads (refer to Table 4.1). Throughout these simulations, the boundary conditions remain constant for a total simulation time of 30000 s, ensuring the attainment of steady-state conditions. Since we are primarily interested in steady-

state energy efficiency, transient operation performance can be neglected. Moreover, steady-state performance is sufficient for determining the static feedforward actions. Subsequently, steady-state quantities are leveraged by the Bayesian optimization method, and the solutions of each optimization problem are found for each operating condition. Both optimization methods aim to determine the optimal value of the design vector, ξ, encompassing a combination of design variables, $\xi_{\mathcal{P}}$, and control variables, $\xi_{\mathcal{C}}$, for the corresponding optimization problems. The outcomes of the considered co-design strategies are discussed in Section 4.2, and finally compared in subsection 4.2.3.

Table 4.1: Boundary conditions.

External air temperature T_{air}	
LT	20.7 °C
MT	25.5 °C
HT	30.4 °C

Thermal load $\dot{Q}_{load}$	
LTL	21.3 kW
MTL	42.6 kW
HTL	63.9 kW

4.1 Optimization Problems

4.1.1 Case 1: Sequential Optimization

As outlined in Section 3.5, the sequential approach involves two consecutive constrained optimization stages. Initially, the method focuses on the optimal design of the chiller system. Subsequently, upon completing the design optimization, the plant design variables are considered as parameters for the subsequent control system optimization step.

Continuing from what introduced in 3.3 and 3.4, the design optimization aims to find the optimal design variables $\xi_{\mathcal{P}}$ that minimizes the design objective function $J_{\mathcal{P}}$, which represents the overall volume of the gas-cooler $V_{GC,overall}$. As observed, the design parameters vector $\xi_{\mathcal{P}}$ encompasses the fin pitch $p_{f,GC}$ and row/tube pitch $p_{R/t,GC}$ of the gas-cooler, and fans impeller

diameter d_{fan}. The mathematical formulation of the design optimization problem can be written as follows:

$$\min_{\xi_P} \; J_{\mathcal{P}}\left(\xi_{\mathcal{P}}\right) = V_{GC,overall} \tag{4.1}$$

$$\text{decision variables: } \xi_{\mathcal{P}} = \left[p_{f,GC},\, p_{R/t,GC},\, d_{fan}\right] \tag{4.2}$$

$$\text{subject to: } g_{\mathcal{P},1} = 0.85\,\zeta_0 - \zeta \leq 0 \tag{4.3}$$

$$g_{\mathcal{P},2} = \zeta - 1.15\,\zeta_0 \leq 0 \tag{4.4}$$

$$g_{\mathcal{P},3} = 0.98\,\sigma_0 - \sigma \leq 0 \tag{4.5}$$

$$g_{\mathcal{P},4} = T_B - T_{B,0} \leq 0 \tag{4.6}$$

$$g_{\mathcal{P},5} = P_{tot} - P_{tot,0} \leq 0 \tag{4.7}$$

$$\dot{x} = f_{\xi_{\mathcal{P}}}\left(x, u, d\right) = 0 \tag{4.8}$$

$$y = r_{\xi_{\mathcal{P}}}\left(x, u, d\right) \tag{4.9}$$

$$\underline{\xi_{\mathcal{P}}} \leq \xi_{\mathcal{P}} \leq \overline{\xi_{\mathcal{P}}} \tag{4.10}$$

$$\text{with: } \zeta = \frac{\pi\, d_{fan}^2}{l_{GC}\, h_{GC}} \tag{4.11}$$

$$\sigma = \frac{A_{fr,n,GC}}{A_{fr,GC}} = \frac{\left(p_{t,GC} - d_{e,GC}\right)\left(p_{f,GC} - t_{f,GC}\right)}{p_{t,GC}\, p_{f,GC}}. \tag{4.12}$$

The minimization problem is subject to both plant inequality constrains $g_{\mathcal{P},1-3}$ and performance inequality constraints $g_{\mathcal{P},4-5}$, while f and r represent the dynamics of the system. Here, x, u, and d, denote states, inputs, and disturbances, respectively. The states x correspond to all the states of the graph nodes. The inputs u include the opening of the valve o_{BPV}, the rotational speed of the fans n_{fan}, and the compressor speed n_C. Finally, the external air temperature T_{air} and the thermal loda $\dot{Q}_{load}$ represent the disturbances d to the system. Eq. 4.8 specifies that the optimization exclusively accounts for steady-state conditions.

The plant inequality constraints $g_{\mathcal{P},1}$ and $g_{\mathcal{P},2}$ are geometric constraints, enforcing the ratio ζ — cross-sectional area of airflow passage in the four fans to total gas-cooler cross-sectional area — to remain within $\pm 15\%$ of the ratio computed based on the nominal design configuration. These are implemented to consider the fluid dynamics aspects associated with the airflow transition

from the outlet of the gas-cooler to the inlet of the fans. A third geometric inequality constraint $g_{\mathcal{P},3}$ is introduced to limit the ratio σ — net cross-sectional area to total cross-sectional area of the gas-cooler — to be greater than 98% of the nominal ratio σ_0. Local air pressure losses and fouling effect in the plate-fin heat exchangers are strictly related to σ. Feasible design solutions must ensure that its value is high enough to reduce these drawbacks.

The performance inequality constraints are contemplated to limit the search to those solutions that guarantee at least the same performance level as the nominal configuration. On the one hand, the function $g_{\mathcal{P},4}$ ensures that feasible solutions provide water to the building at a temperature T_B equal or lower than the nominal case $T_{B,0}$; on the other, $g_{\mathcal{P},5}$ limits total power consumption P_{tot} to be equal or lower than $P_{tot,0}$. The supply water temperature $T_{B,0}$ and the power consumption $P_{tot,0}$ are computed for each operating condition by simulating the system in a fully open-loop configuration (i.e., no PI controllers), fixing design and control parameters to their nominal values (refer to Table 3.1 and Table 3.2). Finally, bound constraints are also considered, where $\underline{\xi_{\mathcal{P}}}$ and $\overline{\xi_{\mathcal{P}}}$ denote the lower and upper bounds for the design variables, respectively. These bounds are calculated as -15% and $+15\%$ of the nominal design values (see Table 4.2).

Table 4.2: Lower and upper bounds of the design optimization variables.

	$\underline{\xi_{\mathcal{P}}}$	$\overline{\xi_{\mathcal{P}}}$
d_{fan}	769 mm	1041 mm
$p_{f,GC}$	1.78 mm	2.42 mm
$p_{R/t,GC}$	19.9 mm	26.9 mm

Figure 4.1 depicts the search space of the design optimization problem for three different operating conditions, obtained by conducting a screening of simulations with $\xi_{\mathcal{P}}$ ranging between $\underline{\xi_{\mathcal{P}}}$ and $\overline{\xi_{\mathcal{P}}}$, and the control parameters fixed at their nominal values. Each surface represents the upper bound of an inequality constraint, and the space of feasible solutions stands between the

upper bounds of $g_{\mathcal{P},1}$, $g_{\mathcal{P},3}$, $g_{\mathcal{P},4}$, and $g_{\mathcal{P},5}$, in all the considered cases. In the feasible region, the figure shows isosurfaces corresponding to different levels of the objective function $J_{\mathcal{P}}$.

As can be seen, $J_{\mathcal{P}}$ decreases moving towards the intersection among the upper bounds of $g_{\mathcal{P},3}$, $g_{\mathcal{P},4}$, and $g_{\mathcal{P},5}$, where it reaches a minimum value, dependent on the operating condition under consideration.

Once the optimal design is determined, the optimized design variables $\xi^*_{\mathcal{P}}$ are treated as parameters in the control optimization. Here, the objective function $J_{\mathcal{C}}$ represents the total power consumption of the chiller system P_{tot}, which is the summation between the compressor power consumption P_C and the power consumption of the four fans P_{fans}. The control optimization aims to find the couple of control set-points, fans rotational speed n_{fan} and valve opening o_{BPV}, that minimizes $J_{\mathcal{C}}$, while the compressor rotational speed n_C is regulated by the decentralized controller to maintain the supply water temperature T_B at the prescribed set-point T^*_B, as illustrated in Section 2.6. Mathematically, the control optimization problem can be expressed as:

$$\min_{\xi_{\mathcal{C}}} \; J_{\mathcal{C}}\left(\xi^*_{\mathcal{P}}, \xi_{\mathcal{C}}\right) = P_{tot} \tag{4.13}$$

$$\text{decision variables: } \xi_{\mathcal{C}} = [n_{fan},\, o_{BPV}] \tag{4.14}$$

$$\text{subject to: } g_{\mathcal{C},1} = T_B - T^*_B \leq 0 \tag{4.15}$$

$$\dot{x} = f_{\xi^*_{\mathcal{P}},\xi_{\mathcal{C}}}\left(x, u, d\right) = 0 \tag{4.16}$$

$$y = h_{\xi^*_{\mathcal{P}},\xi_{\mathcal{C}}}\left(x, u, d\right) \tag{4.17}$$

$$\underline{\xi_{\mathcal{C}}} \leq \xi_{\mathcal{C}} \leq \overline{\xi_{\mathcal{C}}}. \tag{4.18}$$

In this case, the optimization problem incorporates a single inequality constraint, denoted as $g_{\mathcal{C},1}$, restricting feasible solutions to supply chilled water at a temperature equal to or below the set-point T^*_B. The bound constraints $\underline{\xi_{\mathcal{C}}}$ and $\overline{\xi_{\mathcal{C}}}$ are shown in Table 4.3, while the saturation limits the compressor frequency to remain within 30 Hz and 60 Hz (i.e., 870 rpm and 1740 rpm). Note that the values of the fan speed correspond to fans power

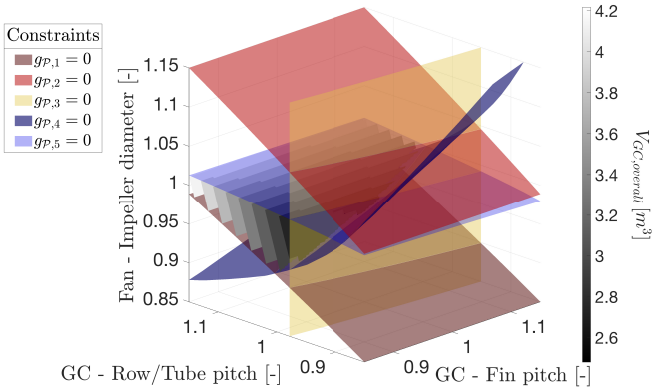

(a) Operating condition: MT-LTL

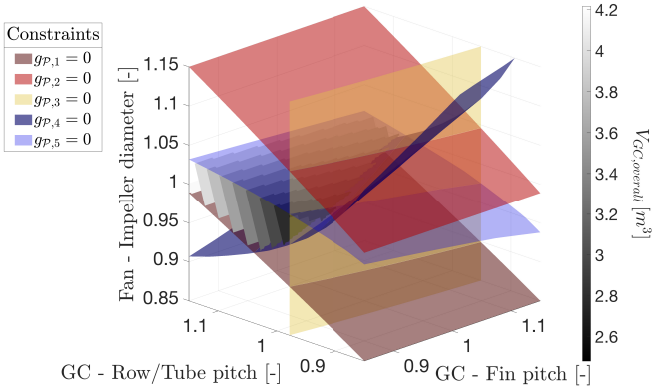

(b) Operating condition: MT-MTL

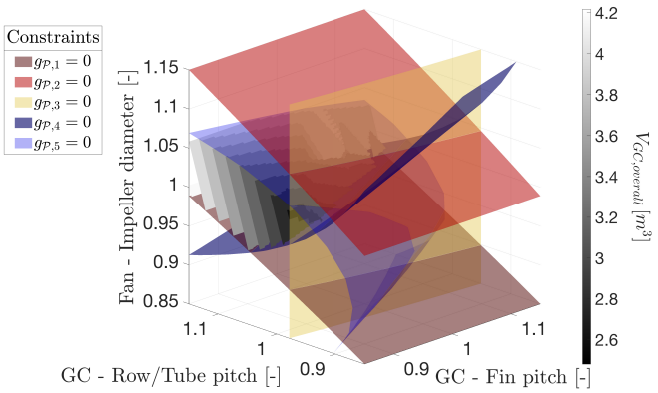

(c) Operating condition: MT-HTL

Figure 4.1: Search space of the design optimization problem.

supply frequency of 30 Hz and 60 Hz[1], respectively.

Table 4.3: Lower and upper bounds of the control optimization variables.

	$\underline{\xi_{\mathcal{C}}}$	$\overline{\xi_{\mathcal{C}}}$
n_{fan}	318 rpm	636 rpm
o_{BPV}	0.04	0.125

The search space of the control optimization problem, depicted in Figure 4.2, is obtained by conducting a screening of simulations with $\xi_{\mathcal{C}}$ ranging between $\underline{\xi_{\mathcal{C}}}$ and $\overline{\xi_{\mathcal{C}}}$, and the design parameters equal to the previously found optimized values $\xi^*_{\mathcal{C}}$. The contour lines refer to different levels of total power consumption P_{tot}, whereas the color shaded areas denote regions of the search space where $g_{\mathcal{C},1}$ is violated, considering T^*_B as 8 °C. In each scenario, the minimum value appears to be situated within a delimited portion of the search space. The results refer to the same operating conditions of Figure 4.1.

It is noteworthy that the inclusion of constraints $g_{\mathcal{P},4}$ and $g_{\mathcal{P},5}$ (Eqs. 4.1-4.12) introduces a partial bi-directional coupling between the design and control optimization problems. While the objective functions of both optimization problems exhibit uni-directional coupling, the performance inequality constraints considered in the design optimization also depend on the control parameters. This is supported by the results in Figure 3.3b, which highlights the significance of the control variables on the total power consumption of the system. Indeed, while varying the rotational speed of the fans, n_{fan}, directly affects power consumption, adjusting the valve opening, o_{BPV}, impacts power consumption indirectly through the operation of the compressor. Opening or closing the valve alters the pressure losses across the valve and consequently through the refrigerant circuit, thus, at constant compressor rotational speed, the mass flow rate provided by the compressor and the refrigerant pressure levels change. This action, in turn, influences the cooling capacity of the chiller, subsequently affecting the supply water temperature,

[1]Varying the power supply frequency between 30 Hz and 60 Hz is equivalent to scaling the nominal rotational speed, set at 50 Hz, by factors of 0.6 and 1.2, respectively.

T_B.

Finally, this emphasizes that the control architecture cannot be completely ignored in the design optimization process [38], and highlights the importance of accounting for system dynamics at that stage as well. Hence, the performance inequality constraints can be referred to as coupling inequality constraints, and they aim to orient the resultant design for effective control and guarantee the feasibility of a viable control design, thus providing a slight modification to the traditional sequential approach.

Algorithmic approach

The sequential optimization problem seamlessly integrates into a black-box optimization framework that uses Bayesian optimization for solving. The corresponding Algorithm 1 outlines the shared procedural steps for both design and control optimizations. As described in subsection 3.6.1, Gaussian processes serve as a probabilistic surrogate model, denoted as $\hat{\varphi}$, to approximate the unknown and costly-to-evaluate objective function J. Additionally, a modified expected improvement function is used as the acquisition function $\mathcal{A}$, as mentioned in subsection 3.6.1.

The algorithm starts by sampling optimization variables ξ to generate evaluations $\hat{J}$ of the objective function (line 1). The resulting dataset $\mathcal{D}$ is used in the learning phase of the statistical model $\hat{\varphi}$ (line 2), subsequently providing predictive mean and variance. These statistical quantities are employed in constructing the acquisition function, which is maximized to select the next evaluation candidate point ξ_+ within the bound constraints (line 4). Subsequently, this point generates a new evaluation $\hat{J}_+$ (line 5) and the new point $(\xi_+, \hat{J}_+)$ is incorporated into the historical data $\mathcal{D}$ (line 6), updating the dataset to $\mathcal{D}_+$ and refining the statistical model $\hat{\varphi}$ (line 7). Steps 4-7 are repeated for a specified number of cycles. The solution for each optimization problem is determined by identifying the evaluation point that satisfies all inequality constraints ($g \leq 0$) and simultaneously minimizes the corresponding surrogate statistical model $\hat{\varphi}$.

In the sequential approach, the control variables $\xi_{\mathcal{C}}$ are treated as param-

eters during the evaluations of the objective function in the design optimization. The resulting output $\xi_{\mathcal{P}}^*$ becomes a parameter in the subsequent control optimization step, ultimately providing the optimized control variables $\xi_{\mathcal{C}}^*$ as the final result.

Algorithm 1 Sequential Optimization through Bayesian Optimization

Design Optimization

Input: $\xi_{\mathcal{P}} \in \left[\underline{\xi_{\mathcal{P}}}, \overline{\xi_{\mathcal{P}}}\right]$ {**Parameters:** $\xi_{\mathcal{C}} = \xi_{\mathcal{C},0}$}

1: Initialize dataset $\mathcal{D}_{\mathcal{P},n}$ with input samples $\Xi_{\mathcal{P},n} = [\xi_{\mathcal{P},1}, \xi_{\mathcal{P},2}, \cdots, \xi_{\mathcal{P},n}]$ and evaluations $\Gamma_{\mathcal{P},n} = \left[\hat{J}_{\mathcal{P}}(\xi_{\mathcal{P},1}), \hat{J}_{\mathcal{P}}(\xi_{\mathcal{P},2}), \cdots, \hat{J}_{\mathcal{P}}(\xi_{\mathcal{P},n})\right]$
2: Build statistical model $\hat{\varphi}_{\mathcal{P}}$
3: **for** *each iteration* i **do**
4: select a sample $\xi_{\mathcal{P},n+i}$ by optimizing acquisition function $\mathcal{A}_{\mathcal{P}}$
$\xi_{\mathcal{P},n+i} = \arg\max_{\xi_{\mathcal{P}}} \mathcal{A}_{\mathcal{P}}(\xi_{\mathcal{P}}; \mathcal{D}_{\mathcal{P},n+i-1})$
5: run simulation for $\xi_{\mathcal{P},n+i}$ to obtain $\hat{J}_{\mathcal{P},n+i}$
6: augment data $\mathcal{D}_{\mathcal{P},n+i} = \{\mathcal{D}_{\mathcal{P},n+i-1}, (\xi_{\mathcal{P},n+i}, \hat{J}_{\mathcal{P},n+i})\}$
7: update statistical model $\hat{\varphi}_{\mathcal{P}}$
8: **end for**

Output: $\xi_{\mathcal{P}}^*$

Control Optimization

Input: $\xi_{\mathcal{C}} \in \left[\underline{\xi_{\mathcal{C}}}, \overline{\xi_{\mathcal{C}}}\right]$ {**Parameters:** $\xi_{\mathcal{P}} = \xi_{\mathcal{P}}^*$}

1: Initialize dataset $\mathcal{D}_{\mathcal{C},m}$ with input samples $\Xi_{\mathcal{C},m} = [\xi_{\mathcal{C},1}, \xi_{\mathcal{C},2}, \cdots, \xi_{\mathcal{C},m}]$ and evaluations $\Gamma_{\mathcal{C},m} = \left[\hat{J}_{\mathcal{C}}(\xi_{\mathcal{C},1}), \hat{J}_{\mathcal{C}}(\xi_{\mathcal{C},2}), \cdots, \hat{J}_{\mathcal{C}}(\xi_{\mathcal{C},m})\right]$
2: Build statistical model $\hat{\varphi}_{\mathcal{C}}$
3: **for** *each iteration* j **do**
4: select a sample $\xi_{\mathcal{C},m+j}$ by optimizing acquisition function $\mathcal{A}_{\mathcal{C}}$
$\rightarrow \xi_{\mathcal{C},m+j} = \arg\max_{\xi_{\mathcal{C}}} \mathcal{A}_{\mathcal{C}}(\xi_{\mathcal{C}}; \mathcal{D}_{\mathcal{C},m+j-1})$
5: run simulation for $\xi_{\mathcal{C},m+j}$ to obtain $\hat{J}_{\mathcal{C},m+j}$
6: augment data $\mathcal{D}_{\mathcal{C},m+j} = \{\mathcal{D}_{\mathcal{C},m+j-1}, (\xi_{\mathcal{C},m+j}, \hat{J}_{\mathcal{C},m+j})\}$
7: update statistical model $\hat{\varphi}_{\mathcal{C}}$
8: **end for**

Output: $\xi_{\mathcal{C}}^*$

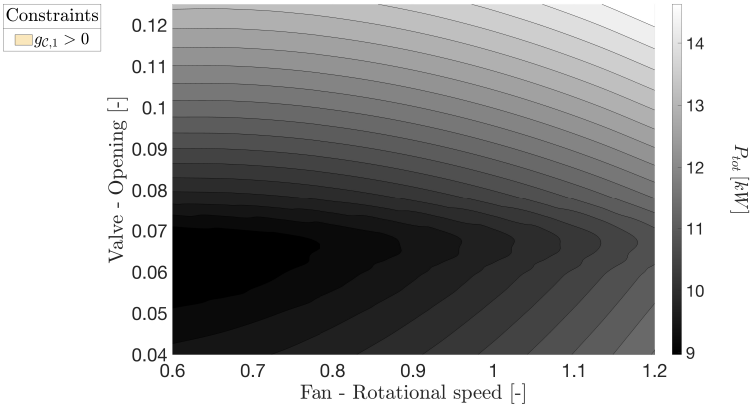

(a) Operating condition: MT-LTL

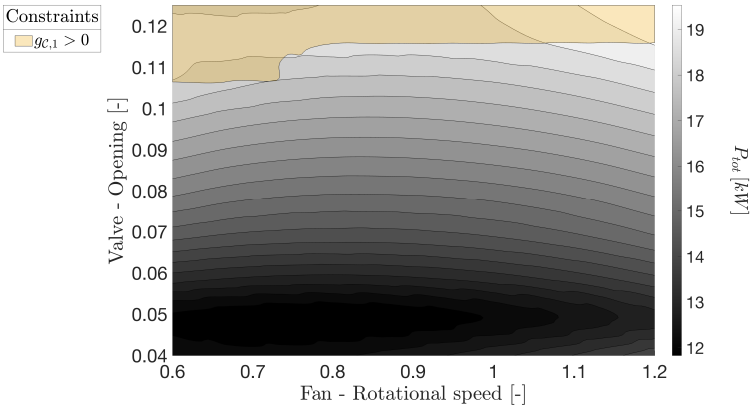

(b) Operating condition: MT-MTL

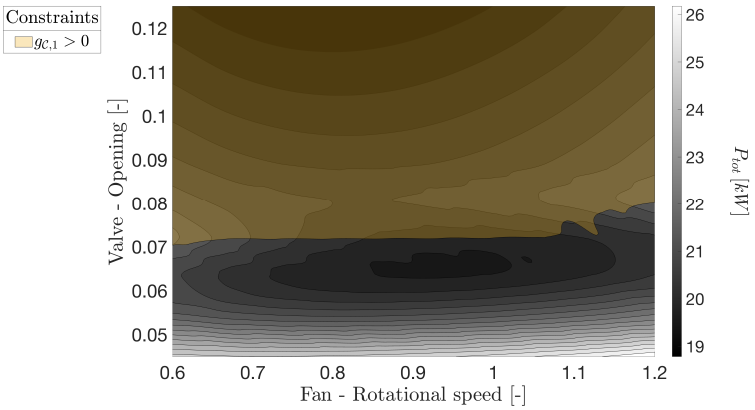

(c) Operating condition: MT-HTL

Figure 4.2: Search space of the control optimization problem, with T_B^* equal to 8 °C.

4.1.2 Case 2: Simultaneous Optimization

In the simultaneous approach, the overall objective function J of the multiobjective optimization problem is derived using the weighted-sum method [96]. This implies that J represents a linear combination of both the design and control objective functions, where the positive normalized weight θ quantifies the trade-off between these objectives. The mathematical formulation of the simultaneous optimization problem is detailed in Eqs. 4.19-4.30. The design variables and constraints encompass those outlined in the previously introduced optimization problems. Consequently, the inequality constraints g_{1-3} align with $g_{\mathcal{P},1-3}$ from the design optimization problem, while g_4 corresponds to $g_{\mathcal{C},1}$ considered in the control optimization problem. Furthermore, g_4 replaces $g_{\mathcal{P},4}$, while the performance inequality constraint $g_{\mathcal{P},5}$ is not explicitly addressed here, as it is implicitly accounted for within the control objective function $J_{\mathcal{C}}$.

$$\min_{\xi_{\mathcal{P}},\xi_{\mathcal{C}}} \; J(\xi_{\mathcal{P}},\xi_{\mathcal{C}}) \;=\; \theta\, J_{\mathcal{P}}(\xi_{\mathcal{P}}) + (1-\theta)\, J_{\mathcal{C}}(\xi_{\mathcal{P}},\xi_{\mathcal{C}}) \tag{4.19}$$

$$\text{decision variables: } \xi_{\mathcal{P}} \;=\; \left[p_{f,GC},\, p_{R/t,GC},\, d_{fan}\right] \tag{4.20}$$

$$\xi_{\mathcal{C}} \;=\; [n_{fan},\, o_{BPV}] \tag{4.21}$$

$$\text{subject to: } g_1 \;=\; 0.85\,\zeta_0 - \zeta \leq 0 \tag{4.22}$$

$$g_2 \;=\; \zeta - 1.15\,\zeta_0 \leq 0 \tag{4.23}$$

$$g_3 \;=\; 0.98\,\sigma_0 \;-\; \sigma \leq 0 \tag{4.24}$$

$$g_4 \;=\; T_B - T_B^* \leq 0 \tag{4.25}$$

$$\dot{x} = f_{\xi_{\mathcal{P}},\xi_{\mathcal{C}}}\,(x,u,d) = 0 \tag{4.26}$$

$$y = r_{\xi_{\mathcal{P}},\xi_{\mathcal{C}}}\,(x,u,d) \tag{4.27}$$

$$\underline{\xi_{\mathcal{P}}} \leq \xi_{\mathcal{P}} \leq \overline{\xi_{\mathcal{P}}} \tag{4.28}$$

$$\underline{\xi_{\mathcal{C}}} \leq \xi_{\mathcal{C}} \leq \overline{\xi_{\mathcal{C}}} \tag{4.29}$$

$$\text{with: } \theta \in [0,1]. \tag{4.30}$$

Algorithmic approach

Similar to the sequential approach, the simultaneous optimization problem is incorporated into a black-box optimization framework based on Bayesian optimization. The proposed algorithm, presented in Algorithm 2, follows the same main steps as in subsection 4.1.1. The output of the algorithm is the optimized co-design vector ξ^* that minimizes the surrogate statistical model $\hat{\varphi}$ of the overall objective function J.

Algorithm 2 Simultaneous Optimization through Bayesian Optimization

Input: $\xi = [\xi_{\mathcal{P}}, \xi_{\mathcal{C}}] \in \left[\underline{\xi}, \overline{\xi}\right]$, with $\xi_{\mathcal{P}} \in \left[\underline{\xi_{\mathcal{P}}}, \overline{\xi_{\mathcal{P}}}\right]$ and $\xi_{\mathcal{C}} \in \left[\underline{\xi_{\mathcal{C}}}, \overline{\xi_{\mathcal{C}}}\right]$

1: Initialize dataset $\mathcal{D}_l$ with input samples $\Xi_l = [\xi_1, \xi_2, \cdots, \xi_l]$ and evaluations $\Gamma_l = \left[\hat{J}(\xi_1), \hat{J}(\xi_2), \cdots, \hat{J}(\xi_l)\right]$
2: Build statistical model $\hat{\varphi}$
3: **for** *each iteration* k **do**
4: select a sample ξ_{l+k} by optimizing acquisition function $\mathcal{A}$ $\{\xi_{l+k} = \arg\max_{\xi} \mathcal{A}(\xi; \mathcal{D}_{l+k-1})\}$
5: run simulation for ξ_{l+k} to obtain $\hat{J}_{l+k}$
6: augment data $\mathcal{D}_{l+k} = \{\mathcal{D}_{l+k-1}, (\xi_{l+k}, \hat{J}_{l+k})\}$
7: update statistical model $\hat{\varphi}$
8: **end for**

Output: ξ^*

4.2 Optimization Results

The sequential and simultaneous optimization problems are solved using their corresponding algorithms, Algorithm 1 and Algorithm 2. This involves performing three distinct optimizations: two for each subproblem within the sequential approach and one for the simultaneous strategy. Each optimization applies a maximum of 60 iterations for the Bayesian optimization method, which is implemented using *bayesopt* library in Matlab™[158]. The outcomes of the sequential optimization can be found in subsection 4.2.1, whereas the results of the simultaneous optimization are detailed in subsection 4.2.2. In subsection 4.2.3, the results of these two approaches are compared and a convergence analysis of the three optimizations is commented.

4.2.1 Case 1: Sequential Optimization

The design and control optimization problems, formulated in subsection 4.1.1, are solved for each operating condition in Table 4.1. The design optimization provides the optimized design variables $\xi^*_{\mathcal{P}}$ to the subsequent control optimization step, which, in turn, leads to the optimized control variables $\xi^*_{\mathcal{C}}$. The results of the sequential approach are outlined in Table 4.4a. The optimal values of fin $p_{f,GC}$ and row/tube $p_{R/t,GC}$ pitches of the gas-cooler, impeller diameter d_{fan} and rotational speed n_{fan} of the fans, and valve opening o_{BPV}, are summarized along with their corresponding minimized objective functions. Furthermore, the values of design and control objective functions are combined using Eq. 4.19 with the weight θ equal to 0.4, for comparison purposes, as will be described further in this section.

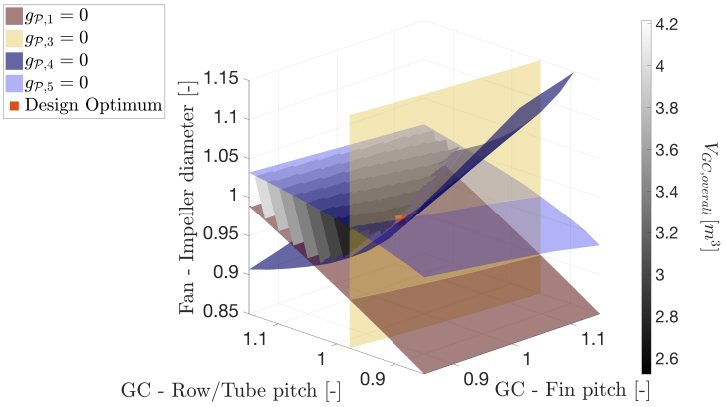

Figure 4.3: Design optimization solution for MT-MTL.

Figure 4.3 represents the optimal point within the search space for the design optimization under MT-MTL operating condition, while Figure 4.4 depicts the corresponding optimal point for the control optimization under a different operating condition. As can be seen, Bayesian optimization provide feasible solutions and locate both optimal points in the regions described in subsection 4.1.1, as expected.

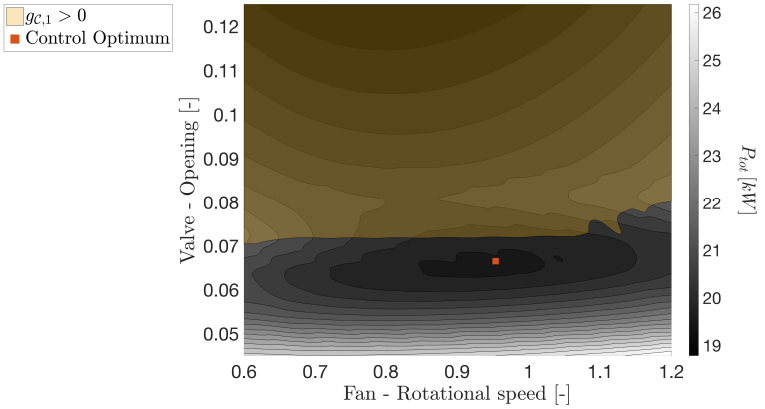

Figure 4.4: Control optimization solution for MT-HTL.

4.2.2 Case 2: Simultaneous Optimization

The solution to the bi-objective co-design problem, as expressed by Eqs. 4.19-4.30, forms a Pareto set. The different Pareto points within this set are determined by adjusting the weight parameter θ between 0 and 1. Figure 4.6 depicts the Pareto fronts obtained by fitting a continuous curve on the Pareto sets, identified by solving the simultaneous optimization problem, outlined in subsection 4.1.2, across every operating condition of Table 4.1. The normalized objective function values $\widetilde{J}_{\mathcal{P}}$ and $\widetilde{J}_{\mathcal{C}}$ are computed dividing each $J_{\mathcal{P}}$ and $J_{\mathcal{C}}$ by their corresponding extreme values $J_{\mathcal{P},\theta=1}$ and $J_{\mathcal{C},\theta=0}$, which are determined by optimizing Eq. 4.19 with the weight θ equal to 1 and 0, respectively. The resulting Pareto fronts are all convex and represent system optimal. Additionally, they provide valuable insights into the trade-offs between the plant and controller objectives for the designer. Finally, Table 4.4b presents the results of the simultaneous optimization for θ equal to 0.4.

4.2.3 Comparison

The two co-design strategies are compared by calculating the percent reduction $\Delta J_{\%}$, as per Eq. 4.31, from the optimal values of $J_{\mathcal{P}}$, $J_{\mathcal{C}}$, and J, of both the sequential and the simultaneous optimizations (refer to Table 4.4a and Table 4.4b, respectively). As mentioned in subsection 4.2.2, the simulta-

neous optimization employed the weight θ equal to 0.4. This same weight is used to compute the overall optimal J, as seen in Table 4.4a, using Eq. 4.19 and combining the optimized design and control objective function values. The resulting percent reductions are summarized in Table 4.4c.

$$\Delta J_{\%} = 100 \frac{J_{sim} - J_{seq}}{J_{seq}}, \tag{4.31}$$

where J_{seq} and J_{sim} are the values of the overall objective functions of the sequential and simultaneous approaches, respectively.

The simultaneous optimization strategy demonstrates higher reductions in total power consumption when the thermal load reaches medium to high levels. This, however, coincides with a significant increase in gas-cooler volume. Moreover, for the specified value of θ, the simultaneous approach does not always ensure a reduction in both the design and control objective functions at the same time. Notwithstanding this trade-off, the simultaneous approach outperforms the sequential strategy by attaining a consistently lower minimum of the overall objective function J across all operating conditions. This is also confirmed by the Pareto fronts in Figure 4.6. As can be seen, for medium to high thermal loads, the sequential optimal points are dominated by the Pareto sets, thus highlighting the advantages associated with the simultaneous optimization strategy. However, for low thermal loads (i.e., LTL), the differences between the two approaches decrease. In fact, in this case, the solutions from the sequential approach precisely align with the Pareto front.

Convergence analysis

As described in the introduction to this section, each optimization problem is solved using *bayesopt* library in Matlab™, exploiting a parallel pool of six workers. The simulation environment is implemented in Matlab™, and each model run is performed for a simulation time of 30000 s using the variable step solver *ode23tb* on a *MacBookPro17,1* with chip *Apple M1*.

Figure 4.5 presents a comparison of the iterations executed by the Bayesian optimization method to reach the minimum across various optimization prob-

Table 4.4: Optimization results.

(a) Sequential optimization results.

	LT			**MT**			**HT**		
	LTL	**MTL**	**HTL**	**LTL**	**MTL**	**HTL**	**LTL**	**MTL**	**HTL**
$p_{f,GC}$ [mm]	1.99	1.94	1.83	2.08	1.95	1.95	2.30	1.97	1.89
$p_{R/t,GC}$ [mm]	22.65	22.74	22.96	22.57	22.69	22.70	22.39	22.78	22.80
d_{fan} [mm]	896.2	900.1	915.0	901.2	901.1	904.2	901.5	904.1	915.3
n_{fan} [rpm]	319.4	378.7	461.6	523.8	492.5	491.0	580.9	497.0	476.0
o_{BPV} [−]	0.085	0.046	0.066	0.065	0.046	0.067	0.051	0.045	0.064
$J_{\mathcal{P}}$ [m^3]	2.52	2.53	2.56	2.47	2.51	2.50	2.40	2.53	2.50
$J_{\mathcal{C}}$ [kW]	7.49	9.19	15.40	8.82	11.57	19.52	10.10	14.81	24.53
J [−], with $\theta = 0.4$	5.50	6.53	10.26	6.28	7.95	12.71	7.02	9.90	15.72

(b) Simultaneous optimization results for $\theta = 0.4$.

	LT			**MT**			**HT**		
	LTL	**MTL**	**HTL**	**LTL**	**MTL**	**HTL**	**LTL**	**MTL**	**HTL**
$p_{f,GC}$ [mm]	2.00	1.86	1.81	2.26	1.80	1.80	2.18	1.80	1.80
$p_{R/t,GC}$ [mm]	22.67	22.81	22.90	22.39	22.89	24.87	22.57	23.26	24.69
d_{fan} [mm]	934.5	953.0	959.9	934.5	952.3	998.7	943.1	960.6	995.4
n_{fan} [rpm]	322.6	329.7	456.5	571.1	455.5	455.1	549.9	453.5	455.3
o_{BPV} [−]	0.086	0.047	0.066	0.064	0.047	0.068	0.051	0.046	0.064
$J_{\mathcal{P}}$ [m^3]	2.39	2.38	2.39	2.30	2.41	2.98	2.33	2.51	2.92
$J_{\mathcal{C}}$ [kW]	7.54	9.14	15.38	8.92	11.50	18.87	10.14	14.65	24.01
J [−], with $\theta = 0.4$	5.48	6.44	10.18	6.27	7.86	12.51	7.02	9.79	15.58

(c) Percent reduction table.

	LT			**MT**			**HT**		
	LTL	**MTL**	**HTL**	**LTL**	**MTL**	**HTL**	**LTL**	**MTL**	**HTL**
$\Delta J_{\mathcal{P},\%}$	**-4.80**	**-5.94**	**-6.77**	**-6.98**	**-3.99**	18.98	**-3.06**	**-0.78**	16.79
$\Delta J_{\mathcal{C},\%}$	0.68	**-0.47**	**-0.12**	1.09	**-0.66**	**-3.34**	0.44	**-1.08**	**-2.11**
$\Delta J_{\%}$, with $\theta = 0.4$	**-0.32**	**-1.32**	**-0.78**	**-0.18**	**-1.08**	**-1.58**	**-0.04**	**-1.05**	**-0.91**

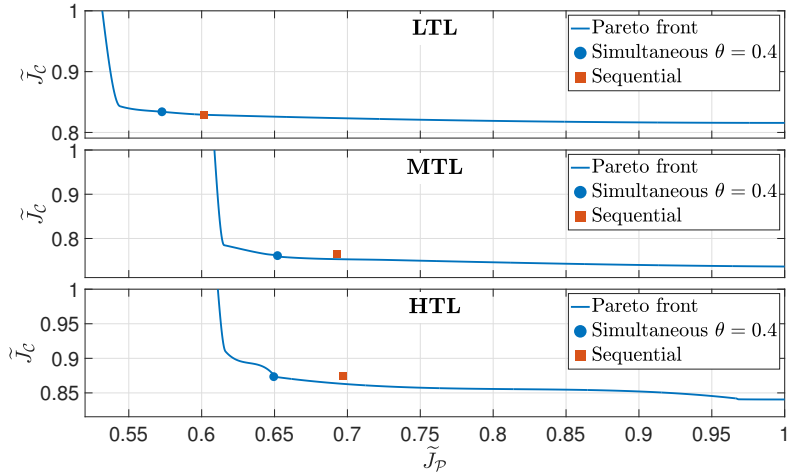

(a) T_{air}: LT

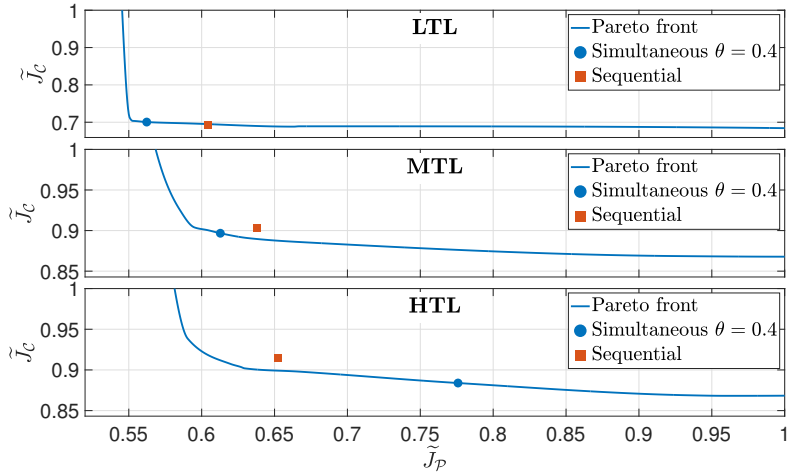

(b) T_{air}: MT

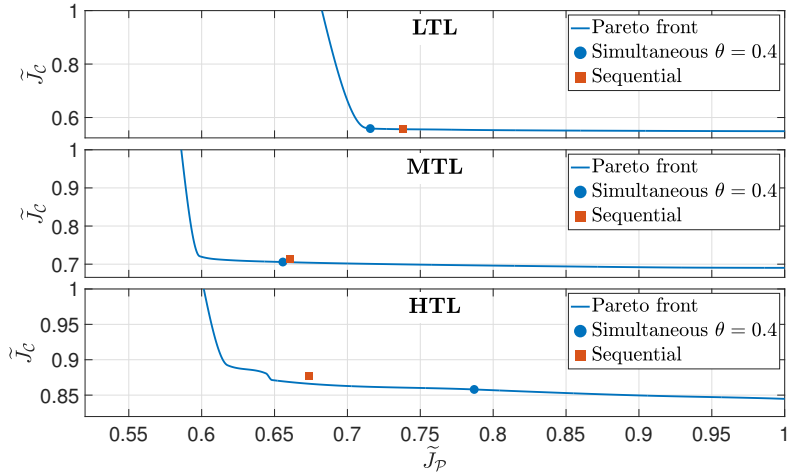

(c) T_{air}: HT

Figure 4.6: Pareto fronts.

lems and operating conditions. The first and second columns display the outcomes of design and control optimizations, respectively, using the sequential strategy, while the third column illustrates the convergence plots for the simultaneous approach with $\theta = 0.4$. It also distinguishes between iterations for feasible and unfeasible solutions.

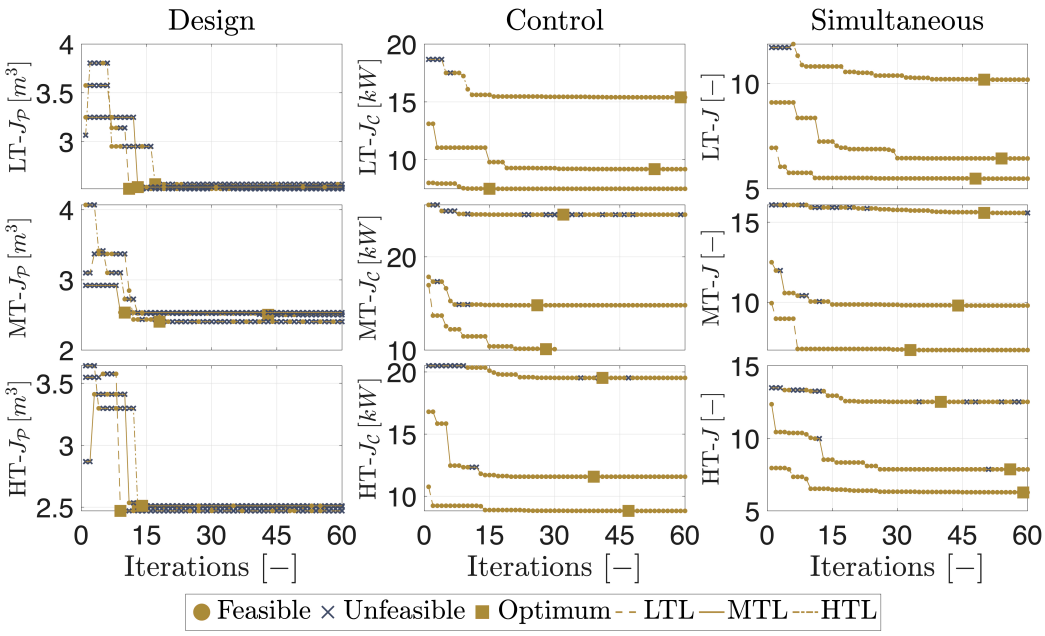

Figure 4.5: Convergence plots.

On average, the design, control, and simultaneous optimizations require 16.4, 37.8, and 48.2, iterations, respectively, to achieve the optimal solution. The average computation times for these are 234.3 s, 3389 s, and 4122 s, respectively. So, the sequential approach needs 52.4 iterations and 3623 s on average to reach the solution. Therefore, despite a notable reduction in mean iteration numbers by 11.1 %, the simultaneous strategy experiences a 13.8 % increase in average computation time. This can be justified by the higher number of optimization variables (i.e., 5) compared to both the design (i.e., 3) and the control (i.e., 3) optimization problems, which confirms the advantages of the sequential approach from the computational point of view.

Chapter 5

Conclusions

5.1 Summary

The optimal design and effective control of HVAC&R systems are essential to meet the requirements of devices aiming to reduce the environmental impact associated with the planet's energy resource consumption. This optimization is also critical to ensure efficient operation tailored to the specific needs present in various contexts where such systems are employed.

Often, traditional design approaches for complex systems, typically involving sequential optimization of design and control system, prove to be limited and capable of providing only suboptimal solutions. Conversely, design approaches based on optimization strategies belonging to the class of Control Co-Design approaches can ensure the achievement of optimal configurations.

In this context, this dissertation focuses on the control co-design problem of a CO_2-based chiller system, employing a graph-based model and black-box optimization.

5.2 Research contributions

This thesis has addressed the Control Co-Design of a potential fundamental element in HVAC&R installations, namely a CO_2-based chiller. In

particular, it has demonstrated the effective application of the Multi-state Convervation-based Graph-based Modeling Toolbox in conjunction with Bayesian optimization methods to design the following:

1. Physical characteristics of a critical component of the cooling system, including the fin pitch, row/tube pitch, and the impeller diameter of the gas-cooler fans.

2. Feedforward control actions for the back pressure valve opening degree and fan rotational speed.

This has entailed taking into account the interplay between control system and the physical components throughout the design process. The CCD guarantees the mutual optimization of both the control system and the chiller unit to enhance efficiency and effectiveness in operation. Importantly, it strives to minimize the environmental impact linked to energy resource consumption for a sustainable innovation.

Through extensive simulations, it has been shown that simultaneous design approach consistently outperforms the traditional sequential strategy, wherein control design is typically developed at the end, optimizing the chiller functioning across various operating conditions. However, it is important to acknowledge the limitations inherent in this research, particularly the exclusive focus on steady-state operating conditions and the lack of an exhaustive analysis of the couplings between the two design subproblems.

5.3 Future Work

This thesis paves the way to the development of a robust framework to tackle CCD problems for HVAC&R systems. Further exploration of structured theory and alternative applications should be considered.

5.3.1 MCGM Toolbox

In order to expand its usability, improve reliability, and broaden its applicability, consider implementing the following enhancements.

Firstly, integrating additional correlations to calculate heat transfer coefficients in heat exchangers would enhance the system's ability to describe various specific phenomena such as heat exchange during condensation and evaporation. This would lead to more accurate estimations of heat exchanger performance under different operating conditions.

Secondly, the inclusion of additional components and modeling their involved phenomena should be considered. Also, incorporating the capability to model multiple compressors, valves in parallel, and including models for other mass flow devices like pumps and injectors would be advantageous. By doing so, the system would be able to simulate complex systems more comprehensively, thereby enabling a more accurate representation of real-world scenarios.

To improve user interaction and accessibility, exploring the development of a graphical interface would be beneficial. This interface should support users across different stages of modeling, analysis, and optimization phases. A user-friendly graphical interface will streamline the modeling process and enhance user experience, making the system more accessible to a wider audience.

Lastly, implementing functions enabling the toolbox to integrate with other graph-based multi-domain modeling tools, such as the one introduced in [53], would be crucial. This integration would enhance interoperability and allow users to leverage the strengths of different modeling platforms, thereby facilitating collaboration and expanding the system's capabilities.

In conclusion, these proposed improvements aim to make significant strides in enhancing the usability, reliability, and applicability of the system, ultimately contributing to its effectiveness in various engineering applications.

5.3.2 Control Co-Design

One potential advancement of the proposed approach involves extending the application of Global Sensitivity Analysis methods, in tandem with the modeling toolbox, for a more comprehensive analysis of the model. This expansion would facilitate the identification of potential components to con-

sider in the subsequent CCD of the chiller system.

To address one of the limitations of this thesis, a thorough analysis of the couplings occurring within HVAC&R systems would undoubtedly enhance the robustness of the CCD framework. Furthermore, identifying methods for a priori analysis of these couplings remains an open area that could provide a significant contribution.

The co-design methods employed in this dissertation were evaluated considering the steady-state performance of the chiller system. However, potential improvements could arise from using CCD strategies to solve the optimization problem under dynamic operating conditions.

Moreover, leveraging the capability to easily generate models with different components or topologies using the MCGM Toolbox, coupled with its ease of integration with the control system, further advancements could emerge from comparing CCD methods, considering alternative system configurations and/or control architectures.

Bibliography

[1] Mark W Roberts. "Finishing the job: The Montreal Protocol moves to phase down hydrofluorocarbons". In: *Review of European, Comparative & International Environmental Law* 26.3 (2017), pp. 220–230.

[2] Luca Cecchinato, Marco Corradi, Ezio Fornasieri, and Lorenzo Zamboni. "Carbon dioxide as refrigerant for tap water heat pumps: A comparison with the traditional solution". In: *International Journal of Refrigeration* 28.8 (2005), pp. 1250–1258.

[3] A Cavallini. "The state-of-the-art on Refrigerants". In: *Journal of Physics: Conference Series*. Vol. 1599. 1. IOP Publishing. 2020.

[4] Ferdinando Mancini, Silvia Minetto, and Ezio Fornasieri. "Thermodynamic analysis and experimental investigation of a CO2 household heat pump dryer". In: *International Journal of Refrigeration* 34.4 (2011), pp. 851–858.

[5] Vahid Vakiloroaya, Bijan Samali, Ahmad Fakhar, and Kambiz Pishghadam. "A review of different strategies for HVAC energy saving". In: *Energy Conversion and Management* 77 (Jan. 2014), pp. 738–754.

[6] Constanze Fetting. "The European green deal". In: *ESDN report* 53 (2020).

[7] Mohamad Ali Khalil and Mahmudur Rahman Fatmi. "How residential energy consumption has changed due to COVID-19 pandemic? An agent-based model". In: *Sustainable Cities and Society* 81 (June 2022).

[8] Jean Rouleau and Louis Gosselin. “Impacts of the COVID-19 lockdown on energy consumption in a Canadian social housing building”. In: *Applied Energy* 287 (Apr. 2021).

[9] REHVA. *REHVA COVID-19 guidance document. 2020.* 2020.

[10] ASHRAE. *Issues and Statements on Relationship Between COVID-19 and HVAC in Buildings.* 2020.

[11] Alberto Cavallini, Luca Cecchinato, Marco Corradi, Ezio Fornasieri, and Claudio Zilio. “Two-stage transcritical carbon dioxide cycle optimisation: A theoretical and experimental analysis”. In: *International Journal of Refrigeration* 28.8 (2005), pp. 1274–1283.

[12] Luca Cecchinato et al. “Thermodynamic analysis of different two-stage transcritical carbon dioxide cycles”. In: *International Journal of refrigeration* 32.5 (2009), pp. 1058–1067.

[13] Luca Cecchinato, Manuel Chiarello, and Marco Corradi. “Design and experimental analysis of a carbon dioxide transcritical chiller for commercial refrigeration”. In: *Applied Energy* 87 (6 June 2010), pp. 2095–2101.

[14] Luca Cecchinato and Marco Corradi. “Transcritical carbon dioxide small commercial cooling applications analysis”. In: *International Journal of Refrigeration* 34.1 (2011), pp. 50–62.

[15] Yitai Ma, Zhongyan Liu, and Hua Tian. “A review of transcritical carbon dioxide heat pump and refrigeration cycles”. In: *Energy* 55 (2013), pp. 156–172.

[16] Saad Dilshad, Ali Raza Kalair, and Nasrullah Khan. “Review of carbon dioxide (CO2) based heating and cooling technologies: past, present, and future outlook”. In: *International Journal of Energy Research* 44.3 (2020), pp. 1408–1463.

[17] Robert McDowall. *Fundamentals of HVAC systems: SI edition.* Academic Press, 2007.

[18] Herbert W Stanford III. *HVAC water chillers and cooling towers: fundamentals, application, and operation.* CRC press, 2011.

[19] Samuel C Sugarman. *HVAC fundamentals*. Crc Press, 2020.

[20] SA Tassou, John S Lewis, YT Ge, Abas Hadawey, and Issa Chaer. "A review of emerging technologies for food refrigeration applications". In: *Applied Thermal Engineering* 30.4 (2010), pp. 263–276.

[21] Alessandro Beghi and Luca Cecchinato. "Modelling and adaptive control of small capacity chillers for HVAC applications". In: *Applied Thermal Engineering* 31.6-7 (2011), pp. 1125–1134.

[22] Chayan Nadjahi, Hasna Louahlia, and Stéphane Lemasson. "A review of thermal management and innovative cooling strategies for data center". In: *Sustainable Computing: Informatics and Systems* 19 (2018), pp. 14–28.

[23] Mirco Rampazzo, Michele Lionello, Fernando Carpignani Panebianco, and Alessandro Beghi. "Model-free Control of Data Center Compressor-based Cooling Systems". In: *2018 IEEE 4th International Forum on Research and Technology for Society and Industry (RTSI)*. IEEE. 2018, pp. 1–6.

[24] George C Briley. "A history of refrigeration". In: *Ashrae Journal* 46 (2004), S31–S34.

[25] Andy Pearson. "Carbon dioxide—new uses for an old refrigerant". In: *international Journal of Refrigeration* 28.8 (2005), pp. 1140–1148.

[26] Alberto Cavallini and Claudio Zilio. "Carbon dioxide as a natural refrigerant". In: *International Journal of Low-Carbon Technologies* 2.3 (2007), pp. 225–249.

[27] Mirco Rampazzo, Michele Lionello, Alessandro Beghi, Enrico Sisti, and Luca Cecchinato. "A static moving boundary modelling approach for simulation of indirect evaporative free cooling systems". In: *Applied Energy* 250 (2019), pp. 1719–1728.

[28] Mario Garcia-Sanz. "Control Co-Design: An engineering game changer". In: *Advanced Control for Applications: Engineering and Industrial Systems* 1 (1 2019).

[29] Andreas Varga. “Computer-Aided Control Systems Design: Introduction and Historical Overview”. In: *Encyclopedia of Systems and Control* (2020), pp. 1–7.

[30] John E Hesselgreaves, Richard Law, and David Reay. *Compact heat exchangers: selection, design and operation*. Butterworth-Heinemann, 2016.

[31] Y. T. Ge, S. A. Tassou, I. Dewa Santosa, and K. Tsamos. “Design optimisation of CO2 gas cooler/condenser in a refrigeration system”. In: *Applied Energy* 160 (Dec. 2015), pp. 973–981.

[32] Chris P Underwood. *HVAC control systems: Modelling, analysis and design*. Routledge, 2002.

[33] Bryan P Rasmussen. “Dynamic Modeling and Advanced Control of Air Conditioning and Refrigeration Systems”. PhD thesis. 2005.

[34] Alessandro Beghi, Luca Cecchinato, Giovanni Cosi, and Mirco Rampazzo. “A PSO-based algorithm for optimal multiple chiller systems operation”. In: *Applied Thermal Engineering* 32 (2012), pp. 31–40.

[35] Francesco Simmini, Mirco Rampazzo, Fabio Peterle, Gian Antonio Susto, and Alessandro Beghi. “A self-tuning KPCA-based approach to fault detection in chiller systems”. In: *IEEE Transactions on Control Systems Technology* 30.4 (2021), pp. 1359–1374.

[36] James T. Allison and Daniel R. Herber. “Special Section on Multidisciplinary Design Optimization: Multidisciplinary Design Optimization of Dynamic Engineering Systems”. In: 52 (4 Mar. 2014), pp. 691–710.

[37] Daniel R Herber and James T Allison. “Nested and Simultaneous Solution Strategies for General Combined Plant and Control Design Problems”. In: *Journal of Mechanical Design* 141 (1 Oct. 2018).

[38] Diane L. Peters. “Coupling and Controllability in Optimal Design and Control”. PhD thesis. University of Michigan, 2010.

[39] Saeed Azad and Daniel R Herber. “An Overview of Uncertain Control Co-Design Formulations”. In: *Journal of Mechanical Design* 145 (9 July 2023).

[40] Diane L Peters. "A procedure for evaluating the applicability of a control proxy function to optimal co-design". In: *Journal of Engineering Design* 27.8 (2016), pp. 515–543.

[41] Saeid Bayat and James T Allison. "Control Co-Design with varying available information applied to vehicle suspensions". In: *International Design Engineering Technical Conferences and Computers and Information in Engineering Conference*. Vol. 87301. American Society of Mechanical Engineers. 2023.

[42] James T Allison, Daniel S Zalkind, and Daniel R Herber. "Open-Loop Control Co-Design of Semisubmersible Floating Offshore Wind Turbines Using Linear Parameter-Varying Models". In: *Journal of Mechanical Design* 146 (2024).

[43] M Maasoumy, Q Zhu, C Li, F Meggers, and A Sangiovanni-Vincentelli. "Co-design of control algorithm and embedded platform for building HVAC systems". In: 2013, pp. 61–70.

[44] Soumya Vasisht, Arnab Bhattacharya, Sen Huang, Himanshu Sharma, Veronica Adetola, and Draguna Vrabie. "Co-Design of Commercial Building HVAC using Bayesian Optimization". In: *2021 American Control Conference (ACC)*. 2021, pp. 366–372.

[45] Arnab Bhattacharya, Soumya Vasisht, Veronica Adetola, Sen Huang, Himanshu Sharma, and Draguna L Vrabie. "Control co-design of commercial building chiller plant using Bayesian optimization". In: *Energy and Buildings* 246 (2021).

[46] Michael J. Risbeck, Martin Z. Bazant, Zhanhong Jiang, Young M. Lee, Kirk H. Drees, and Jonathan D. Douglas. "Modeling and multiobjective optimization of indoor airborne disease transmission risk and associated energy consumption for building HVAC systems". In: *Energy and Buildings* 253 (Dec. 2021).

[47] Díaz Torres et al. "Energy Performance Comparison of a Chiller Plant Using the Conventional Staging and the Co-Design Approach in the

Early Design Phase of Hotel Buildings". In: *Energies 2023, Vol. 16, Page 3782* 16 (9 Apr. 2023), p. 3782.

[48] Austin L. Nash, Timothy S. Fisher, and Neera Jain. "Combined plant and control design for a flash boiling cooling system". In: *Proceedings of the American Control Conference* 2019-July (July 2019), pp. 4229–4236.

[49] A L Nash and N Jain. "Combined Plant and Control Co-Design for Robust Disturbance Rejection in Thermal-Fluid Systems". In: *IEEE Transactions on Control Systems Technology* 28 (6 2020), pp. 2532–2539.

[50] Austin L. Nash and Neera Jain. "Hierarchical Control Co-Design Using a Model Fidelity-Based Decomposition Framework". In: *Journal of Mechanical Design* 143 (1 Jan. 2021).

[51] Cary Laird, Ziliang Kang, Kai A. James, and Andrew G. Alleyne. "Framework for integrated plant and control optimization of electrothermal systems: An energy storage system case study". In: *Energy* 258 (Nov. 2022).

[52] Christopher Thomas Aksland. "Mission-specific design of aircraft energy systems". In: (Apr. 2023).

[53] Philip M. Renkert and Andrew G. Alleyne. "Component-Based Design Optimization of Multirotor Aircraft". In: *Proceedings of the American Control Conference* 2022-June (2022), pp. 3985–3990.

[54] Bryan P. Rasmussen. "Dynamic modeling for vapor compression systems—Part I: Literature review". In: *HVAC&R Research* 18 (5 Oct. 2012), pp. 934–955.

[55] Andrea Cervato. "Energy analysis of household devices and their modeling software". PhD thesis. 2015.

[56] Enrico Sisti. "Modellizzazione di un sistema di raffreddamento adiabatico indiretto per applicazioni di risparmio energetico nei centri di elaborazione dati". MA thesis. July 2014.

[57] Kayla M. Russell, Christopher T. Aksland, and Andrew G. Alleyne. "Graph-Based Dynamic Modeling of Two-Phase Heat Exchangers in Vapor Compression Systems". In: *International Journal of Refrigeration* 137 (2022), pp. 244–256.

[58] G. L. Wedekind, B. L. Bhatt, and B. T. Beck. "A system mean void fraction model for predicting various transient phenomena associated with two-phase evaporating and condensing flows". In: *International Journal of Multiphase Flow* 4 (1 Mar. 1978), pp. 97–114.

[59] Thomas L. McKinley and Andrew G. Alleyne. "An advanced nonlinear switched heat exchanger model for vapor compression cycles using the moving-boundary method". In: *International Journal of Refrigeration* 31 (7 Nov. 2008), pp. 1253–1264.

[60] Bin Li and Andrew G. Alleyne. "A dynamic model of a vapor compression cycle with shut-down and start-up operations". In: *International Journal of Refrigeration* 33 (3 May 2010), pp. 538–552.

[61] Luca Cecchinato and Ferdinando Mancini. "An intrinsically mass conservative switched evaporator model adopting the moving-boundary method". In: *International Journal of Refrigeration* 35 (2 Mar. 2012), pp. 349–364.

[62] Wolfgang Borutzky. *Bond graph methodology: Development and analysis of multidisciplinary dynamic system models*. Springer London, 2010, pp. 1–662.

[63] Rahmatallah Shoureshi and Kevin McLaughlin. "Modeling and Dynamics of Two-Phase Flow Heat Exchangers using Temperature - Entropy Bond Graphs". In: *Proceedings of the American Control Conference* 1 (1984), pp. 93–98.

[64] F. T. Brown. "Non-iterative evaluation of multiphase thermal compliances in bond graphs". In: 216 (1 Feb. 2002), pp. 13–19.

[65] Jin Long Lin and T. J. Yeh. "Modeling, identification and control of air-conditioning systems". In: *International Journal of Refrigeration* 30 (2 Mar. 2007), pp. 209–220.

[66] Dean Karnopp. "State Variables and Pseudo Bond Graphs for Compressible Thermofluid Systems". In: *Journal of Dynamic Systems, Measurement, and Control* 101 (3 Sept. 1979), pp. 201–204.

[67] M. Kebdani, G. Dauphin-Tanguy, A. Dazin, R. Albach, and P. Dupont. "Two-phase reservoir: development of a transient thermo-hydraulic model based on bond graph approach with experimental validation". In: *Mathematical and Computer Modelling of Dynamical Systems* 23 (5 Sept. 2017), pp. 476–503.

[68] Mohamed Kebdani and Geneviève Dauphin-Tanguy. "Dynamic bond graph modelling of a two-phase cooling system with experimental analysis". In: *International Journal of Simulation and Process Modelling* 16 (2 2021), pp. 79–89.

[69] Simcenter Amesim. 2022. URL: `https://www.plm.automation.siemens.com`.

[70] Paolo Artuso et al. "Dynamic Modelling and Validation of an Air-to-Water Reversible R744 Heat Pump for High Energy Demand Buildings". In: *Energies* 14 (24 2021).

[71] Francesco Fabris, Paolo Artuso, Sergio Marinetti, Silvia Minetto, and Antonio Rossetti. "Dynamic modelling of a CO2 transport refrigeration unit with multiple configurations". In: *Applied Thermal Engineering* 189 (May 2021).

[72] Enrico Sisti et al. "Assessment of basic control strategies through dynamic simulations: A CO2-based chiller under extreme off-design conditions". In: *Energy and Buildings* 289 (June 2023).

[73] Andrew G. Alleyne and Christopher T. Aksland. "Control as an Enabler for Electrified Mobility". In: *Annu. Rev. Control Robot. Auton. Syst.* 5.1 (May 2022), pp. 659–688.

[74] Justin P. Koeln, Matthew A. Williams, Herschel C. Pangborn, and Andrew G. Alleyne. *Experimental Validation of Graph-Based Modeling for Thermal Fluid Power Flow Systems*. Oct. 2016.

[75] Matthew A. Williams. "A framework for the control of electro-thermal aircraft power systems". PhD thesis. University of Illinois at Urbana-Champaign, Sept. 2017.

[76] Herschel C. Pangborn, Matthew A. Williams, Justin P. Koeln, and Andrew G. Alleyne. "Graph-based hierarchical control of thermal-fluid power flow systems". In: *Proceedings of the American Control Conference* (June 2017), pp. 2099–2105.

[77] Christopher T. Aksland and Andrew G. Alleyne. "Hierarchical model-based predictive controller for a hybrid UAV powertrain". In: *Control Engineering Practice* 115 (Oct. 2021).

[78] Christopher T. Aksland, Pamela J. Tannous, Minda J. Wagenmaker, Herschel C. Pangborn, and Andrew G. Alleyne. "Hierarchical Predictive Control of an Unmanned Aerial Vehicle Integrated Power, Propulsion, and Thermal Management System". In: *IEEE Transactions on Control Systems Technology* 31 (3 May 2023), pp. 1280–1295.

[79] Christopher Thomas Aksland. "Modular modeling and control of a hybrid unmanned aerial vehicle's powertrain". MA thesis. Dec. 2019.

[80] Justin P. Koeln, Herschel C. Pangborn, Matthew A. Williams, Malia L. Kawamura, and Andrew G. Alleyne. "Hierarchical Control of Aircraft Electro-Thermal Systems". In: *IEEE Transactions on Control Systems Technology* 28 (4 July 2020), pp. 1218–1232.

[81] C G Khatri and C Radhakrishna Rao. "Solutions to Some Functional Equations and Their Applications to Characterization of Probability Distributions". In: *Sankhyā: The Indian Journal of Statistics, Series A (1961-2002)* 30 (2 1968), pp. 167–180.

[82] Suhas V. Patankar. *Numerical Heat Transfer and Fluid Flow*. CRC Press, Oct. 1980.

[83] The MathWorks Inc. *Graph and Network Algorithms*. Natick, Massachusetts, United States, 2022. URL: `https://www.mathworks.com/help/matlab/graph-and-network-algorithms.html`.

[84] E. W. Lemmon, I. H. Bell, M. L. Huber, and M. O. McLinden. *NIST Standard Reference Database 23: Reference Fluid Thermodynamic and Transport Properties-REFPROP, Version 10.0, National Institute of Standards and Technology*. 2018. URL: https://www.nist.gov/srd/refprop.

[85] Herschel Pangborn, Andrew G. Alleyne, and Ning Wu. "A comparison between finite volume and switched moving boundary approaches for dynamic vapor compression system modeling". In: *International Journal of Refrigeration* 53 (May 2015), pp. 101–114.

[86] T L Bergman, A S Lavine, and F P Incropera. *Fundamentals of Heat and Mass Transfer, 7th Edition*. John Wiley & Sons, Incorporated, 2011.

[87] V. Gnielinski. "New equations for heat and mass transfer in the turbulent flow in pipes and channels". In: *STIA* 41 (1 1975), pp. 8–16.

[88] Zhan Bin Liu, Ya Lings He, Yi Fan Yang, and Ji You Fei. "Experimental study on heat transfer and pressure drop of supercritical CO2 cooled in a large tube". In: *Applied Thermal Engineering* 70 (1 Sept. 2014), pp. 307–315.

[89] Paolo Artuso, Giacomo Tosato, Armin Hafner, Antonio Rossetti, Silvia Minetto, and Sergio Marinetti. *02_ Data_Site−2.txt*. Ed. by Norwegian University of Science and Technology. 2021. URL: https://doi.org/10.18710/UNIYBZ/6DR3LK.

[90] Pedro Albertos and Sala Antonio. *Multivariable control systems: an engineering approach*. Springer London, 2004.

[91] José A. Alfaya, Guillermo Bejarano, Manuel G. Ortega, and Francisco R. Rubio. "Controllability analysis and robust control of a one-stage refrigeration system". In: *European Journal of Control* 26 (Nov. 2015), pp. 53–62.

[92] Guillermo Bejarano, José A. Alfaya, Manuel G. Ortega, and Manuel Vargas. "On the difficulty of globally optimally controlling refrigeration systems". In: *Applied Thermal Engineering* 111 (Jan. 2017), pp. 1143–1157.

[93] Anurag Goyal, Marcel A. Staedter, and Srinivas Garimella. "A review of control methodologies for vapor compression and absorption heat pumps". In: *International Journal of Refrigeration* 97 (Jan. 2019), pp. 1–20.

[94] Neera Jain, Bin Li, Michael Keir, Brandon Hencey, and Andrew Alleyne. "Decentralized feedback structures of a vapor compression cycle system". In: *IEEE Transactions on Control Systems Technology* 18 (1 Jan. 2010), pp. 185–193.

[95] Sigurd Skogestad and Ian Postlethwaite. *Multivariable Feedback Control - Analisys and Design*. Ed. by John Wiley & Sons Inc. Nov. 2005, p. 592.

[96] Joaquim R. R. A. Martins and Andrew Ning. *Engineering design optimization*. Cambridge, UK: Cambridge University Press, Jan. 2022.

[97] Austin L. Nash, Herschel C. Pangborn, and Neera Jain. "Robust Control Co-Design with Receding-Horizon MPC". In: *Proceedings of the American Control Conference* 2021-May (May 2021), pp. 373–379.

[98] Qi Zhang, Yizhong Wu, Li Lu, and Ping Qiao. "A Single-Loop Framework for the Reliability-Based Control Co-Design Problem in the Dynamic System". In: *Machines 2023, Vol. 11, Page 262* 11 (2 Feb. 2023), p. 262.

[99] Rikin Gupta, Wei Zhao, and Rakesh K. Kapania. "Controllability Gramian as Control Design Objective in Aircraft Structural Design Optimization". In: *AIAA Journal* 58.7 (2020), pp. 3199–3220.

[100] Jolan Wauters, Tom Lefebvre, and Guillaume Crevecoeur. "Comparative Study of Co-Design Strategies for Mission-Specific Design of Quadcopters using Differential Flatness and Bayesian Optimization".

In: *IEEE/ASME International Conference on Advanced Intelligent Mechatronics, AIM* 2022-July (2022), pp. 703–709.

[101] Ali Baheri and Chris Vermillion. "Combined Plant and Controller Design Using Batch Bayesian Optimization: A Case Study in Airborne Wind Energy Systems". In: *Journal of Dynamic Systems, Measurement, and Control* 141 (9 May 2019).

[102] Joe Deese, Nihar Deodhar, and Chris Vermillion. "Nested Plant/Controller Co-Design Using G-Optimal Design and Extremum Seeking: Theoretical Framework and Application to an Airborne Wind Energy System". In: *IFAC-PapersOnLine* 50.1 (2017). 20th IFAC World Congress, pp. 11965–11971.

[103] Saeed Azad, Mohammad Behtash, Arian Houshmand, and Michael J. Alexander-Ramos. "PHEV powertrain co-design with vehicle performance considerations using MDSDO". In: *Structural and Multidisciplinary Optimization* 60 (3 Sept. 2019), pp. 1155–1169.

[104] Bart D Frischknecht, Diane L Peters, and Panos Y Papalambros. "Pareto set analysis: local measures of objective coupling in multiobjective design optimization". In: *Structural and Multidisciplinary Optimization* 43 (5 2011), pp. 617–630.

[105] Diane L. Peters, Panos Y. Papalambros, and A. Galip Ulsoy. "Sequential Co-Design of an Artifact and its Controller Via Control Proxy Functions". In: *IFAC Proceedings Volumes* 43 (18 Jan. 2010), pp. 125–130.

[106] Rakesh Patil, Zoran Filipi, and Hosam Fathy. "Computationally Efficient Combined Plant Design and Controller Optimization Using a Coupling Measure". In: *Journal of Mechanical Design* 134 (7 June 2012).

[107] Anand P. Deshmukh, Daniel R. Herber, and James T. Allison. "Bridging the gap between open-loop and closed-loop control in co-design: A framework for complete optimal plant and control architecture de-

sign". In: *2015 American Control Conference (ACC)*. 2015, pp. 4916–4922.

[108] James Allison, David Walsh, Michael Kokkolaras, Panos Y. Papalambros, and Matthew Cartmell. "Analytical target cascading in aircraft design". In: *Collection of Technical Papers - 44th AIAA Aerospace Sciences Meeting* 21 (2006), pp. 16112–16120.

[109] Sulaiman F Alyaqout, Diane L Peters, Panos Y Papalambros, and A Galip Ulsoy. "Generalized Coupling Management in Complex Engineering Systems Optimization". In: *Journal of Mechanical Design* 133 (9 Sept. 2011).

[110] Prasad Vilas Chanekar, Nikhil Chopra, and Shapour Azarm. "Co-design of linear systems using Generalized Benders Decomposition". In: *Automatica* 89 (2018), pp. 180–193.

[111] H K Fathy, J A Reyer, P Y Papalambros, and A G Ulsov. "On the coupling between the plant and controller optimization problems". In: vol. 3. 2001, 1864–1869 vol.3.

[112] Diane L. Peters, Panos Y. Papalambros, and A. Galip Ulsoy. "On Measures of Coupling Between the Artifact and Controller Optimal Design Problems". In: *Proceedings of the ASME Design Engineering Technical Conference* 2 (PARTS A AND B July 2010), pp. 1363–1372.

[113] *Quantification and Use of System Coupling in Decomposed Design Optimization Problems*. Vol. Computers and Information in Engineering. ASME International Mechanical Engineering Congress and Exposition. Nov. 2005, pp. 95–103.

[114] Tulga Ersal et al. "Coupling Between Component Sizing and Regulation Capability in Microgrids". In: *IEEE Transactions on Smart Grid* 4 (Sept. 2013), pp. 1576–1585.

[115] K. M. Tsamos et al. "Performance investigation of the CO2 gas cooler designs and its integration with the refrigeration system". In: *Energy Procedia* 123 (Sept. 2017), pp. 265–272.

[116] Yunting Ge. "CO2 Gas Cooler and Cooling Process". In: *Lecture Notes in Energy* 96 (2023), pp. 91–118.

[117] IDewa M.C. Santosa, Baboo L. Gowreesunker, Savvas A. Tassou, Konstantinos M. Tsamos, and Yunting Ge. "Investigations into air and refrigerant side heat transfer coefficients of finned-tube CO2 gas coolers". In: *International Journal of Heat and Mass Transfer* 107 (Apr. 2017), pp. 168–180.

[118] Diane L. Peters, Panos Y. Papalambros, and A. Galip Ulsoy. "Relationship between coupling and the controllability Grammian in co-design problems". In: *Mechatronics* 29 (2015), pp. 36–45.

[119] Anci Wang, Jianmin Fang, Xiang Yin, Yulong Song, Feng Cao, and Paride Gullo. "Coupling Effect of Air Flow Rate and Operating Conditions on the Performance of Electric Vehicle R744 Air Conditioning System". In: *Applied Sciences 2021, Vol. 11, Page 4855* 11 (11 May 2021), p. 4855.

[120] Andrea Saltelli. "Sensitivity Analysis for Importance Assessment". In: *Risk Analysis* 22 (3 June 2002), pp. 579–590.

[121] Andrea Saltelli et al. *Global sensitivity analysis: The primer*. wiley, Jan. 2008, pp. 1–292.

[122] Bertrand Iooss and Paul Lemaître. "A review on global sensitivity analysis methods". In: *Operations Research/ Computer Science Interfaces Series* 59 (Apr. 2014), pp. 101–122.

[123] Minda Joy Wagenmaker. "Analytical sensitivity analysis methodology for the co-design of thermal management systems". MA thesis. University of Illinois at Urbana-Champaign, July 2021.

[124] Max D. Morris. "Factorial Sampling Plans for Preliminary Computational Experiments". In: *Technometrics* 33 (2 May 1991), p. 161.

[125] Facundo Bre, Arthur Santos Silva, Enedir Ghisi, and Víctor D. Fachinotti. "Residential building design optimisation using sensitivity analysis and genetic algorithm". In: *Energy and Buildings* 133 (Dec. 2016), pp. 853–866.

[126] Francesca Campolongo, Andrea Saltelli, and Jessica Cariboni. "From screening to quantitative sensitivity analysis. A unified approach". In: *Computer Physics Communications* 182 (4 Apr. 2011), pp. 978–988.

[127] Francesca Campolongo, Jessica Cariboni, and Andrea Saltelli. "An effective screening design for sensitivity analysis of large models". In: *Environmental Modelling & Software* 22 (Oct. 2007), pp. 1509–1518.

[128] Francesca Pianosi, Fanny Sarrazin, and Thorsten Wagener. "A Matlab toolbox for Global Sensitivity Analysis". In: *Environmental Modelling & Software* 70 (Aug. 2015), pp. 80–85.

[129] Valentina Noacco, Fanny Sarrazin, Francesca Pianosi, and Thorsten Wagener. "Matlab/R workflows to assess critical choices in Global Sensitivity Analysis using the SAFE toolbox". In: *MethodsX* 6 (Jan. 2019), pp. 2258–2280.

[130] Francesca Pianosi, Fanny Sarrazin, and Thorsten Wagener. "How successfully is open-source research software adopted? Results and implications of surveying the users of a sensitivity analysis toolbox". In: *Environmental Modelling & Software* 124 (Feb. 2020).

[131] Julie A. Reyer, Hosam K. Fathy, Panos Y. Papalambros, and A. Galip Ulsoy. "Comparison of Combined Embodiment Design and Control Optimization Strategies Using Optimality Conditions". In: *Proceedings of the ASME Design Engineering Technical Conference* 2 (Nov. 2020), pp. 1023–1032.

[132] A. Galip Ulsoy. "Design for Ease of Control and Estimation". In: *ASME 2016 Dynamic Systems and Control Conference, DSCC 2016* 1 (Feb. 2017).

[133] Diane Peters, Panos Papalambros, and A. Ulsoy. "Control Proxy Functions for Sequential Design and Control Optimization". In: *Journal of Mechanical Design* 133 (Sept. 2011).

[134] Scott A. Bortoff Yu Jiang Yebin Wang and Zhong-Ping Jiang. "An iterative approach to the optimal co-design of linear control systems". In: *International Journal of Control* 89.4 (2016), pp. 680–690.

[135] M. Moradi, M. Naraghi, and A. Kamali Eigoli. "Optimal codesign of controller and linear plants with input saturation: The sensitivity Lyapunov approach". In: *Optimal Control Applications and Methods* 39 (2 Mar. 2018), pp. 622–637.

[136] Loris Serafino. "Optimizing Without Derivatives: What Does the No Free Lunch Theorem Actually Say?" In: *Notices of the American Mathematical Society* 61 (Aug. 2014), p. 750.

[137] Mohammad Nabi Omidvar, Xiaodong Li, and Xin Yao. "A Review of Population-Based Metaheuristics for Large-Scale Black-Box Global Optimization—Part I". In: *IEEE Transactions on Evolutionary Computation* 26 (5 Nov. 2021), pp. 802–822.

[138] Mohammad Nabi Omidvar, Xiaodong Li, and Xin Yao. "A Review of Population-Based Metaheuristics for Large-Scale Black-Box Global Optimization - Part II". In: *IEEE Transactions on Evolutionary Computation* 26 (5 Oct. 2022), pp. 823–843.

[139] Ramses Sala and Ralf Muller. "Benchmarking for Metaheuristic Black-Box Optimization: Perspectives and Open Challenges". In: *2020 IEEE Congress on Evolutionary Computation, CEC 2020 - Conference Proceedings* (July 2020).

[140] Marcus Gallagher. "Towards improved benchmarking of black-box optimization algorithms using clustering problems". In: *Soft Computing* 20 (10 Oct. 2016), pp. 3835–3849.

[141] David H. Wolpert and William G. Macready. "No free lunch theorems for optimization". In: *IEEE Transactions on Evolutionary Computation* 1 (1 1997), pp. 67–82.

[142] Charlie Vanaret, Francois Gallard, and Joaquim R. R. A. Martins. "On the Consequences of the "No Free Lunch" Theorem for Optimization on the Choice of an Appropriate MDO Architecture". In: *18th AIAA/ISSMO Multidisciplinary Analysis and Optimization Conference* (June 2017).

[143] David Barber. *Bayesian Reasoning and Machine Learning*. Cambridge University Press, 2012.

[144] Christopher M Bishop. *Pattern Recognition and Machine Learning*. Springer New York, Dec. 2006.

[145] J Močkus. "On Bayesian Methods for Seeking the Extremum". In: *Optimization Techniques IFIP Technical Conference: Novosibirsk, July 1–7, 1974*. Ed. by G I Marchuk. Berlin, Heidelberg: Springer Berlin Heidelberg, 1975, pp. 400–404.

[146] J Mockus, Vytautas Tiesis, and Antanas Zilinskas. "The application of Bayesian methods for seeking the extremum". In: vol. 2. Sept. 1978, pp. 117–129.

[147] Tansu Alpcan. "A framework for optimization under limited information". In: *Journal of Global Optimization* 55 (3 Mar. 2013), pp. 681–706.

[148] Bobak Shahriari, Kevin Swersky, Ziyu Wang, Ryan P. Adams, and Nando de Freitas. "Taking the Human Out of the Loop: A Review of Bayesian Optimization". In: *Proceedings of the IEEE* 104.1 (2016), pp. 148–175.

[149] Ankush Chakrabarty, Emilio Maddalena, Hongtao Qiao, and Christopher Laughman. "Scalable Bayesian optimization for model calibration: Case study on coupled building and HVAC dynamics". In: *Energy and Buildings* 253 (Dec. 2021).

[150] Victor Martinez-Viol, Eva M. Urbano, Miguel Delgado-Prieto, and Luis Romeral. "Automatic model calibration for coupled HVAC and building dynamics using Modelica and Bayesian optimization". In: *Building and Environment* 226 (2022).

[151] Qiugang Lu, Leonardo D. González, Ranjeet Kumar, and Victor M. Zavala. "Bayesian optimization with reference models: A case study in MPC for HVAC central plants". In: *Computers & Chemical Engineering* 154 (Nov. 2021).

[152] Xingbin Lin, Qi Guo, Deyu Yuan, and Min Gao. "Bayesian Optimization Framework for HVAC System Control". In: *Buildings 2023, Vol. 13, Page 314* 13 (2 Jan. 2023), p. 314.

[153] Ankush Chakrabarty, Claus Danielson, Scott A. Bortoff, and Christopher R. Laughman. "Accelerating self-optimization control of refrigerant cycles with Bayesian optimization and adaptive moment estimation". In: *Applied Thermal Engineering* 197 (Oct. 2021).

[154] Takuya Takabatake, Makoto Yamamoto, and Hideitsu Hino. "Algorithm for searching optimal set values of absorption chiller system using Bayesian optimization". In: *Science and Technology for the Built Environment* 28 (2 2022), pp. 188–199.

[155] Joe Deese, Peter Tkacik, and Chris Vermillion. "Gaussian process-driven, nested experimental co-design: Theoretical framework and application to an airborne wind energy system". In: *Journal of Dynamic Systems, Measurement and Control, Transactions of the ASME* 143 (5 May 2021).

[156] Soumya Vasisht, Aowabin Rahman, Thiagarajan Ramachandran, Arnab Bhattacharya, and Veronica Adetola. "Multi-fidelity Bayesian Optimization for Co-design of Resilient Cyber-Physical Systems". In: *Proceedings - 13th ACM/IEEE International Conference on Cyber-Physical Systems, ICCPS 2022* (2022), pp. 298–299.

[157] Jasper Snoek, Hugo Larochelle, and Ryan P. Adams. "Practical Bayesian Optimization of Machine Learning Algorithms". In: *Advances in Neural Information Processing Systems* 4 (June 2012), pp. 2951–2959.

[158] The MathWorks Inc. *Statistics and machine learning toolbox*. Natick, Massachusetts, United States, 2022. URL: `https://www.mathworks.com/help/stats/index.html`.

[159] Adam D. Bull. "Convergence rates of efficient global optimization algorithms". In: *Journal of Machine Learning Research* 12 (Jan. 2011), pp. 2879–2904.

[160] Eric Brochu, Vlad M. Cora, and Nando de Freitas. "A Tutorial on Bayesian Optimization of Expensive Cost Functions, with Application to Active User Modeling and Hierarchical Reinforcement Learning". In: (Dec. 2010).

[161] Daniel Packwood. *Bayesian optimization for materials science*. Springer, 2017.

[162] Carl Edward Rasmussen and Christopher K. I. Williams. *Gaussian Processes for Machine Learning*. The MIT Press, Nov. 2005.

[163] Matthew Hoffman, Eric Brochu, and Nando de Freitas. "Portfolio Allocation for Bayesian Optimization". In: AUAI Press, 2011, pp. 327–336.